Early-Type Galaxy Stellar Populations in the Near-Infrared

Author:
Christina Baldwin

Supervisor:
Dr. Richard McDermid

MACQUARIE UNIVERSITY

ASTRONOMY, ASTROPHYSICS AND ASTROPHOTONICS RESEARCH CENTRE

November 25, 2014

A thesis submitted to Macquarie University for the degree of Master of Research

Statement of Originality

The line strengths measured in this thesis are based upon code written by Harald Kuntschner. The spectral fitting was carried out using the pPXF code written by Michele Cappellari. Otherwise, the material presented in this thesis is original (except where cited) and has not been submitted in whole or part for a degree in any university.

Christina Baldwin
October, 2014

Typeset in LaTeX 2_ε.

Acknowledgements

Firstly I would like to express my sincere gratitude to the greatest supervisor on the planet. I would also like to thank my own supervisor, Dr Richard McDermid. Secondly, a big thanks to Lee Spitler and the ExGal group for making this year's Friday lunches so delicious.

Thank you to my fellow MRes sufferers for always understanding my pain. RFL, Tiffany, Brint, Reggie, Reece, Black, Woody, Clen, Guff, Lombardo and that new guy — it's almost over. Thank you Shame, for sharing my love of the Bachelor and The Goodwife, and for finally getting rid of the undercut. Thank you, James for inventing computers. Without these majestic beasts, my thesis would have taken much longer to type. Dean, thank you for thanking me in your thesis. You're very welcome. Baldwin #2, every superhero needs a nemesis. Thank you for being mine. Carlos, you were sometimes around.

To my brothers: Big Balls, Tall Balls and Small Balls. Thanks for being in the family. To my parents, I appreciate you saving all the great genes for me. Thank you to my favourite homemate, And others. Thank you to Vicky for still being my best friend after so many years. Don't be mad that I haven't replied to your text yet, it's because I'm acknowledging you in my thesis.

On a serious note, I'd like to thank Eric Emsellem and Tim de Zeeuw for allowing me to spend four weeks at ESO and for being so helpful and welcoming. A huge thank you to Harald Kuntschner for teaching me more than I ever wanted to know about line strengths and for taking such good care of me in the big, scary city of Garching. Thank you to the AAO for the top-up scholarship. I hope you aren't too disappointed with what your money bought.

And Richard, I seriously couldn't have done it without you.

Abstract

Stellar population synthesis (SPS) models are key to interpreting the spectral energy distributions of galaxies. While different models typically agree at optical wavelengths, these same models give vastly different predictions in the near-infrared, mainly due to different treatments of late-stage stellar evolution, in particular the Thermally Pulsing Asymptotic Giant Branch (TP-AGB) phase. This thesis tests three popular SPS models, with a focus on evaluating the differing treatments of this phase. To this end, we obtain high quality near-infrared spectroscopy of a sample of galaxies with well-known spectral properties. These galaxies were selected from the ATLAS^{3D} sample to span a large range of ages, but other physical properties such as velocity dispersion do not vary significantly within the sample, allowing age-dependent phases such as the TP-AGB to be studied.

We measure the strengths of the CN index at 1.1 μm and the CO index at 2.29 μm and compare these with the predictions of the Bruzual and Charlot (2003), Maraston and Strömbäck (2011), and Conroy et al. (2009); Conroy and Gunn (2010) SPS models. We also perform full spectral fitting of these same models to the data. We find that none of the models can accurately predict the strengths of either the CN or CO indices. Furthermore, we find that the age estimates obtained by fitting single stellar populations (SSPs) to the near-infrared data do not correlate with those obtained from the optical or with those obtained by each other. The inclusion of multiple stellar populations alleviates some issues found with SSP fitting, however all models are found to have certain fundamental inaccuracies in the near-infrared regime.

Contents

Chapter 1

Introduction

1.1 Galaxies

Hierarchical assembly of dark matter is the current cosmological paradigm for how the Universe evolves on the largest of scales (Davis et al. 1985; White and Frenk 1991; Navarro et al. 1995; Baugh 2006). Within this framework, primordial quantum fluctuations grew to macroscopic size during the period of rapid expansion of the Universe known as inflation. These density fluctuations seeded the growth of dark matter haloes (shown in Figure 1.1) within which galaxy formation occurs. Galaxies are the building blocks of the Universe, containing most of the ordinary visible matter which we are able to observe, and hence upon which we base our understanding of the Universe. While numerical simulations are able to reproduce the large scale structure of the Universe, discrepancies arise at the scale of individual galaxies. Thus, in spite of their great importance, the many questions of galaxy formation and evolution are as yet unanswered.

Hierarchical formation of galaxies via merging provides a mechanism to explain the variety of galaxy morphologies seen in the Universe, which can be loosely divided into two main types: late-types (spirals) and early-types (ellipticals and lenticulars) (shown in Figure 1.2). Spiral galaxies are generally blue in colour, with a disk and spiral arms, and are supported by their strong rotation. Ellipticals, on the other hand, are red and spheroidal, with little internal structure or gas and a smoothly decreasing light profile. They are ordered by increasing ellipticity from E0 to E7. This was the basis of Edwin Hubble's classification scheme (Hubble 1926, shown in Figure 1.3), which divided galaxies into groups based solely on their morphology. The spiral and elliptical branches were joined by the Lenticular galaxies (S0), which looked like spirals that had been stripped of their gas (i.e. they were disky but gas free). They were thus considered to be intermediate between the groups.

This simple morphological classification correlates strongly with the stellar populations

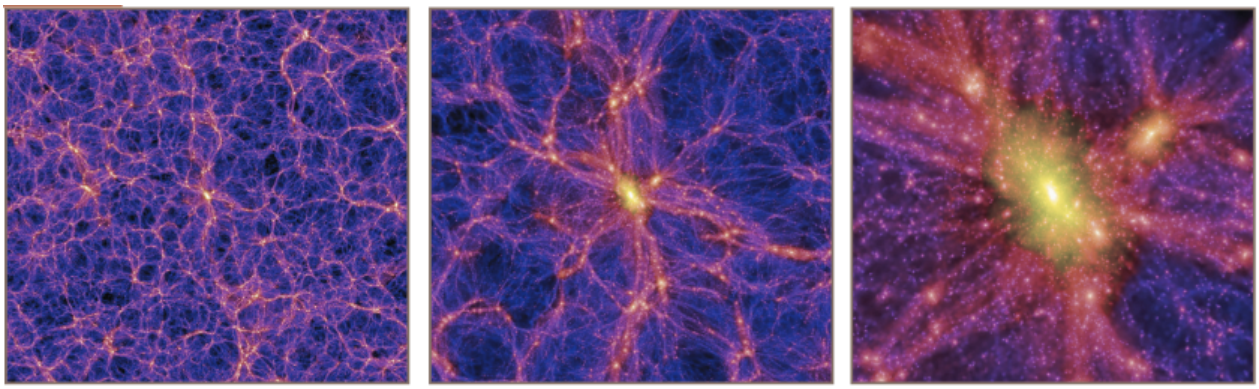

Figure 1.1: The large scale structure of the Universe, as predicted by numerical simulations. The brighter the colour, the higher the density of dark matter. The panels zoom into the structure, with the right-most panel showing an individual dark matter halo (Lemson and Consortium 2006).

present in the galaxies. Spiral galaxies typically have young ages, and are actively star forming. Their blue colour is in fact due to the presence of young stars. Early-type galaxies (ETGs) are generally composed of old stellar populations and were initially thought to be coeval systems which were formed by an initial starburst ∼15 Gyr ago, that have been passively evolving since (Eggen et al. 1962). However this simple picture of ETGs is changing. ETGs have since been found to contain gas (Young et al. 2011), young populations (Kaviraj et al. 2008; Kuntschner et al. 2010) and even ongoing star formation (Wiklind and Rydbeck 1986), indicating that the monolithic collapse scenario put forward by Eggen et al. (1962) is insufficient. A proper understanding of these systems requires an understanding of their star formation histories.

There are two complementary approaches to testing the current ideas of galaxy formation and evolution. One is to directly observe galaxies at high redshift (corresponding to early times) and accurately measure their stellar mass and thus determine how rapidly star formation and assembly occurs (Pérez-González et al. 2008; Marchesini et al. 2009; Ilbert et al. 2013; Tomczak et al. 2014). The second is to understand the 'fossil record' encoded in the stellar populations of today's galaxies, and thus determine how brief or extended their star formation histories were (Thomas et al. 2005). Both of these techniques require a detailed understanding of galaxy stellar populations. ETGs are ideal for these types of studies as their spectra are typically not complicated by dust or strong emission.

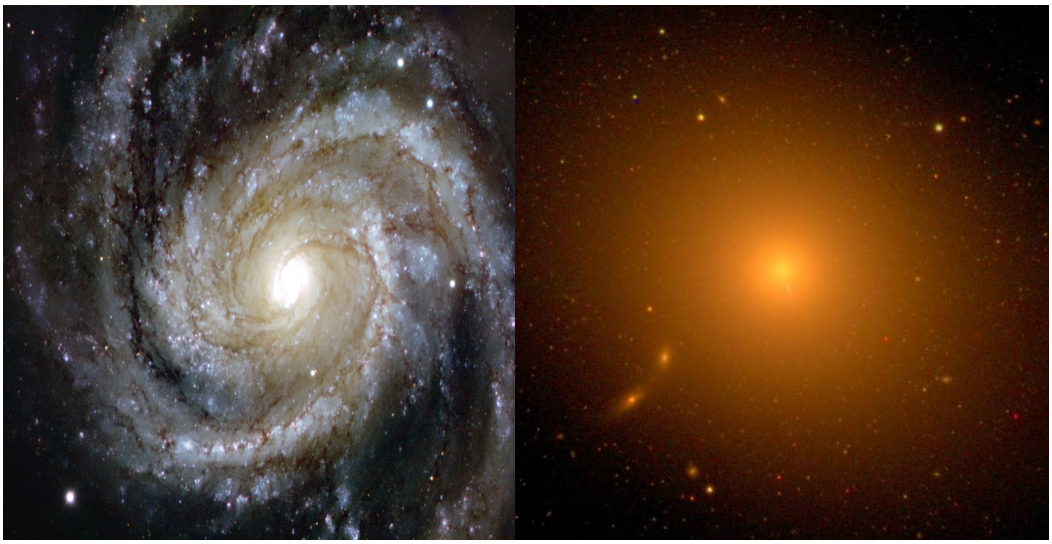

(a) Grand Design Spiral M100 **(b)** Elliptical Galaxy M87

Figure 1.2: The two main galaxy types. (a) Spiral galaxy Messier 100. The dusty blue spiral arms are well-defined and clearly visible. (b) The giant elliptical galaxy Messier 87 is of type E1.

1.2 Stellar Population Synthesis

Within our own galaxy, individual stars can be resolved and studies of stellar populations are carried out using the colour-magnitude diagram. However even with modern telescopes, we are still unable to resolve individual stars in any but the handful of galaxies closest to the Milky Way. Instead we see the integrated light of all stars present in the population. To determine the ages, metallicities and abundances of populations from this integrated starlight requires a stellar population synthesis (SPS) model, which predicts the spectral energy distribution (SED) we would expect to see from a certain population of stars. This technique was pioneered by Tinsley (1968), and has been refined by many authors in the years since (Searle et al. 1973; Larson and Tinsley 1978; Worthey 1994; Vazdekis 1999; Bruzual and Charlot 2003; Schiavon 2007; Conroy et al. 2009; Conroy and Gunn 2010; Maraston and Strömbäck 2011).

The simplest form of SPS modelling uses Single Stellar Populations (SSPs), which are populations formed in a single burst of infinitesimal duration in a uniform chemical environment, with a particular initial mass function (IMF). The spectrum, S, of an SSP of age t, and metallicity Z is given by the sum of the individual stars present:

$$S(t, Z) = \int_{M_{\min}}^{M_{\max}} \phi(M)_{t,Z} S_*(M, t, Z) \tag{1.2.1}$$

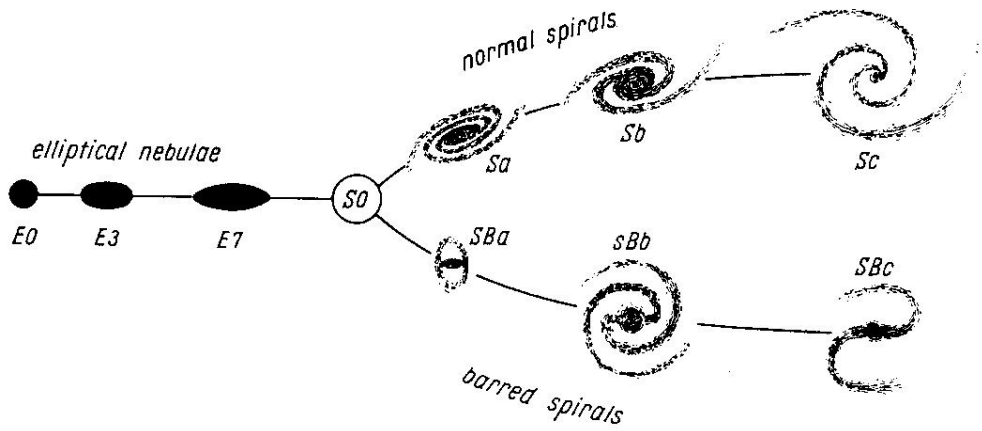

Figure 1.3: Hubble Tuning Fork (Hubble 1926).

where $\phi(M)_{t,Z}$ is the stellar mass function, computed from an initial mass function $\phi_0(M)$. The IMF is an empirical function describing the distribution of stellar masses of a zero-age population. Commonly used IMFs include the Salpeter (1955) IMF: a unimodal power-law; the Kroupa (2001) IMF: a broken power-law; and the Chabrier (2001) IMF: a log-normal form. The IMF is typically valid between a minimum and maximum stellar mass: $M_{\rm min}$ is usually taken to be the hydrogen burning limit of $\sim 0.08 - 0.1$ M$_\odot$, while $M_{\rm max} \sim 100 - 150$ M$_\odot$.

To determine the SED of a star of initial mass, M, age, t, and metallicity, Z, requires two things. Firstly, stellar evolutionary tracks, describing the evolution of a single star with time. These determine where a star with these stellar parameters lies on the Hertzsprung-Russell (H-R) diagram in order to build up the stellar isochrone, which is a curve on the H-R diagram representing a population of stars of the same age. Much work has been done on calculating stellar tracks (e.g. Padova: Marigo and Girardi (2007); Marigo et al. (2008), BaSTI: Pietrinferni et al. (2009), Geneva: Lejeune and Schaerer (2001)), which are now available covering a wide range of initial masses and metallicities.

Secondly, we require a library of stellar spectra for all relevant locations on the H-R diagram. These libraries allow spectra to be selected with the appropriate surface gravity, g, and effective temperature, $T_{\rm eff}$, as predicted by a given isochrone, which are then included in the SSP model spectrum. As with the tracks, much work has been done to build extensive spectral libraries, and there are presently many libraries spanning a wide range of wavelengths and spectral types. Some libraries are empirical (e.g. STELIB (Le Borgne et al. 2003), MILES (Sánchez-Blázquez et al. 2006; Cenarro et al. 2007), ELODIE (Prugniel et al. 2007)), while others are created from theoretical calaculations (e.g., Kurucz 1992; Westera et al. 2002; Lançon et al. 2007). The benefit of empirical libraries is that they are made up of real stars, and thus are complete in their representation of spectral features found in real stars and

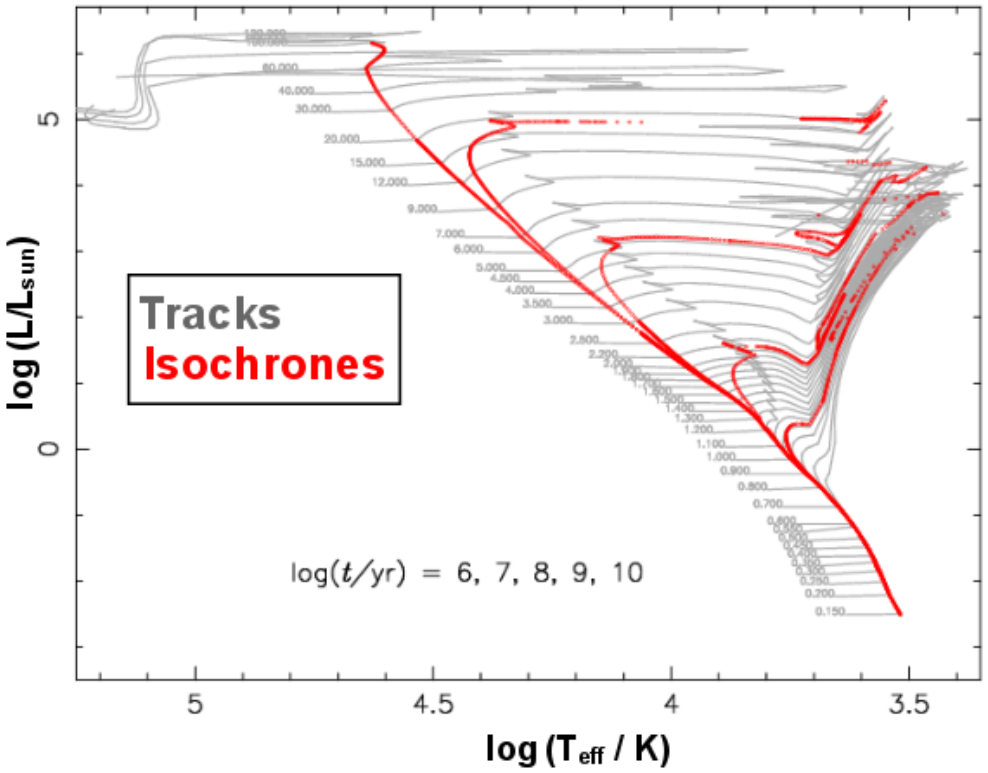

Figure 1.4: Stellar evolutionary tracks (grey lines) and isochrones (red lines), taken from Zhang et al. (2013). The masses of stars range from $0.1 - 100 M_{\odot}$ at logarithmic intervals of 0.05. The ages of isochrones are log(t/yr) = 6, 7, 8, 9 and 10.

galaxies. However, due to observational constraints, they are limited in spectral coverage and resolution, and biased towards the composition of the solar neighbourhood. Theoretical libraries, on the other hand, can cover a wide parameter space at high resolution, however their accuracy is only as good as their input physics and spectral line catalogues, which can be incomplete.

1.2.1 Including the Thermally-Pulsing Asymptotic Giant Branch Phase in SPS Models

One of the limitations of SPS is that all evolutionary phases must be accounted for, some of which are difficult to model. Post-Main Sequence phases are some of the most problematic to account for, as they are typically short lived but also very bright, thus impacting the integrated SEDs quite strongly. As the number of stars in a particular phase depends on the length of the phase in question, stars in short-lived phases are rarely observed. Brief phases such as the thermally-pulsing asymptotic giant branch (TP-AGB) are thus difficult to account for empirically. The TP-AGB phase is also difficult to model theoretically, due to

the variable pulses and strong mass loss taking place. This mass loss causes changes in the star's structure which are very difficult to accurately incorporate into models.

The AGB phase occurs when low- and intermediate-mass stars ($M < 8\ M_{\odot}$) exhaust the helium in their cores. This phase is characterised by nuclear burning of hydrogen (H) and helium (He) in thin shells above a degenerate core composed of carbon and oxygen. In the early stages of the AGB phase (the E-AGB), the energy output of the star is dominated by burning in the He-shell. As the star evolves through the E-AGB phase, it cools and the convective envelope of the star deepens. At some point the convective envelope extends deep enough to transport the products of hydrogen-burning (He, neon) to the star's surface in what is known as the "second dredge-up". The E-AGB is followed by the thermally pulsing-AGB or TP-AGB phase. During this phase the dominant energy output alternates between He-burning and H-burning. The thermal pulses that occur are due to the unstable burning of the He-shell. They happen as the H-burning shell periodically dumps helium ash onto the helium layer below. This produces a brief, high energy pulse on a time-scale of several tens of years (Herwig et al. 2000). These pulses drive convection such that the material produced in the He-burning shell (mostly carbon products) is mixed and transported to the base of the H-burning shell. Furthermore, the outer convective zone increases with the pulse strength of the helium flashes, eventually reaching this region and transporting the carbon to the surface. This is called the "third dredge-up" (Herwig et al. 2000).

As carbon is transported to the surface with every thermal pulse, a star that started the AGB with a C/O ratio less than unity can at some point become a carbon star (C star), in which the C/O ratio exceeds 1. In a C star, all of the oxygen is tied up in CO molecules, with leftover carbon atoms forming molecules such as CN, CH and C_2. Prior to this point, the envelope was oxygen-rich, with all the carbon bound in CO, and the remaining oxygen free to form molecules such as TiO and SiO. Intermediate between these oxygen-rich stars (M stars) and C stars are what are known as S stars, which have a C/O ratio of approximately unity.

After a burst of star formation, the contribution to the integrated light of a single stellar population due only to TP-AGB stars peaks between 0.3 and ~ 1.5 Gyr (Lançon 1998).This contribution can be up to 40% of the bolometric luminosity of a population, and up to 80% of the K band light (Maraston 2006). Strong carbon and oxygen features (and associated molecular tracers) visible in the integrated light of a stellar population are a signature of TP-AGB stars, and thus may indicate the presence of an intermediate age population. Typical spectra of C and M stars are shown in Figure 1.5, along with integrated spectra of stellar populations containing these kinds of stars.

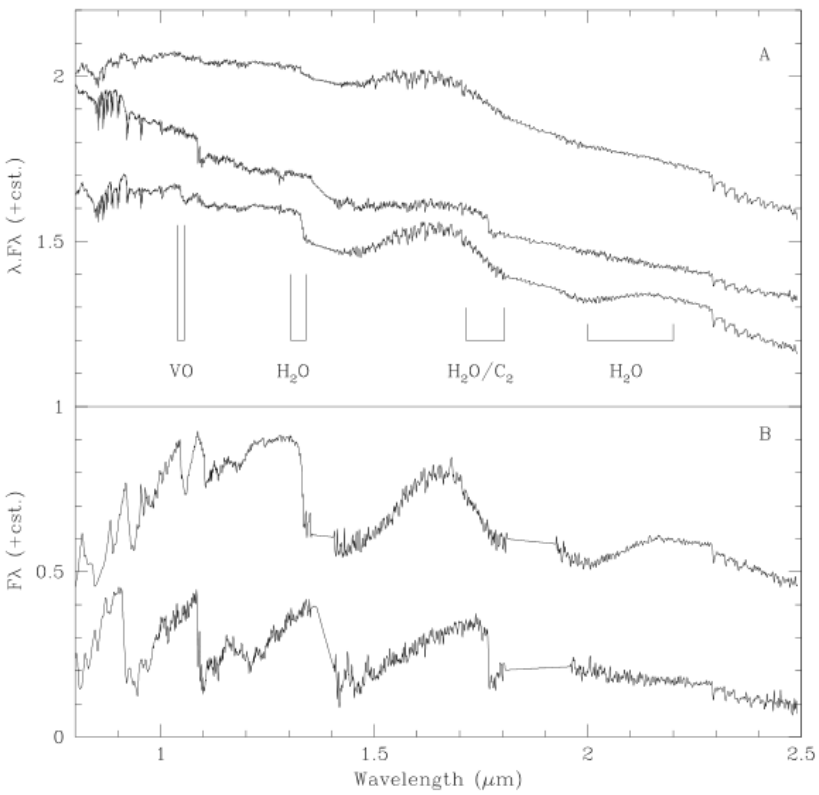

Figure 1.5: Synthetic integrated spectra, taken from Lançon (1998). A: Integrated population spectra. From top to bottom: a giant dominated 4 Gyr old population, and two populations $\sim$ 200 Myr after a starburst, when most TP-AGB stars are respectively C-rich and O-rich. B: Typical cool M star (top) and C star (bottom) spectra.

1.3 Previous Work

The treatment of the TP-AGB phase in SPS models has been somewhat controversial since Maraston (2005) (hereafter referred to as M05) revealed its potentially large impact on the near-infrared luminosity of intermediate age (0.2–2 Gyr) populations. The M05 models made two testable predictions for intermediate age populations: firstly, boosted near-infrared flux, and secondly, strong absorption features due to the carbon and oxygen in the atmospheres of TP-AGB stars. These predictions are in contrast to the predictions of other popular SPS models such as Bruzual and Charlot (2003) (hereafter referred to as BC03), which give much less weight to the TP-AGB phase. The predictions of these models are discussed in more detail in Chapter 4. Many studies have been carried out with the aim of proving (or disproving) these predictions, however the results so far have been contradictory.

Maraston et al. (2006) fit M05 and BC03 models to the near-infrared photometry of seven high redshift early-type galaxies. UV/optical spectra of these galaxies exhibit features

indicative of A- and F-stars, implying that these galaxies are in the critical age range $0.2 - 2$ Gyr, which is the age at which the contribution of the TP-AGB phase is thought to be at a maximum. They found that the M05 models give better fits to the data, as well as obtaining photometric redshifts which are in better agreement with spectroscopic redshifts for these galaxies. They also found that use of the M05 models led to estimates of age and mass that are systematically lower than those derived using the BC03 models (by $\sim 60\%$ on average), highlighting the importance of a correct treatment of this phase. Figure 1.6 shows the impact of different approaches on the stellar masses derived using SPS modelling. The top panels show the effects of different SPS models: the left panel shows the masses obtained by BC03 and M05 when using only the optical and near-infrared bands, while the right hand panel shows the masses obtained with the inclusion of the IRAC $3.5 - 8$ μm data. The M05 models are able to reproduce the galaxy SEDs with lower ages, therefore leading to a lower derived mass. This effect is strengthened with the inclusion of the IRAC bands, as the TP-AGB phase contributes most strongly in the rest-frame near-infrared. The bottom panels show the effects of the wavelength range included in the fit for given SPS models. The BC03 models are not noticeably affected by the inclusion of the IRAC bands, however use of the M05 models leads to three galaxies showing markedly lower masses when the IRAC fluxes are included.

Tonini et al. (2009, 2010) investigated the impact of the TP-AGB phase on galaxy evolution models by comparing the PEGASE models (which do not include the TP-AGB phase) with the M05 models. They found that the near-infrared colors of model galaxies can differ by up to 2 magnitudes between the models, with the difference being greater at high redshift. The inclusion of the TP-AGB phase in the Maraston models solves the problem of the abundance of luminous red galaxies at high-redshift (Yan et al. 2004; Cirasuolo et al. 2008), which when interpreted with traditional SPS models, are too old and massive to exist this early.

MacArthur et al. (2010) used optical spectral fitting techniques to obtain star formation histories of two spiral galaxies which had recently undergone star formation (within ~ 1 Gyr) using BC03 models. They then compared the optical-NIR colours predicted by BC03 based on that star formation history to the observed galaxy colours. They found that the observed colours were too red compared to the model predictions. However, the inclusion of a 1 Gyr population from a model incorporating a strong contribution from the TP-AGB phase was found to bring observed and predicted colors into agreement.

Melbourne et al. (2012) used high resolution HST images of 23 nearby galaxies to constrain the contribution of TP-AGB stars and red helium burning stars to their 1.6 μm luminosities. They found that the TP-AGB phase, while contributing negligible stellar mass, can contribute

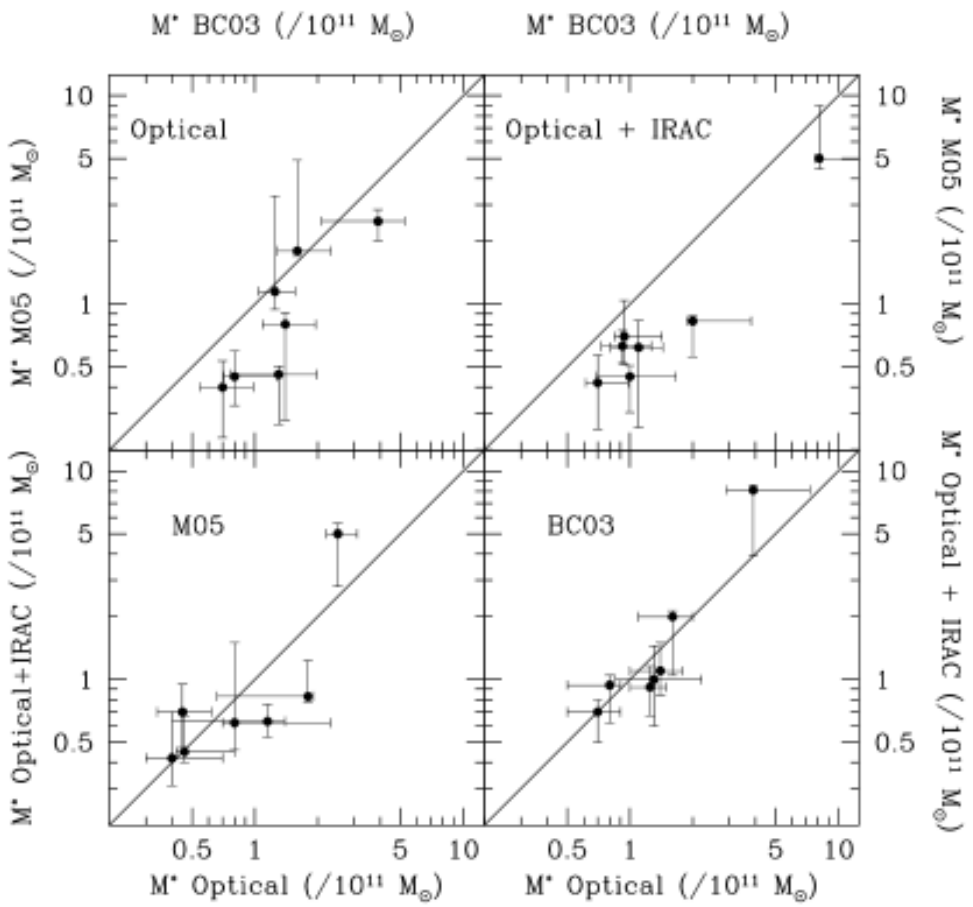

Figure 1.6: Fig 9 of Maraston et al. (2006), showing the effect of different approaches on the stellar masses derived by SED fitting. The top panels show the effect of the SPS models used on the stellar masses, using only optical bands (left panel) and optical plus IRAC bands (right panel). The bottom panels show the effect of the wavelength range for given set of templates: M05 (left panel) and BC03 (right panel).

as much as 17% of the 1.6 μm flux, and more at higher redshift.

Observationally, the CN bands predicted by the M05 models have been detected in the nuclear spectra of AGN by Riffel et al. (2007) and in the nuclear spectra of nearby active galaxies by Mason et al. (2014, submitted). Lyubenova et al. (2012) also detected the C_2 feature at 1.77 μm in accordance with M05 predictions.

Conroy and Gunn (2010) compared the SPS models of BC03 and M05 with their own, newly made Flexible Population Synthesis model (Conroy et al. 2009; Conroy and Gunn 2010). They compared the three models using ultraviolet, optical, and near-infrared photometry, plus spectroscopy of star clusters in the Magellanic Clouds and the Milky Way, as well as photometry and spectral indices of nearby quiescent and post-starburst galaxies. They found that all models fall short in some areas, particularly in reproducing the J-K and

V-K colors of the star clusters. However, overall, they found the Maraston models to perform most poorly of the three, being unable to reproduce the colours of post-starburst galaxies and star clusters in the Magellanic Clouds.

Kriek et al. (2010) constructed a composite SED from the photometry of 62 post-starburst galaxies, spanning the wavelength range $1200 - 40000$ Å. They found that this SED could be well fit by the BC03 models, but that the M05 models could not simultaneously reproduce the rest-frame optical and near-infrared portions of the SED. Restricting the fit to only the optical regime, the Maraston models overpredicted the rest-frame near-infrared flux whereas the BC03 models fit well.

Zibetti et al. (2013) analysed the optical colours and near-infrared spectra of a sample of 16 post-starburst galaxies. They aimed specifically to observe two features predicted by the Maraston models, namely the strong carbon bandhead drops at 1.41 μm and 1.77 μm. These features are typically difficult to observe, as they lie inside regions of poor atmospheric transmission between the near-infrared bands. The authors thus selected galaxies at $z \approx 0.2$ so as to shift these two features inside the atmospheric windows where they can be seen. They did not detect these features in their spectra, and they found that the Maraston models were unable to reproduce the optical colours and near-infrared spectra simultaneously, while the BC03 models do well.

1.4 Outline and aims of thesis

The aim of this thesis is to put new, robust constraints on the hotly debated contribution of the TP-AGB phase to the integrated near-infrared light of intermediate age galaxies. The recent availability of infrared array detectors, as well as a new generation of advanced infrared spectrographs (e.g. GNIRS, NIFS, NIRSpec etc.) have opened up the near-infrared regime for routine analysis. The near-infrared wavelength range contains signatures of AGN (Lacy et al. 2013), intermediate age stellar populations, (e.g., McLean et al. 2000) and is less affected by dust obscuration than the optical regime. The growing importance of the near-infrared spectral range leads to a growing need for accurate near-infrared modelling, which is currently not well understood. Correct treatment of the TP-AGB phase, which impacts intermediate age populations, is especially important at high-redshift, when the Universe itself is only a few Gyrs old. To this end, we test the predictions of three popular SPS models. We use for this study high signal-to-noise near-infrared spectroscopy of a sample of nearby ETGs with a range of ages, selected from the ATLAS^{3D} Survey (Cappellari et al. 2011). By comparing different model predictions to high-quality infrared spectroscopy with well-characterized properties from ATLAS^{3D} optical spectroscopy, this thesis aims to evaluate

the successes and failures of the stellar population models, and thus inform the construction of future population models and their applications.

This thesis is organised as follows. In Chapter 2 we describe the sample, along with relevant information about the ages, metallicity and gas content previously reported by the ATLAS^{3D} Team. We then outline the steps taken in the reduction of the data. Chapter 3 undertakes a visual analysis of the spectra. The three SPS models we compare are those of Maraston and Strömbäck (2011), Bruzual and Charlot (2003) and Conroy et al. (2009); Conroy and Gunn (2010). These models are described in Chapter 4, and the different model predictions laid out. Chapter 5 gives the results of our line strength analysis, and a comparison of measured line strengths with the various model predictions with the aim of obtaining ages and metallicities for each galaxy. Chapter 6 describes our spectral fitting analysis and comparison of the spectral fits with model predictions and with ATLAS^{3D} values. Chapter 7 summarises our main conclusions.

Chapter 2

Observations and Data Reduction

This thesis concerns the analysis of near-infrared data of twelve galaxies taken with the Gemini Near-Infrared Spectrograph (GNIRS) on the Gemini North 8 m telescope. In this chapter the sample, observations, and the steps taken in the reduction of the data are described.

2.1 The Sample

The sample consists of twelve ETGs selected from the ATLAS^{3D} survey (Cappellari et al. 2011). The ATLAS^{3D} survey observed a complete, volume-limited sample of 260 ETGs within 40 Mpc, with absolute K_s magnitude brighter than -21.5, spanning a range of masses from $10^{10} - 10^{12}$ $M_\odot$. The galaxies for this study were selected from the parent sample so as to span a wide range of ages, but a narrow range of velocity dispersion ($\sigma = 80 - 120$ kms^{-1}), metallicity ([Z/H] = -0.2 to 0.2) and abundance ratio ([α/Fe]= $0.1 - 0.3$). This careful selection was required to isolate age as the main parameter varying across the sample of objects, and thus study the age dependence of the galaxies' infrared spectra. The selection criteria are displayed in Figure 2.1.

The ATLAS^{3D} survey obtained optical integral-field spectroscopy, interferometric CO maps, UV imaging and Spitzer imaging for all galaxies in the sample, making this one of the best-studied samples of ETGs available, with mean ages and metallicities as well as complete star formation histories calculated from stellar population fitting of their optical spectra. IC 0719, NGC 3032, NGC 3156, NGC 3182, NGC 3489 and NGC 4710 were detected in CO molecular gas by Young et al. (2013); Combes et al. (2007), who showed that there is a correlation between molecular gas detection and young stellar populations as traced by the Hβ line. This gas detection is indicative of ongoing star formation, as measured by Davis et al. (2014). We can therefore be confident that the relevant ages for detecting TP-AGB signatures will be included within this sample. Unlike previous works on this subject whose

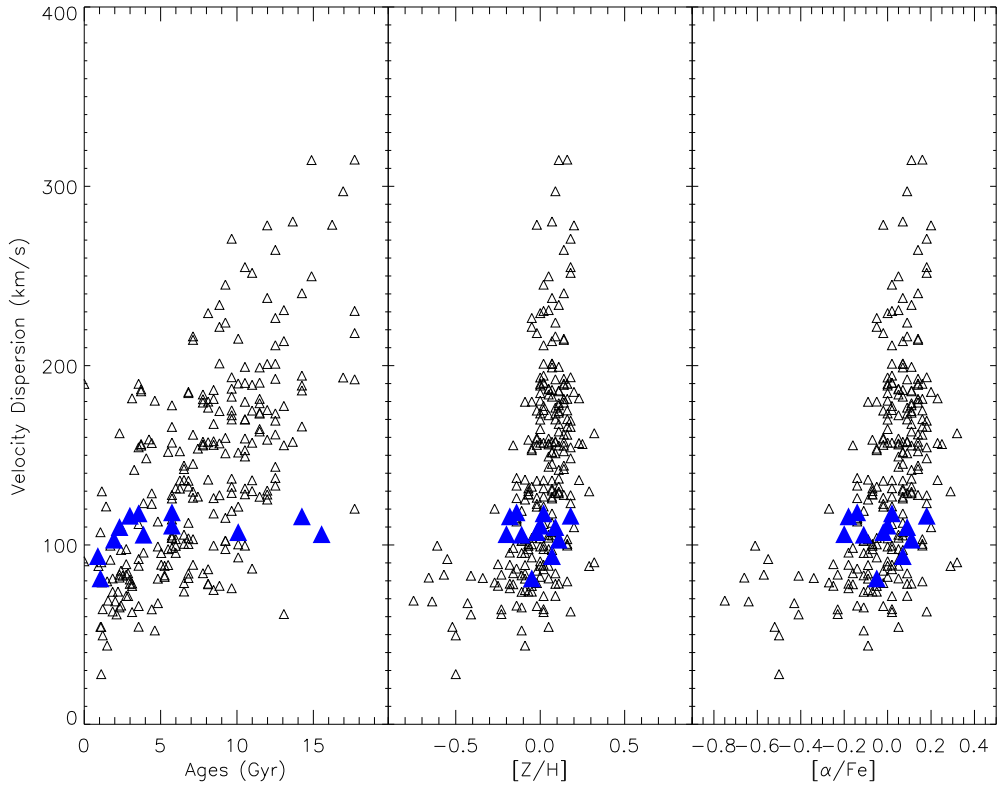

Figure 2.1: Sample selection. Panels show (from left to right) mean central stellar age, metallicity and abundance ratio varying against stellar velocity dispersion, all derived from ATLAS^{3D} optical spectroscopy. Blue triangles show our sample selection, taking a narrow range in velocity dispersion ($100 - 120$ km s^{-1}). This gives a small range of metallicity and abundance ratio, but a broad range in age.

samples spanned only the age range at which the TP-AGB phase is expected to dominate the integrated light output, this sample also includes galaxies where the contribution from the TP-AGB phase should be negligible (i.e. old stellar populations, with no gas detected), giving us a "control" sample with which to compare. The basic galaxy parameters are summarised in Table 2.1. SDSS images are available for all the galaxies in our sample, and are displayed in Figure 2.2.

2.2 The Observations

The spectra were obtained over six nights between 1 February, 2012 and 1 May, 2012, using the Gemini Near-Infrared Spectrograph (GNIRS) on the Gemini North 8 m telescope in Hawaii. They were taken in queue mode through observing program GN-2012A-Q-22, with observing conditions constraints of 85th percentile for seeing (1.1" or better in V-band), 50th percentile for cloud cover (photometric), and any water vapour or sky background.

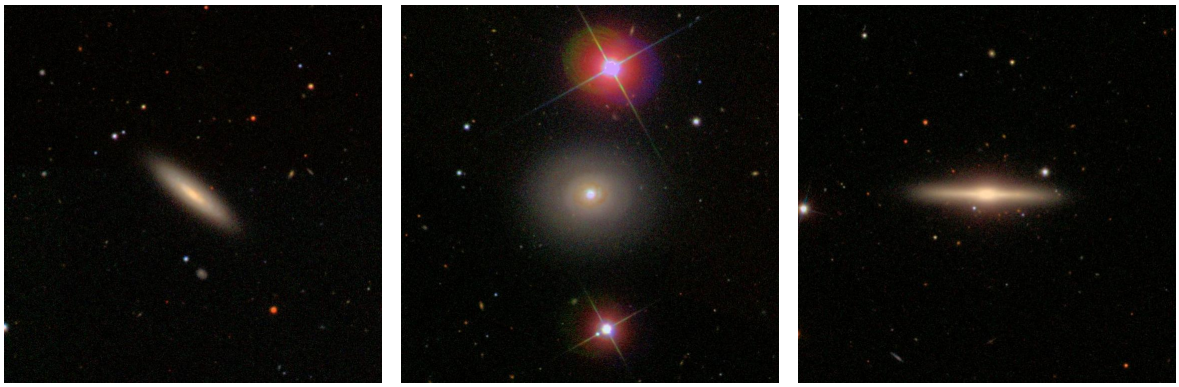

(a) IC 0719 **(b)** NGC 3032 **(c)** NGC 3098

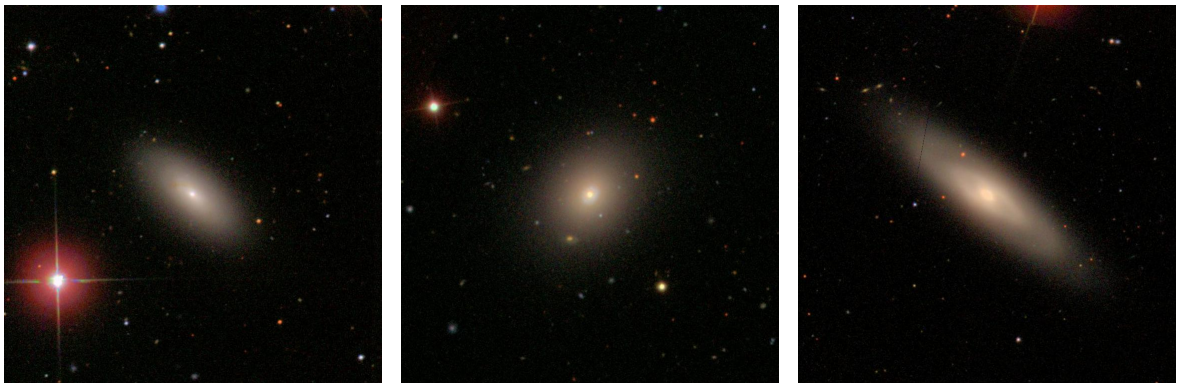

(d) NGC 3156 **(e)** NGC 3182 **(f)** NGC 3301

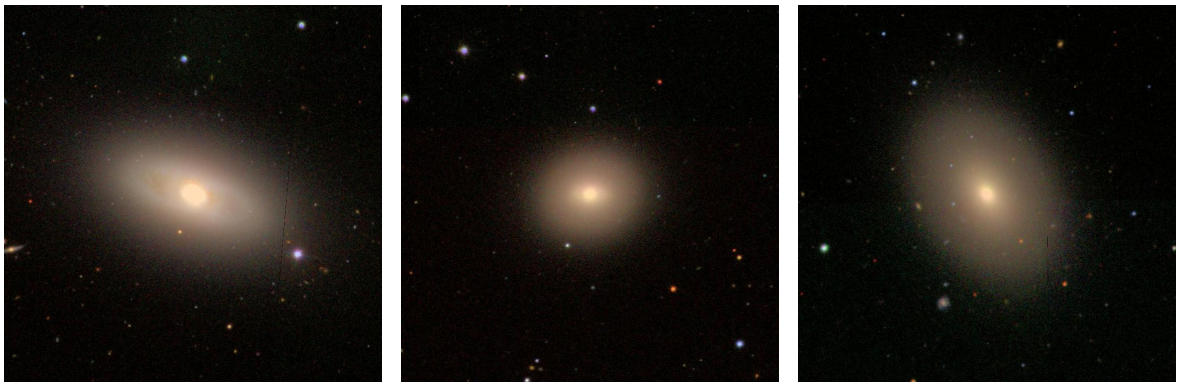

(g) NGC 3489 **(h)** NGC 4379 **(i)** NGC 4578

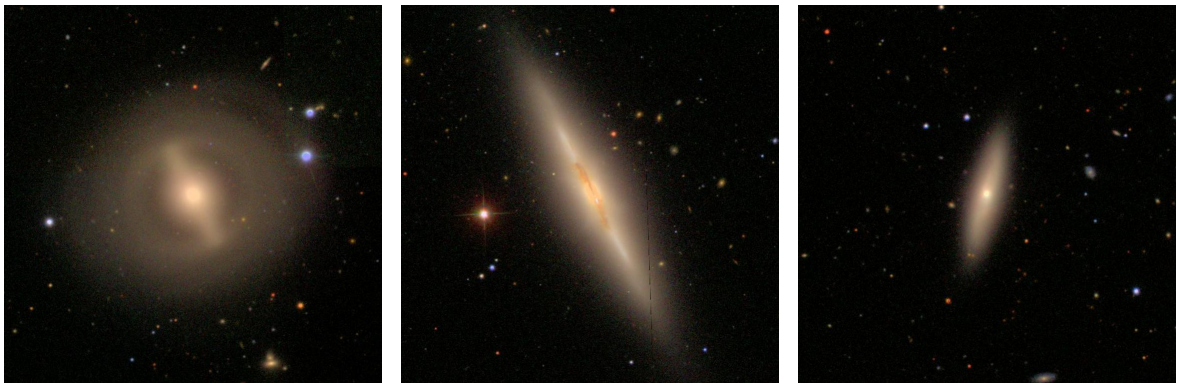

(j) NGC 4608 **(k)** NGC 4710 **(l)** NGC 5475

Figure 2.2: SDSS images of sample galaxies.

Table 2.1: Sample Properties.

Galaxy	Right Ascension	Declination	Velocity	σ	M_K	Age	[Z/H]	[α/Fe]
(1)	(2)	(3)	(4)	(5)	(6)	(7)	(8)	(9)
IC 0719	175.077042	9.009861	1833	117.64	-22.70	3.56	0.02	0.10
NGC 3032	148.034119	29.236279	1562	93.78	-22.01	0.89	0.07	0.04
NGC 3098	150.569458	24.711092	1397	118.22	-22.72	5.74	-0.14	0.17
NGC 3156	153.171692	3.129320	1338	81.39	-22.15	1.06	-0.05	-0.01
NGC 3182	154.887558	58.205818	2118	110.78	-23.19	5.74	-0.00	0.25
NGC 3301	159.233459	21.882166	1339	109.97	-23.28	2.31	0.09	0.09
NGC 3489	165.077454	13.901258	695	102.94	-22.99	1.94	0.11	0.09
NGC 4379	186.311386	15.607498	1074	106.03	-22.24	15.54	-0.20	0.24
NGC 4578	189.377274	9.555121	2292	107.15	-22.66	10.08	-0.02	0.14
NGC 4608	190.305374	10.155793	1850	115.97	-22.94	14.25	-0.18	0.25
NGC 4710	192.412323	15.165490	1102	105.75	-23.53	3.88	-0.11	0.21
NGC 5475	211.301437	55.741802	1671	116.30	-22.88	2.99	0.18	0.14

Notes: (1) Galaxy name. (2) Right Ascension in decimal degrees (J2000.0). (3) Declination in decimal degrees (J2000.0). (4) Recession velocity in km s^{-1}. (5) Velocity dispersion σ in km s^{-1}. (6) Absolute K-band magnitude. (7) SSP-equivalent age in Gyr. (8) SSP-equivalent total metallicity. (9) SSP-equivalent α-abundance. Columns (2)-(5) were taken from Cappellari et al. (2011). (6)-(9) were taken from McDermid et al. (submitted), and are SSP-equivalent mean values calculated by fitting SPS models to the galaxies' optical spectra. They were measured using an $R_e/8$ aperture, which is similar to the scales probed by GNIRS.

GNIRS is a specialised near-infrared spectrograph offering a variety of spectroscopic capabilities (Elias et al. 2006a,b). For this study, GNIRS cross-dispersed (XD) spectroscopy mode was utilised, providing simultaneous coverage across five orders without inter-order contamination. Using the short (0.15"/pixel) blue camera, a 32 l/mm grating, and a slit of width 0.3" and length 7" gives complete coverage from $0.85 - 2.5$ μm at an instrumental resolution of $R \sim 1700$ ($R \sim 9$ Å (FWHM)). This spectral range contains a number of features predicted to be prominent in TP-AGB stars, including the CN breaks at 1.1 μm and 1.4 μm, the C_2 feature at 1.8 μm and the CO bandhead at 2.29 μm (Maraston 2005; Maraston and Strömbäck 2011; Origlia and Oliva 2000). It also includes a number of other features, most of which have not been well studied. These are described in more detail in Chapter 3. An observation log is given in Table 2.2.

For each observation, the object was centred 1" from the slit centre.The telescope was then offset 50" from the object to observe a blank region of sky in order to facilitate the removal of night sky emission lines and dark current. The standard star and object were observed at different locations along the slit to avoid persistence from the standard stars impacting

Table 2.2: Observation Log.

Galaxy (1)	Date (2)	Integration Time (s) (3)	S/N_J (4)	S/N_H (5)	S/N_K (6)
IC 0719	04-02-2012	8x120	74	177	208
NGC 3032	10-02-2012	6x120	124	195	252
NGC 3098	05-02-2012	6x120	117	208	299
NGC 3156	04-02-2012	10x120	99	169	203
NGC 3182	04-02-2012	8x120	109	174	217
NGC 3301	04-02-2012	4x120	160	281	410
NGC 3489	01-02-2012	4x120	224	313	455
NGC 4379	03-02-2012	6x120	108	154	161
NGC 4578	04-02-2012	6x120	136	229	281
NGC 4608	01-05-2012	8x120	78	129	217
NGC 4710	10-02-2012	6x120	51	161	258
NGC 5475	10-02-2012	7x120	105	241	285

Notes.(1) Galaxy name. (2) Date: day, month, year. (3) On-source exposure time. (4)-(6) Average signal-to-noise calculated in the JHK bands, where the noise spectrum was estimated as the difference between the observed spectrum and smoothed version of itself.

the object. The pattern used was ABAABA, which gives a neighbouring sky frame to every galaxy exposure while keeping an on-source efficiency of 66%.

Immediately after each observation, a set of calibration images were taken with the telescope at the position of the galaxy, consisting of flat-field and emission-line calibration lamps. This ensures that there is minimal instrument flexure between the science and calibration exposures. Observations of a bright A-star were also taken before and/or after each galaxy sequence, in order to enable the removal of atmospheric absorption features (or 'telluric' absorption) from the galaxy spectra. The telluric stars used are listed in Table 2.3.

2.3 Data Reduction

The aim of data reduction is to remove instrumental signatures, mask unwanted signals, and perform any necessary calibrations. The data were reduced using version 2.0 of the XDGNIRS pipeline made public by Rachel Mason via the Gemini DRForum[1]. The pipeline uses a wrapper, XDpiped, to call a variety of tasks, mostly from the Gemini IRAF package (Cooke and Rodgers 2005). These tasks convert the original two-dimensional (2D) data into a flux-calibrated one-dimensional (1D) spectrum. Examples of the raw 2D data are shown

[1]http://drforum.gemini.edu/topic/gnirs-xd-reduction-script/

Table 2.3: Telluric Parameters.

Name	RA	DEC	M_K	Type	Integration Time (s)	Associated Galaxy
HIP58616	261.9051	+71.1321	12.496	A1V	12x2	IC 0719
HIP44512	198.0997	+40.0782	9.193	A1V	8x1	NGC 3032
HIP45272	207.2047	+40.3625	13.392	A2V	8x1	NGC 3098
HIP45167	226.8590	+32.8559	14.913	A0V	8x1	NGC 3156
HIP44717	156.5883	+40.1529	12.338	A2V	8x1	NGC 3182
HIP55166	212.1556	+68.9505	15.363	A3V	8x2	NGC 3301
HIP56736	242.8442	+69.5211	15.170	A0V	8x20	NGC 3489
HIP62478	299.6228	+76.4042	11.147	A1V	8x1	NGC 4379
HIP62478	299.6228	+76.4042	16.069	A1V	7x1	NGC 4578
HIP62478	299.6228	+76.4042	15.214	A1V	8x1	NGC 4608
HIP65599	333.3763	+72.6448	12.523	A0V	8x5	NGC 4710
HIP67548	108.8267	+56.9431	11.167	A3V	8x1	NGC 5475

Notes. (1) Name of telluric star. (2) Right Ascension in decimal degrees (J2000). (3) Declination in in decimal degrees (J2000). (4) K-band magnitude from Skrutskie et al. (2006). (5) Spectral type. (6) Integration time in seconds. (7) Galaxy for which star was used.

in Figure 2.3. Here the various steps involved are summarised.

Cosmic Ray and Radiation Event Removal

The GNIRS short camera has radioactive lens coatings, which cause radiation events on the output spectra, similar in appearance to cosmic rays. These are removed by creating a minimum frame at each nod position and flagging any pixels which deviate from this clean image by some multiple of the noise. This threshold is chosen individually for each galaxy so as to remove as many radiation events as possible without erroneously flagging any real signal. Deviant pixels are then interpolated over using IRAF's *fixpix* task.

Flat Fielding

Flat fielding accounts for the differential sensitivity of individual pixels on the detector. A flat frame is taken by illuminating the detector with a uniform light source, which should be smooth in the spectral direction. In this case, multiple flats were taken using a Quartz-Halogen (QH) lamp, and an infrared (IR) lamp. The QH flats have a strong spectral feature in order 3, so for that order the IR lamp was used and then combined with the QH flats into a single master flat frame. This frame was then collapsed along the spatial direction and fitted with a polynomial. The 2D flat frame was divided by the polynomial and the science

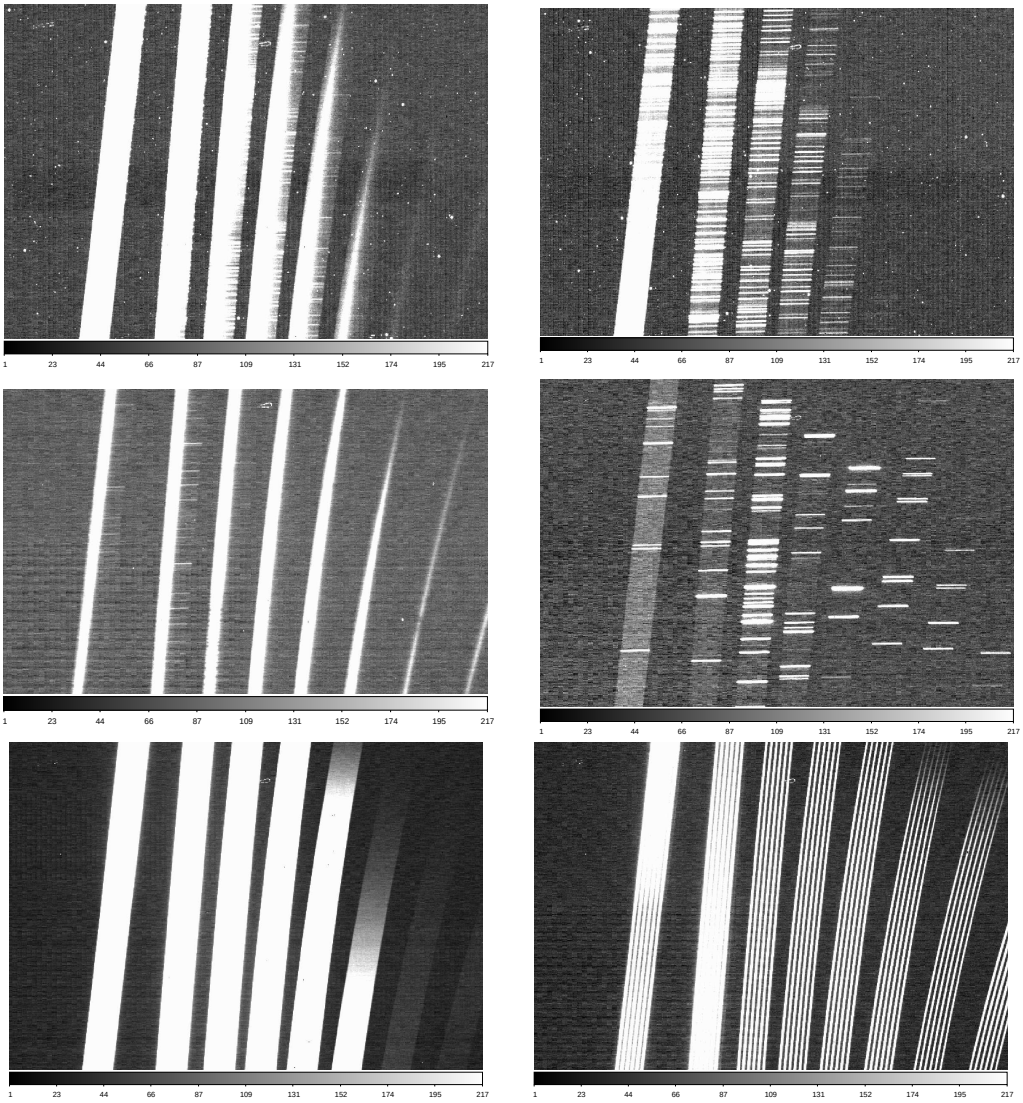

Figure 2.3: Examples of raw data obtained in the cross-dispersed mode. Top left: An example of a raw galaxy spectrum. The vertical stripes are different orders, starting with order 3 on the left (corresponding approximately to K band), and increasing along the x-axis. Wavelength runs along the y-axis, decreasing with increasing order, and increasing downwards within orders. The orders are tilted with respect to the detector. Top right: Example of a sky frame, when the telescope is nodded off the galaxy to a region of blank sky. Middle left: Example of a standard star. Middle right: An example of an arc frame, using an argon lamp. Bottom left: An example flat frame. Bottom right: An example pinhole flat frame, used for tracing the spectra.

images divided by the result.

Sky Subtraction

One of the main contributors to detector counts in the near-infrared is the night sky, which may produce even more counts than the target itself (Irwin et al. 2004). To correct for this, Gemini's standard observational technique for extended targets is to nod the telescope between the target and an empty region on the sky, and then subtract the latter from the former. The strength of sky emission varies on short timescales, necessitating the observation of sky frames as close in time to the science frames as possible. The pattern ABAABA was used, which gives a neighbouring sky frame to every galaxy exposure. The observation of neighbouring sky frames minimises flexure of the spectrograph while maintainig an on-source efficiency of 66%. The sky subtraction was carried out with the IRAF task *nsreduce*, which uses an automatic sky-object pairing algorithm to find the frames at the correct (sky) telescope position closest in time for each science frame. This sky frame is then subtracted from the science frame, removing the night sky emission lines, as well as other static artefacts in the detector, such as stable 'hot' pixels. Figure 2.4 shows a science frame before and after sky subtraction. The sky lines are typically removed well, although some residuals may be present due to temporal variations that are not tracked within the 120 s exposure, and there is also Poisson noise which cannot be removed.

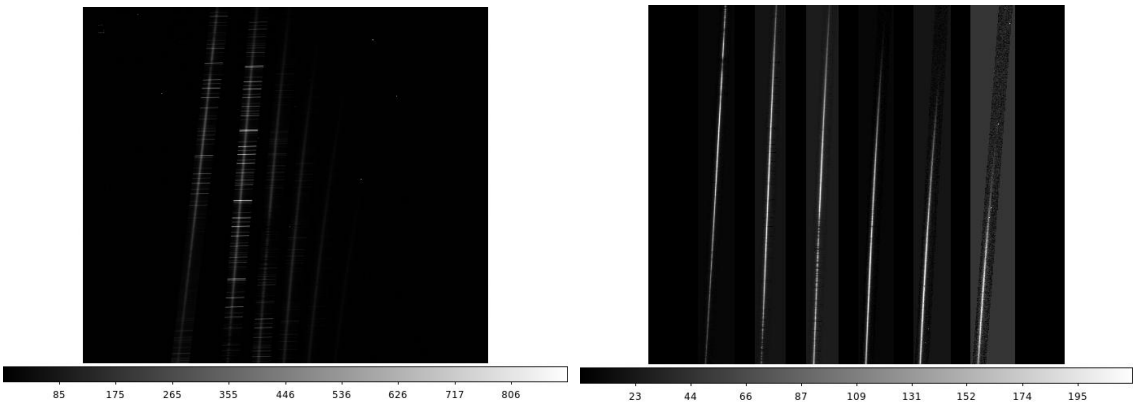

Figure 2.4: Left: Example data before sky subtraction. Right: Example data after sky subtraction. This data has also been cut into individual orders.

Wavelength Calibration and S-distortion Correction

At this stage the spectral and spatial axes of each order are tilted with respect to the detector pixels. The two axes need to be rectified to be linearly sampled in wavelength and

angular resolution. The pinhole mask acts as a spatial reference for the orders, giving light at regular intervals along the slit. The traces of the light peaks were fitted with an order 5 polynomial. This polynomial was then used to transform the spatial axis onto a regularly sampled grid of angular scale using the IRAF task *nssdist*. The position of the observed argon emission lines in detector pixels was compared to the known laboratory wavelengths, and a polynomial function fitted to these data using the IRAF task *identify*. This function is used to transform the dispersion axis onto a linearly sampled grid of wavelength using the IRAF task *nstransform*.

Aperture Extraction

1D spectra were then extracted from each order using IRAF task *apall*, which finds the peak of the spectrum, performs a spectral trace, and extracts a spectrum from each order in a fixed aperture size of ± 6 pixels, corresponding to ± 0.9" around the peak. This region encompasses most of the galaxy flux, while minimising contamination by sky, and it is large enough to be insensitive to seeing effects. The extraction was done in *apall* in order to enable the rejection of deviant pixels (due to, for example, poorly removed cosmic rays or radiation events). The extraction is carried out such that the sum is weighted by the signal to noise in each pixel – a process known as 'optimal extraction' (Horne 1986). Deviant pixels are rejected by assuming that variations in the shape of the spatial profile vary slowly with wavelength.

Telluric Correction

Ground based near-infrared spectroscopy suffers from strong and variable absorption features (telluric features) at certain wavelengths due to the Earth's atmosphere. This absorption varies with airmass and on timescales on the order of several to tens of minutes (Vacca et al. 2003). To correct for this absorption, a calibration star was observed close to the target immediately before or after each galaxy, and with the same instrument setup. These stars were chosen from the Hipparcos Catalog[2] (Perryman et al. 1997), and were of type $\mathrm{A0} - \mathrm{A4}$ as shown in Table 2.3. These telluric data were then reduced in the same way as the galaxies.

Since these stars are hot, their continuum can be well approximated by a black-body spectrum of the same effective temperature, with certain intrinsic stellar features superimposed. These intrinsic features are predominantly strong hydrogen lines, which can usually be fitted and separated from the telluric absorption. Before applying the telluric correction, the star's intrinsic hydrogen lines were removed by interactively shifting and scaling a model spectrum

[2]using the tool http://www.gemini.edu/sciops/instruments/gnirs/nir-resources?q=node/10165

spectrum of the star Vega (Kurucz 1993), leaving a spectrum containing telluric features only. Figure 2.5 shows order 8 of a telluric star before and after removal of its hydrogen lines.

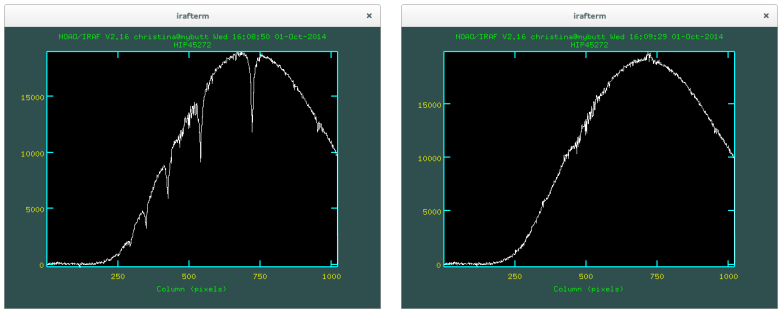

Figure 2.5: Standard star before (left) and after (right) removal of intrinsic hydrogen lines.

IRAF's *telluric* task was then used to interactively shift and scale the (intrinsic-line free) telluric star spectra to achieve the best telluric removal in the science target. Figure 2.6 shows the telluric correction in the K-band.

Flux Calibration

The next step is to convert the measured photon counts into flux units of ergs s^{-1} cm^{-2} $Å^{-1}$. The telluric star's K-band magnitude is used as a flux calibration reference. Each order of the science target is multiplied by a black body function of the telluric star's temperature, scaled to the value of the star's K band magnitude as taken from 2MASS. This gives a rough flux calibration. Finally, the orders are joined together using the IRAF task *odcombine*, which ensures a smooth overlap region between the different orders.

2.4 Spectra

The final output of the reduction process are the twelve 1D spectra shown in Figure 2.7. The spectra have been corrected for recession velocity. The grey regions indicate wavelengths where the atmospheric transmission model of Lord (1992) is $\leq 50\%$, assuming a water vapour column of 1.6mm and an airmass of 1.0.

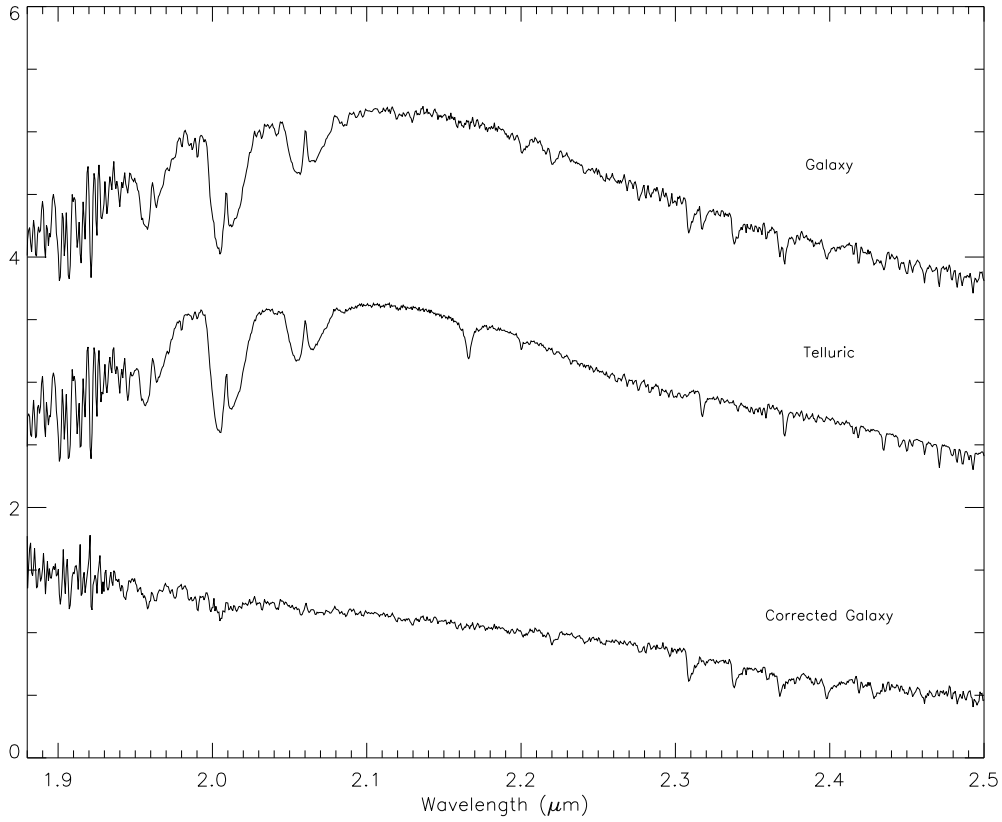

Figure 2.6: Example of telluric correction in the K band. Top: Extracted, sky-subtracted galaxy spectrum of NGC 3032. Middle: Spectrum of telluric star HIP44512, reduced in the same way as the galaxy and before removal of the star's intrinsic absorption features. Bottom: Telluric-corrected galaxy spectrum.

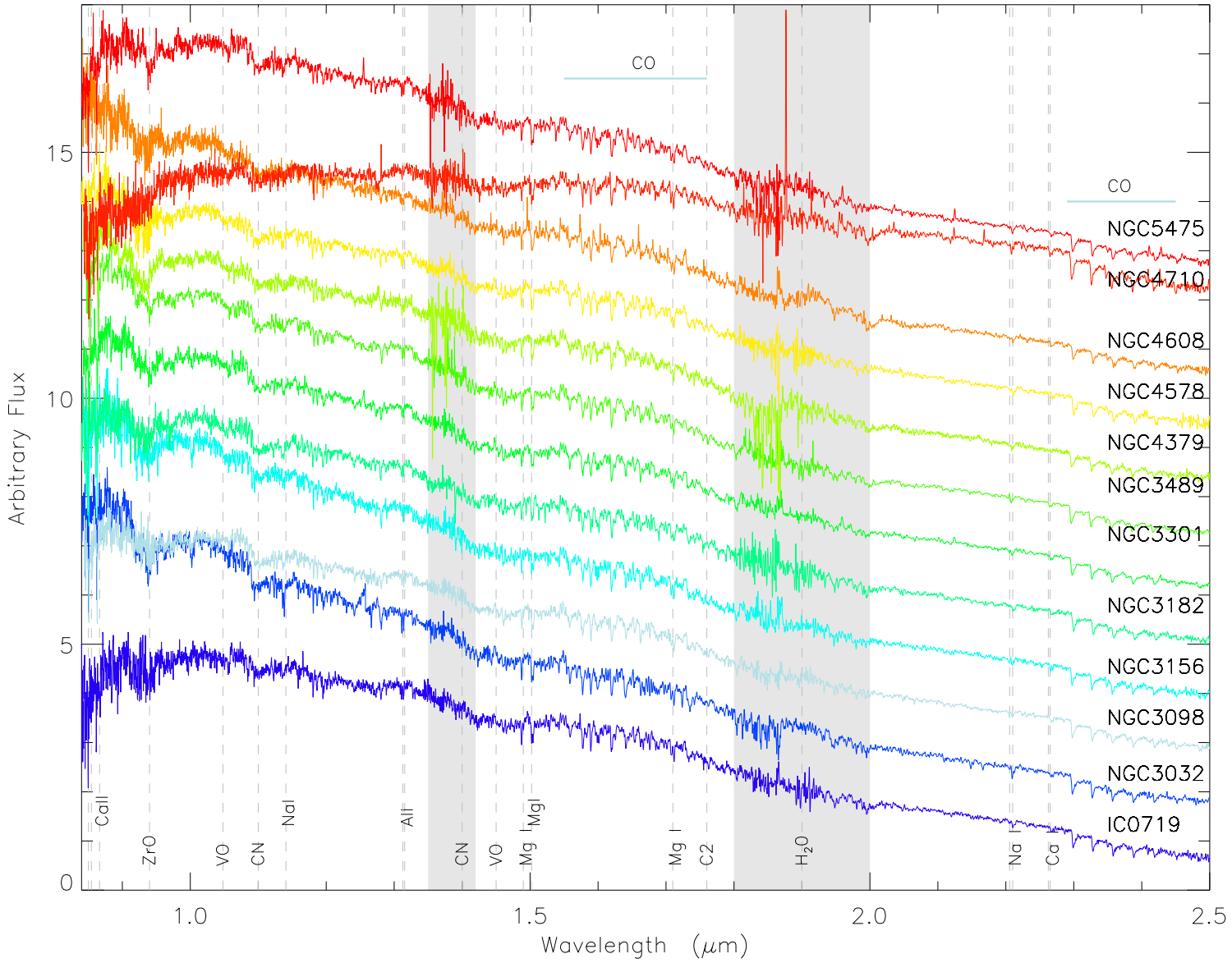

Figure 2.7: Reduced spectra of the twelve galaxies in the sample. The shaded areas indicate regions of strong atmospheric absorption. Each spectrum is normalised to its median value and offset for display purposes.

Chapter 3

Overview of the spectra

The full near-infrared SEDs of the twelve galaxies in the sample are shown in Figure 3.1. In this and all subsequent figures, the galaxies are ordered by their optical SSP-equivalent age from McDermid et al. (2014), unless otherwise stated. Regions of poor atmospheric transmission (as defined in Section 2.4) are shown on the plot in grey. A simple visual inspection of the spectra reveals a striking lack of variation between galaxies. The similarity of the near-infrared region is surprising as the galaxies span span 14 Gyrs in age as measured from single stellar populations applied at optical wavelengths (McDermid et al. 2014). The spectrum of each galaxy has the same overall shape, with the exception of NGC 4710, which exhibits a downturn at shorter wavelengths. However NGC 4710 has a relatively high molecular gas fraction compared with the other galaxies in this sample (Young et al. 2013), which indicates that significant amounts of dust may be present (Young and Scoville 1991), giving increasing amounts of extinction at bluer wavelengths (Calzetti 2001). Visual inspection of the SDSS image (Figure 2.2) confirms this.

All other galaxies display a gradual decrease in flux with increasing wavelength. They feature prominent breaks at $\sim$ 0.9 μm and $\sim$ 1.1 μm as well as changes in slope at $\sim$ 1.4 μm and $\sim$ 1.7 μm. Comparing Figure 3.1 with Figure 2.7 (which is plotted on the same scale, but ordered alphabetically), it appears to be the case that age plays a role in overall spectral shape. Figure 2.7 has clear overlap between spectra – IC 0719, NGC 3098, NGC 3182, NGC 4379, NGC 4710 and NGC 5475 all display a decrease in flux at the blue end compared with the others. These same galaxies all lie in the top half of Figure 3.1, indicating that young galaxies tend to be steeper than old galaxies.

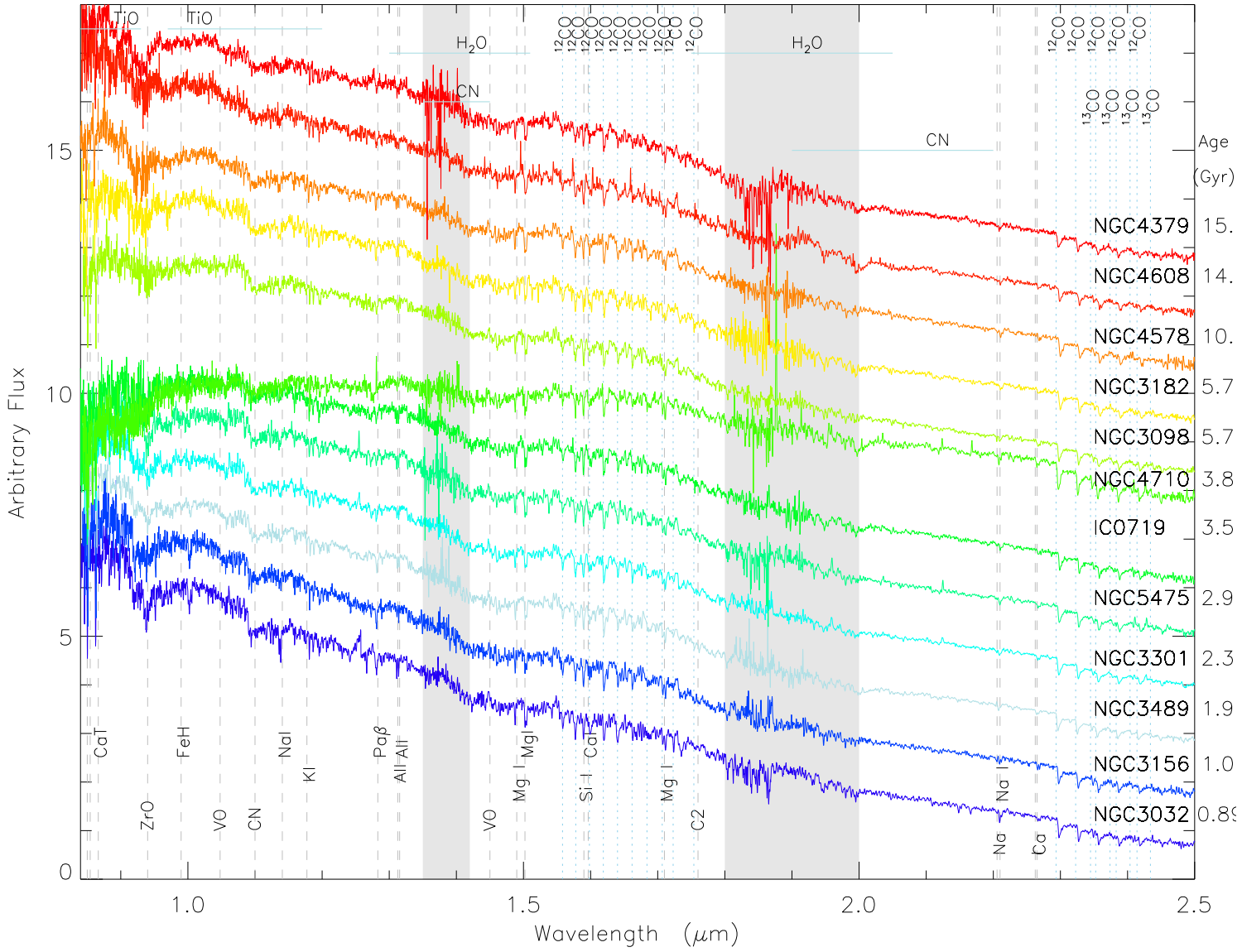

Figure 3.1: Near-infrared spectra of the sample of galaxies. The spectra are normalised to their median value and shifted by a constant for display purposes. The shaded boxes mark regions of poor atmospheric transmission between the near-infrared J, H and K bands. The spectra are corrected for recession velocity and sorted according to age, with age increasing upwards. Important atomic features are marked with dashed lines, and molecular bands with horizontal bars and dotted vertical lines.

To show more detail, Figures 3.2 to 3.5 show shorter wavelength ranges, roughly corresponding to the I/Z, Y/J, H and K passbands. All galaxy spectra are clearly dominated by stellar absorption lines and molecular bands. The locations of the main atomic features (identified using Rayner et al. 2009) are marked on the plots with dashed lines. Broad molecular bands are marked either with horizontal bars or dotted vertical lines. The plots show clearly that the same features are present in all galaxies.

3.1 The I/Z and Y/J band

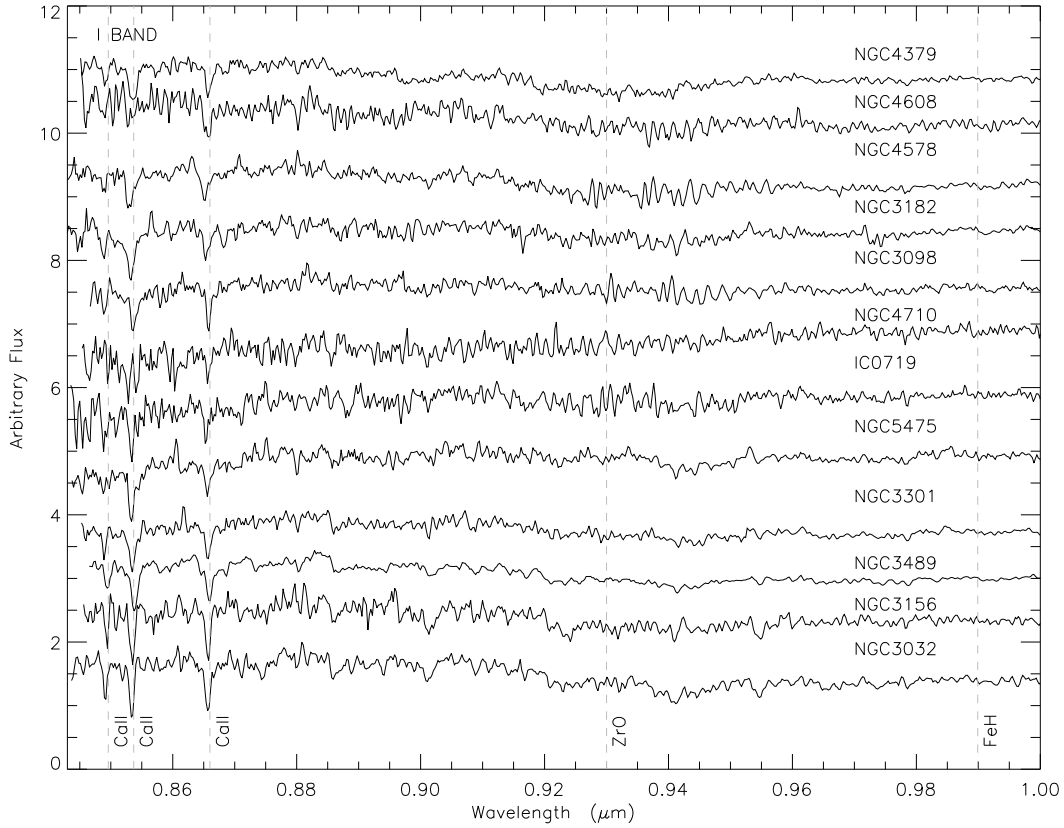

Figure 3.2: I/Z-band portion of the final reduced galaxy spectra. The main absorption features are marked with dashed lines and molecular bands with horizontal bars.

There are a number of interesting features blueward of 1.5 μm. The I- and J-bands contain the well studied calcium II triplet (CaT) at λ 0.84, 0.85, 0.86 μm and the FeH Wing-Ford band at λ 0.99 μm as well as a number of other absorptions due to Na I at λ 1.14 μm, Paβ at λ 1.28 μm and Al I at λ 1.31 μm. As these data were obtained to study stronger absorption features such as the 1.1 μm CN break predicted to be prominent in TP-AGB stars, and the signal-to-noise in this band is not the highest, some of these features are not noticeable in

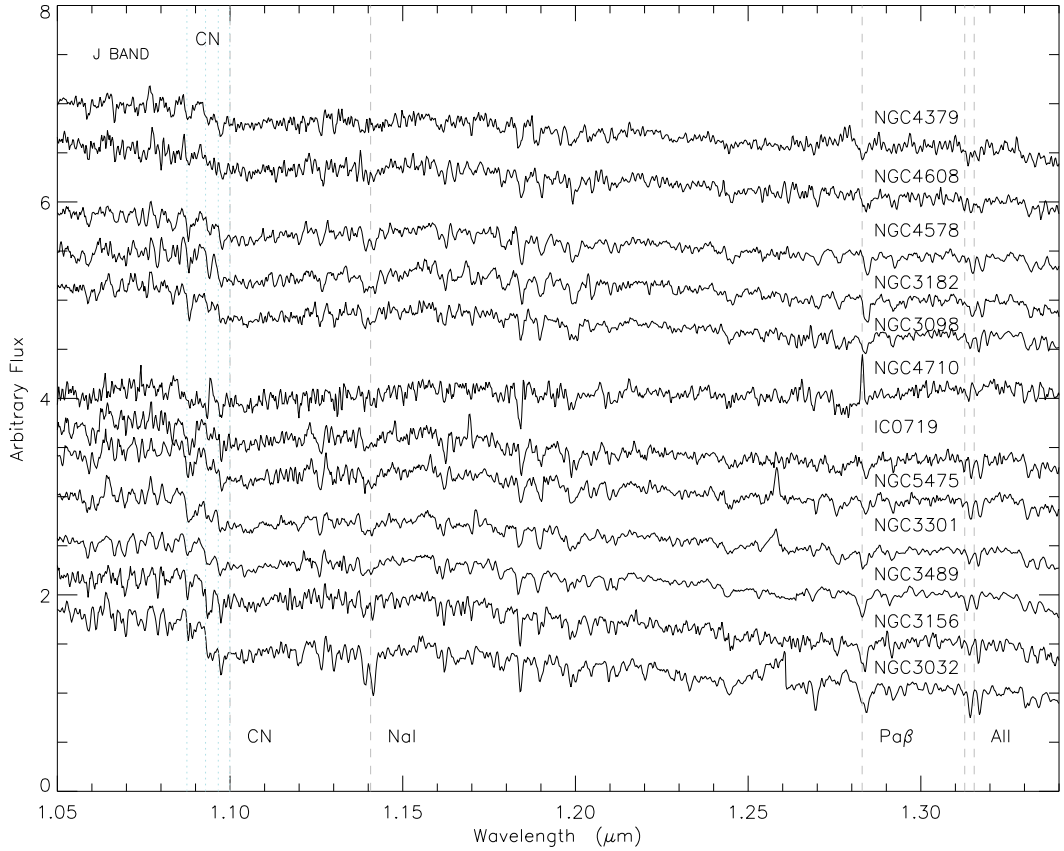

Figure 3.3: Y/J-band portion of the final reduced galaxy spectra. The main absorption features are marked with dashed lines. Paβ can be seen in NGC 4710 in emission.

these spectra.

The FeH Wing-Ford band is an IMF-sensitive feature, appearing only in the spectra of late-type M dwarfs (Conroy and van Dokkum 2012). This feature is weak or not easily detected in these spectra, perhaps due to limitations in S/N. CaT traces Ca which is an alpha element, and should be enhanced compared to Fe in giant ellipticals, however studies show that Ca seems to follow Fe (Cenarro et al. 2003). The strength of CaT is a strong function of surface gravity (being enhanced in giants but weak in dwarfs) and a weak function of metal abundance (Jones et al. 1984; Diaz et al. 1989). Na I is an alpha element which is sensitive to low mass stars, so a strong Na I feature indicates both a high [Na/Fe] abundance and an overabundance of dwarf stars (Alloin and Bica 1989; Cohen 1978; Carter et al. 1986). Other features in this wavelength range (KI, Paβ, Al I) were identified by Conroy and van Dokkum (2012) as IMF-sensitive features. Paβ is visible in emission in NGC 4710.

Cool late-type stars (such as M giants and TP-AGB stars) display a number of prominent absorption bands over the $0.8 - 1.5$ μm range. A number of these are visible in the I/Z- and Y/J-bands. Particularly noticeable are two broad, strong features at ~ 0.94 μm and 1.1 μm.

The feature at 0.94 μm is likely due to a blend of TiO, ZrO and CN, as identified using the table of molecular features in Rayner et al. (2009). The break at 1.1 μm is due to CN, and possibly an overlapping band of TiO. These features are all due to molecules present in the atmospheres of cool stars, including the TP-AGB stars that we are concerned with in this study. The CN feature is of particular importance to this study, being a tracer of age in the M11 models we are testing. From study of individual stars, CN shows a strong temperature dependence, increasing in strength with decreasing temperature, and it is only present in the coolest stars ($T_{\rm eff} < 5500$ K; Malkan et al. 2002).

3.2 The H band

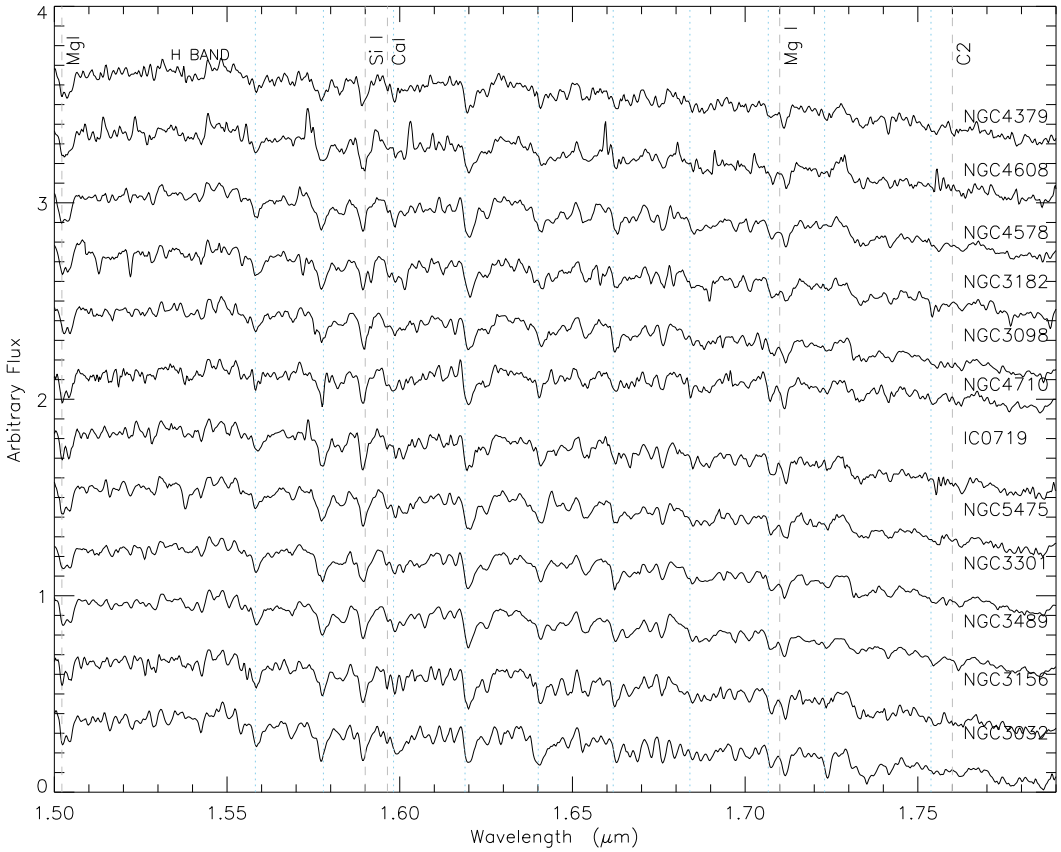

Figure 3.4: H-band portion of the final reduced galaxy spectra. The main absorption features are marked with dashed lines. CO rotation-vibration bands are shown with blue dotted lines.

The H band shows multiple strong features in every galaxy. These are second CO overtone rotation-vibration bands, which are easily identified based on a comparison with Figure 31 of Rayner et al. (2009). There are also a number of atomic features present in this region

including Si I, Mg I and Ca I. A C_2 band at 1.78 μm is expected to be strong in TP-AGBs, however it lies just outside of the H-band in a region of poor atmospheric transmission.

3.3 The K band

There are few features in the K band. The most obvious is the CO bandhead at 2.29 μm. The galaxies also display a small amount of absorption from sodium (Na) and calcium (Ca). The CO bandhead at $\sim 2.29 - 2.5$ μm is known to be strong in late-type giants and supergiants and become progressively weaker with decreasing luminosity (Rayner et al. 2009; Persson et al. 1980) It does not depend on metallicity (Frogel et al. 1978).

The molecular H_20 band near 2 μm is a sensitive function of effective temperature. Strong H_20 absorption is indicative of a population of giants at least as late as M5 (Aaronson et al. 1978).

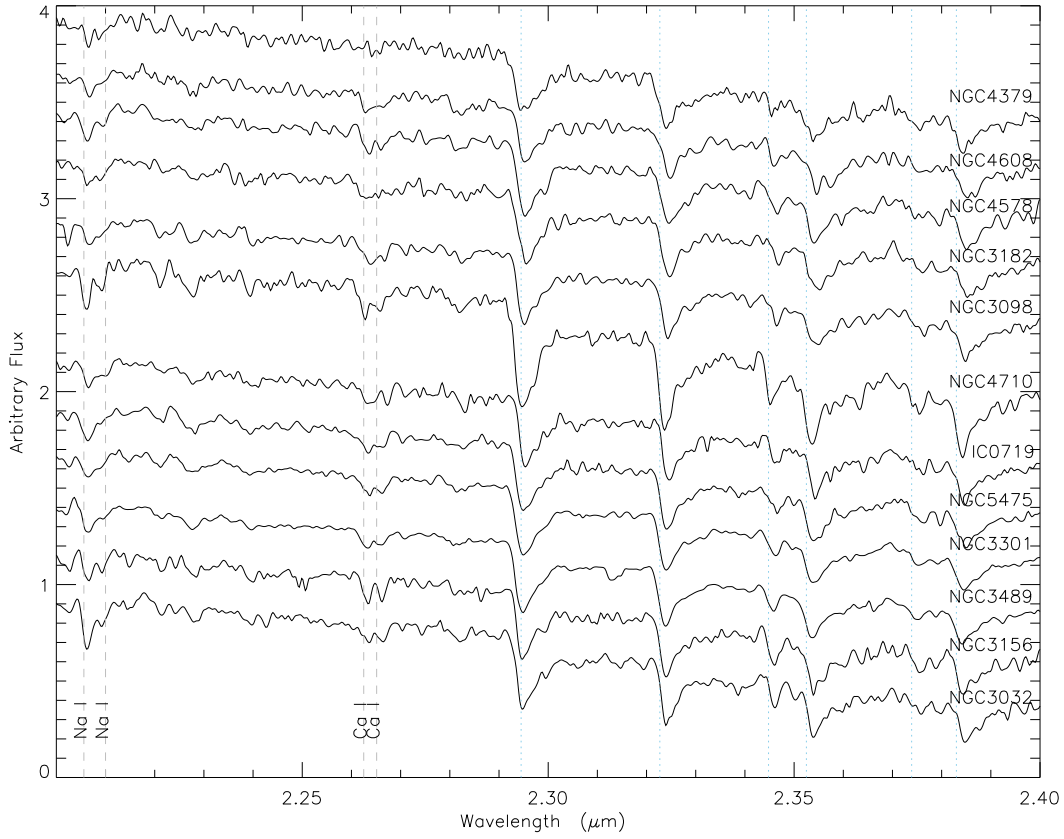

Figure 3.5: K-band portion of the final reduced galaxy spectra. The main atomic features are marked with dashed lines. CO rotation-vibration bands are shown with blue dotted lines.

3.4 Emission Lines

All galaxies in this sample are dominated by stellar absorption lines. However three galaxies (NGC 3301, NGC 4710 and NGC 5475) also display weak emission lines. These are due to H_2 emission[1] at 2.12 μm, 1.26 μm, 2.17 μm, 2.40 μm and 2.42 μm. Paβ at 1.28 μm is also visible in the spectra of NGC 4710. These galaxies display strong emission lines in their optical spectra. However, optical emission is the norm amongst this sample. NGC 3301 and NGC 4710 are classified as transition objects based on their optical spectra (as are IC 0719 and NGC 3032), while NGC 5475 is classified as a LINER/AGN (along with NGC 3489). NGC 3156 and NGC 3182 are classified as Seyferts, and NGC 3098 is classified as having central LINER-like optical emission, while NGC 4379, NGC 4578 and NGC 4608 display no optical emission (Marc Sarzi, private communication). Essentially, there is poor correspondence between optical and near-infrared emission. This may be due to probing different regimes of the gas (molecules vs ionized atomic) and/or sensitivity (GNIRS is lower S/N than SAURON, which obtained the optical data).

3.5 Optical Properties

We include here in Figure 3.6 the optical spectra of these galaxies as observed by ATLAS^{3D} with the SAURON spectrograph. The figure shows the spectra after the emission lines of [OIII] and Hβ have been subtracted. The systematic variation in the strength of age indicators Hβ and (to a lesser degree) Mg b led to the derivation of SSP-equivalent ages ranging from 0.89 Gyr to 15.54 Gyr by McDermid et al. (2014). This is in contrast to what we see in the infrared spectra, which display no clear systematic variation. The inclusion of the SAURON spectra here also demonstrates the high signal-to-noise ratio of our optical data, supporting our assumption that the properties determined from these data give a secure benchmark with which to test predictions in the infrared.

[1] identified using http://www.reunanen.ftml.net/public/linelists/hmol.html

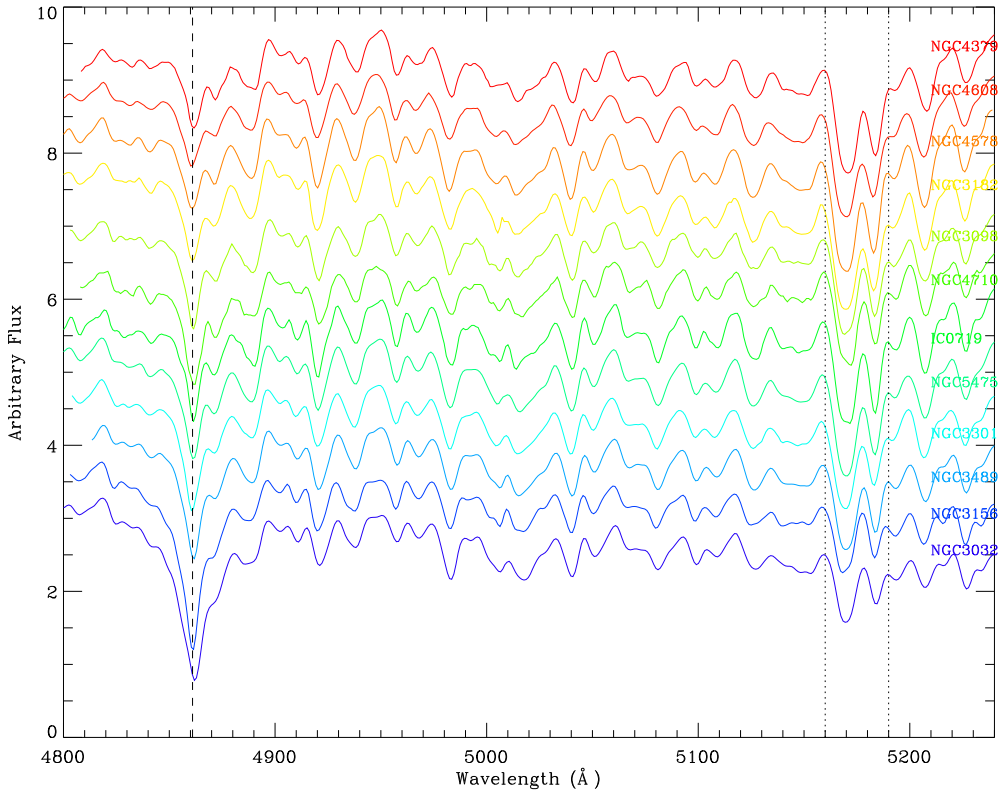

Figure 3.6: Cleaned optical spectra taken with SAURON (McDermid et al. 2014). Spectra are normalised to unity and offset for display. Hβ is marked with a dashed line and the bounds of Mg b are marked with dotted lines.

Chapter 4

Model Predictions

4.1 Stellar Population Synthesis models

There are a number of Stellar Population Synthesis (SPS) models currently in use. Popular models include GALAXEV (Bruzual and Charlot 2003), Maraston (Maraston 1998, 2005; Maraston and Strömbäck 2011), FSPS (Conroy et al. 2009; Conroy and Gunn 2010), PEGASE (Fioc and Rocca-Volmerange 1997), Vazdekis et al. (1996), MILES (Vazdekis et al. 2010), MIUSCAT (Vazdekis et al. 2012) and Schiavon (2007).

This thesis focuses on three sets of models: Bruzual and Charlot (2003), Maraston and Strömbäck (2011), and Conroy et al. (2009); Conroy and Gunn (2010). These three were chosen as they each provide predictions of the medium-resolution near-infrared spectral energy distributions (SEDs) for a range of ages and metallicities, allowing us to make direct spectral fits to our observational data. These three models also account for the TP-AGB phase in different ways, allowing us to test which approach is best.

The aim of this thesis is to apply these three SPS models and compare how well they can reproduce the near-infrared spectra of our sample of early-type galaxies. This section describes the models and outlines the main features predicted by each.

The Bruzual & Charlot Models

The Bruzual & Charlot Models (hereafter BC03), use the Padova 1994 tracks (Alongi et al. 1993; Bressan et al. 1993; Fagotto et al. 1994) supplemented with the Vassiliadis and Wood (1993) models for TP-AGB stars and the Vassiliadis and Wood (1994) models for post-AGB stars. The default stellar spectral libraries are the empirical STELIB library (Le Borgne et al. 2003), extended with the semi-empirical BaSeL library (Westera et al. 2002) for ultraviolet and near-infrared predictions. STELIB is made up of 249 stars at a resolving power of

R = $\lambda/\Delta\lambda \approx 2000$ (FWHM $\sim$ 3Å), while the BaSeL library has resolving power of $\sim$300. BC03 also offer the option of generating solar metallicity SEDs extending to the near-infrared using the Pickles library, which has a resolution of $R \sim 500$. BC03, as well as most other current models (including FSPS) use the isochrone synthesis technique to calculate SEDs. This technique integrates the spectra of all the stars along an isochrone to compute the total flux for a population of a particular age. As isochrones are built in discrete time steps, this approach struggles to account for brief post-Main Sequence phases such as the TP-AGB phase, leading to a low contribution from stars in this phase. More recent versions of the Bruzual & Charlot models have increased contributions from the TP-AGB compared with the 2003 models (Bruzual 2006). These models are distributed on demand, however they are not fully documented. As such, we elected to analyse the widely used BC03 models.

The Maraston Models

There have been a number of iterations of the Maraston models. The current version comprises the Maraston (2011) (hereafter M11) models, which are a higher-resolution version of the M05 models. They use the isochrones and stellar tracks by Cassisi et al. (1997) up to the Main Sequence turn-off, after which time they use the fuel consumption theorem of Renzini (1981) to calculate the energetics of post-Main Sequence (PMS) stages of stellar evolution such as the TP-AGB phase. With this technique, the luminosity of PMS stars is proportional to the amount of nuclear fuel burned in each PMS phase, making the contribution of each phase independent of the details of stellar evolution. The specific contribution of the TP-AGB phase at each age was calibrated against Magellanic Cloud globular clusters. This treatment of PMS phases leads to very different predictions than those given by traditional SPS models, with the TP-AGB strongly impacting the near-infrared SEDs of intermediate age populations.

For the stellar spectra, the Maraston models offer the option of four different libraries of flux-calibrated empirical stellar spectra, namely Pickles (Pickles 1998), ELODIE (Prugniel et al. 2007), STELIB (Le Borgne et al. 2003) and MILES (Sánchez-Blázquez et al. 2006; Cenarro et al. 2007), as well as the MARCS (Gustafsson et al. 2008) library of very high resolution theoretical stellar spectra. The Pickles library was utilised in this study, as it is the only library to cover both the wavelength range and ages of interest. Pickles contains 131 flux calibrated spectra covering all normal spectral types and luminosity classes at solar abundance, and metal-weak and metal-rich F-K dwarf and G-K giant components. The library covers a wavelength range of 1150 Å to 2.5μm at a resolving power R $\approx$ 500. STELIB and ELODIE do not span the relevant wavelength range (STELIB covers 3201.0–9296.5 Å, and ELODIE 3900.0–6800.0 Å), while the MILES and MARCS libraries cover the near-

infrared range, but not the required ages (both generate near-infrared SEDs for 3–15 Gyr), thus missing the ages where the TP-AGB phase is expected to dominate.

The Conroy Models

The Flexible Population Synthesis models (FSPS) by Conroy et al. (2009); Conroy and Gunn (2010) are designed to give the user control over uncertain phases of stellar evolution such as the TP-AGB phase. They use stellar evolution tracks from the Padova group (Marigo and Girardi 2007; Marigo et al. 2008). They use the semi-empirical BaSeL3.1 library (Lejeune et al. 1997, 1998; Westera et al. 2002), supplemented with empirical TP-AGB spectra from the library of Lançon and Mouhcine (2002).

The 'flexibility' in the Flexible Population Synthesis models is that users may modify the bolometric luminosity and effective temperature of the TP-AGB phase via parameters ΔL and ΔT which are introduced in these models. Originally these shifts were with respect to the Padova tracks, however the current models set the default values of L and T to the best-fit values calculated in Conroy and Gunn (2010). We used the default values for this thesis, leaving a full exploration of these parameters as the topic of future work.

4.2 Preparation of Models

In order to make a valid comparison between the different models, we restricted our analysis to the subset of parameters common to all models. For each model, SSP templates were generated covering the wavelength range 8400–25000Å in 1 Gyr time steps for ages 1–12 Gyrs at solar metallicity. This subset was common to all models, and also spans approximately the same parameter space covered by McDermid et al. (2014) who analysed this same sample at optical wavelengths, and calculated star formation histories binned in 1 Gyr time steps from 1–14 Gyr. As the subsample for this study was selected from the complete ATLAS^{3D} sample with the criterion of being approximately solar metallicity, limiting the metallicity of the models to solar (which is the only metallicity available for the M11 models in this age/wavelength range) is also appropriate.

SSP templates were generated for all models assuming a Salpeter IMF, which is the IMF traditionally considered to be most appropriate for ETGs. There are currently indications that IMF may not be universal, and indeed, that it may even vary within the class of ETGs, from a light Chabrier-like IMF to one even heavier than Salpeter depending on galaxy mass (Cappellari et al. 2012). However, the choice of a Salpeter IMF is in line with previous stellar population studies and should not greatly impact our overall conclusions.

To ease comparison between the three models, each of which is based on a spectral library with a particular resolution, we degraded the resolution of the data to match the resolution of the library when carrying out spectral fitting. This is described further in Chapter 6. The spectral libraries used in the study are listed in Table 4.1.

Table 4.1: SPS models. The libraries selected for this study are in bold.

SPS Model	Stellar Tracks	Spectral Library	Library Type	Wavelength Range	Median Resolution	Metallicities ($Z_\odot$)
M11	Cassisi	**Pickles**	**Empirical**	**1005 − 25000 Å**	**500**	**0.02**
		Miles	Empirical	3500 − 7429 Å	2.54 Å	0.0001, 0.001, 0.01, 0.02, 0.04
		Elodie	Empirical	3900 − 6800 Å	0.55 Å	0.0001, 0.01, 0.02, 0.04
		Stelib	Empirical	3201 − 9296 Å	2000	0.01, 0.02, 0.04
		Marcs	Theoretical	1299 − 199948 Å	20,000	0.0001, 0.02, 0.04
BC03	Padova	**Pickles**	**Empirical**	**1005 − 25000 Å**	**500**	**0.02**
		Stelib	Empirical	3201 − 9296 Å	2000	0.01, 0.02, 0.04
		BaSeL	Empirical	91 Å − 160 μm	300	$10^5 - 10$
FSPS	Padova	**BaSeL**	**Empirical**	**91 Å−160 μm**	**300**	$\mathbf{10^5 - 10}$

4.3 Model Predictions

4.3.1 Comparison between models

Figure 4.1 shows a comparison between intermediate age and old SSPs for each model. The left hand panel shows the spectrum of a 1 Gyr SSP generated by each model: this is approximately the age at which the contribution of the TP-AGB phase is thought to be maximum. The right hand panel shows a 12 Gyr SSP generated by each model: in this instance the contribution from the TP-AGB phase should be negligible. The large contribution from the TP-AGB phase in the M11 models causes strong, sharp drops to be present throughout the near-infrared spectral range of intermediate age SSPs. Two of these fall in the regions of poor atmospheric transmission surrounding the H band, however in all cases a large drop in flux over a short wavelength range can be clearly discerned. These drops are due to carbon molecules present in the atmospheres of stars which have repeatedly gone through the third dredge-up and become C stars. These features are not present in the old M11 SSPs, which display a smooth decline in flux with increasing wavelength. The strong breaks of the M11 models are replaced by rounded bulges in the FSPS models, which are present in both young and old populations, although at different strengths. The FSPS bulges occur at approximately the same wavelengths as the break features in the M11 SSPs.

In contrast to the other two models, the 1 Gyr BC03 SSP displays a gradual decline in flux over the near-infrared range, without the presence of any large features. The 12 Gyr SED has a similar shape to the FSPS SSP of the same age.

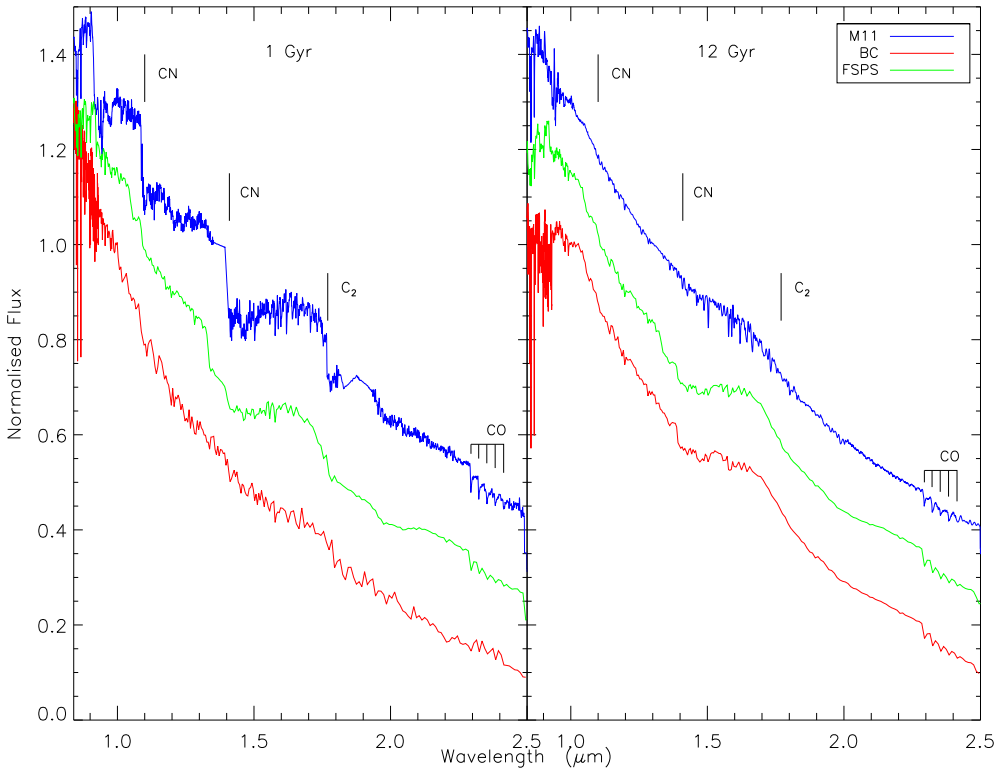

Figure 4.1: Comparison between SSPs as derived from M11 models (blue lines) FSPS models (green lines) and BC03 (red lines). Left: at the peak of the TP-AGB phase ($\sim$ 1 Gyr). Right: old SSPs (12 Gyr). The SEDs are normalised to unity at 1 μm and offset for display purposes

4.3.2 Age progression

This section describes the age progression of the different models. Figures 4.2 to 4.4 are ratio plots showing the variation within in each model with age. Each subplot shows an SSP of a given age divided by a 12 Gyr SSP, giving the ratio of the fluxes between the two ages.

Figure 4.2 shows the expected variation in feature strength with age in the BC03 models. The youngest models have higher flux, particularly towards the blue end of the near-infrared range. The 1 Gyr template has stronger features than the oldest throughout the whole range, particularly at the CO bandhead. After 2 Gyr, there is little variation between models.

Figure 4.3 shows the expected variation in the M11 models. It can be seen that the strong carbon features predicted by M11 are present in the model SEDs only of populations < 2 Gyr.

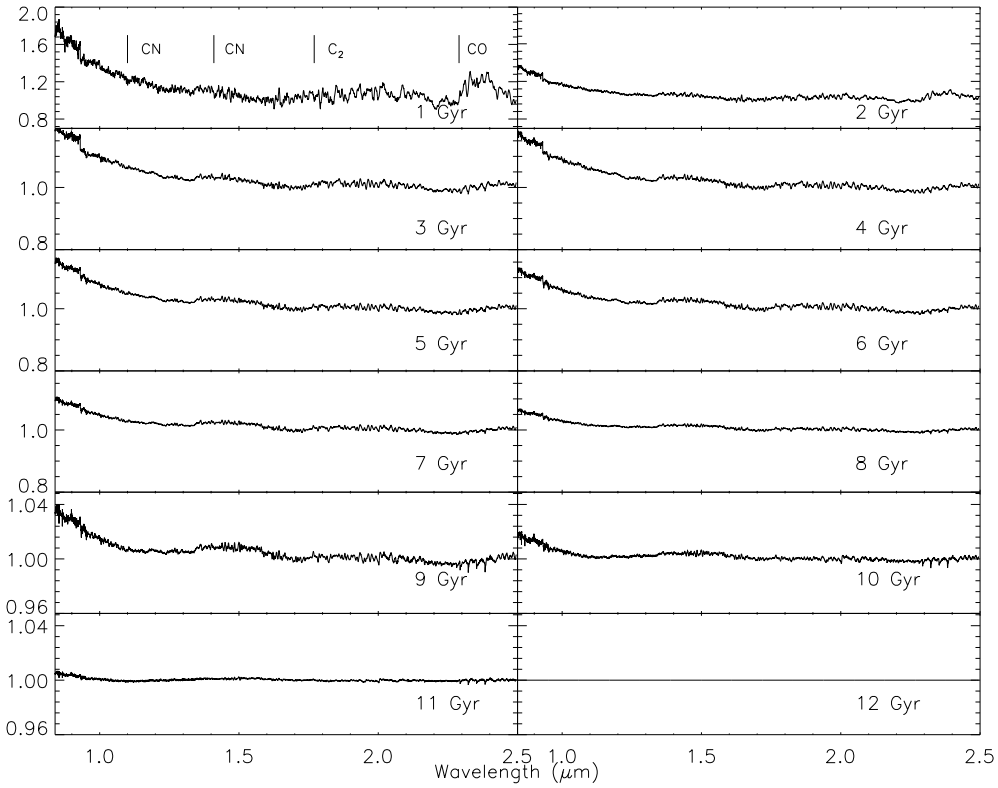

Figure 4.2: Variation of the BC03 models with age. Each plot shows an SSP of a certain age divided by a 12 Gyr SSP. The age of the varying SSP is given in the plots. Note that the scale varies between subplots.

There are clear strong, sharp drops at $\sim 0.9\mu$m, $\sim 1.1\mu$m, $\sim 1.4\mu$m and $\sim 1.8\mu$m. The 0.9μm feature is due to a blend of molecules present in late-type stars, the features at 1.1μm and 1.4μm are CN, and the 1.8μm feature is due to H_2O. The strength of these features peaks at 1 Gyr and then declines. The variation in the strength of this feature between young and old models is on the order of 20%. Templates > 3 Gyr show little variation, displaying some decrease in overall flux with increasing age, and a decline in the strength of the many H band features between $1.4 - 1.8$ μm and the CO bandhead at 2.29 μm, on the order of $\sim 1\%$. Old templates ($\gtrsim 9$ Gyr) display negligible variation.

The same plot for the FSPS models is shown in Figure 4.4. The youngest FSPS models also display strong molecular features, similar to those seen in M11. There is a feature present at ~ 1.1 μm in the FSPS models, as well as a larger break at ~ 1.3 μm. The models display a prominent bulge in the H-band, due to a minimum in the opacity of H^- at $1.6\,\mu$m, and another in the K-band. The variation in the strength of these features with age is on the same scale as the variation in the strong M11 features (i.e. on the order of $\sim 20\%$). In the case of FSPS however, the strength of these features peaks later, at 2 Gyr, before declining in the old models. The strength of the CO bandhead and the H-band features decrease with

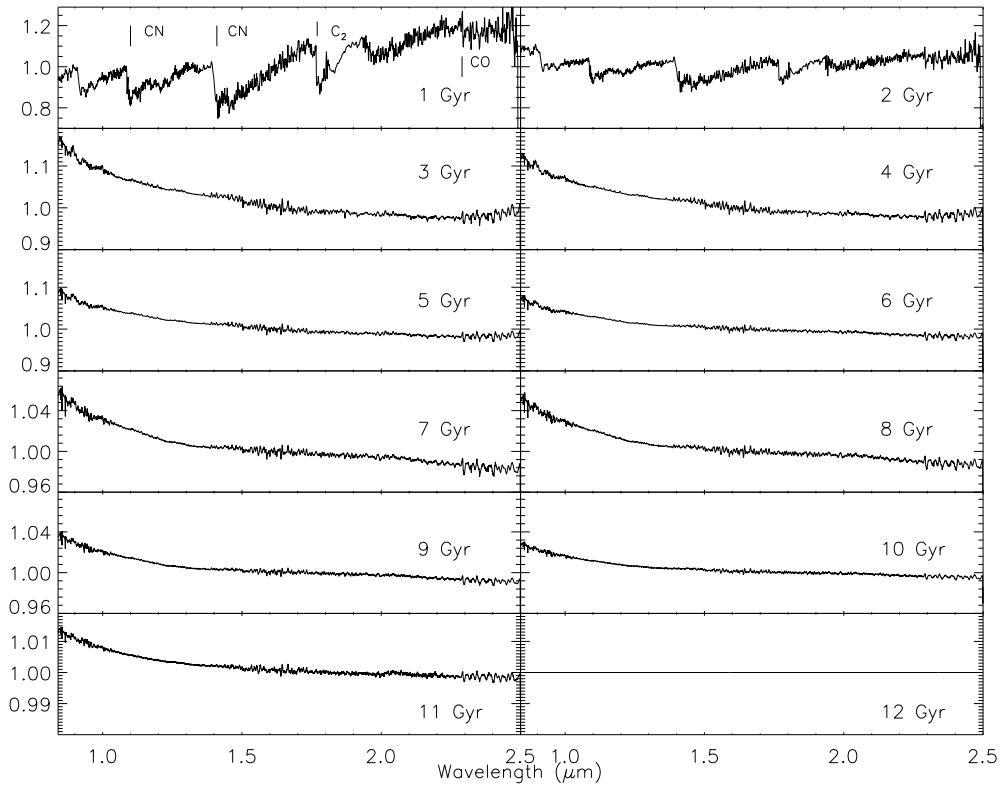

Figure 4.3: As Figure 4.2 but for M11.

age, similar to what we see in the other two models.

To summarise, the BC03 models display a gradual decline in the strength of major features with age, while maintaining the same approximate shape. Intermediate age M11 models have quite a different shape to the old models, with strong sharp drops visible throughout the near-infrared range that are not present in SEDs of populations 3 Gyr and above. The FSPS models display similarly strong features, but with broader, smoother shapes than M11, and these features remain visible until older ages (10% amplitude still at 5–6 Gyr), decreasing only gradually with age.

4.3.3 Line Strengths

As seen above, each model predicts the strength of certain features to vary with age. By measuring the equivalent widths of these age-dependent features, we can accurately quantify how well the models predict these specific spectral features. From the ratio plots we can see that the main age-sensitive features in the NIR range are carbon-related features, including the strong breaks visible in the M11 models and the CO bandhead. The molecular carbon features seen in M11 vary strongly with age, making them ideal age tracers, in principle. The CO bandhead is also a strong, isolated feature which is easy to measure and varies with age.

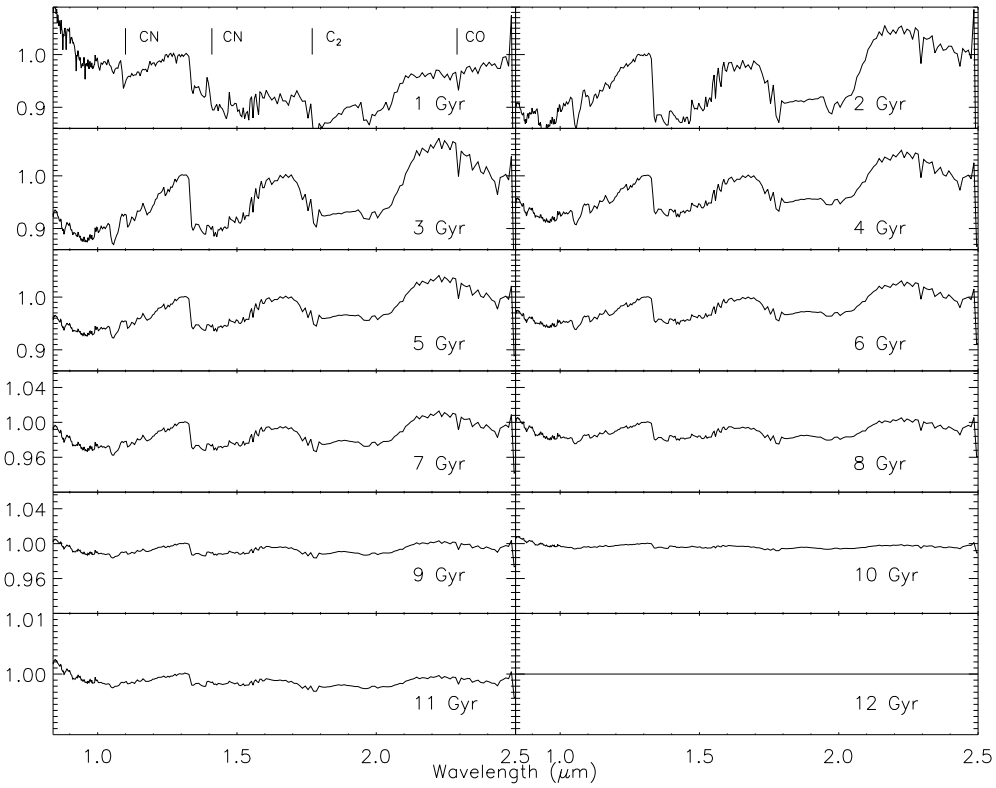

Figure 4.4: As Figure 4.3 but for FSPS.

As the features at ~ 1.4 μm and ~ 1.8 μm fall into regions of poor atmospheric transmission, making them unable to be measured, we restrict our line strength analysis to the 1.1 μm CN feature and the 2.29 μm CO feature.

To measure the strength of these absorption features we follow a procedure similar to that used for the measurement of Lick indices in the optical. Line strength indices are typically defined by a central bandpass covering the feature of interest, flanked by two pseudocontinuum bandpasses, one to the red side of the feature and one to the blue. The strength of the feature is usually calculated as an equivalent width following Equation (4.3.1)

$$\mathrm{EW} = \int_{\lambda_1}^{\lambda_2} \left(1 - \frac{\mathrm{S}(\lambda)}{\mathrm{C}(\lambda)}\right) \mathrm{d}\lambda \tag{4.3.1}$$

where $\mathrm{S}(\lambda)$ is the observed spectrum and $\mathrm{C}(\lambda)$ is the local pseudocontinuum, which is calculated by finding the average flux in middle of each pseudocontinuum bandpass and joining these points with a straight line, as shown in Figure 4.5. The difference in flux between this line and the portion of the spectrum within the central bandpass is the strength of the feature. Index strengths are usually measured in angstroms (Å).

CN Index The CN break is predicted by the M11 models to be prominent in galaxies of intermediate age (0.2–2 Gyr). Based on these models, we expect the youngest galaxies in our sample to show strong evidence of this feature, which should peak at $\sim$ 1 Gyr, be weaker by 2 Gyr, and not be visibly present in the spectra of galaxies over 3 Gyr. This index was previously defined by Riffel et al. (2007) using the M05 models, which follow the same prescription as the M11 models, but at a lower resolution. The central bandpass as defined by Riffel thus extends both blueward and redward of the feature in the native (higher) resolution galaxy spectra. However, to allow a direct comparison of all models, we measure the index at the lowest resolution common to all models and data. This is set by the FSPS models ($R \sim 300$), at which resolution the index is a good match to the feature. The CN feature is measured in the usual fashion for equivalent widths, with pseudocontinuum bandpasses defined bracketing the feature. An example of our CN index measurement is shown in Figure 4.5.

CO Index Various definitions have previously been put forward for the CO index. As the CO feature lacks a well-defined and easily measurable pseudocontinuum redwards of the feature, index definitions for CO typically define several bandpasses to the blue and extrapolate redwards. The definition of Mármol-Queraltó et al. (2008) defined the pseudocontinuum by two bands blueward of the CO feature. The authors found that this definition was less affected by uncertainties in velocity dispersion, spectral resolution or radial velocity, as well as being less impacted by low S/N, and errors in wavelength or flux calibration. An example of our CO index measurement is shown in Figure 4.6. The two indices are defined in Table 4.2.

Table 4.2: Index Definitions.

Index	Blue Pseudocontinuum (μm)	Central Bandpass (μm)	Red Pseudocontinuum[a] (μm)	Units	Source[b]
CN	1.0445 - 1.0580	1.0780 - 1.1120	1.2160 - 1.2385	Å	1
CO	2.2460 - 2.2550	2.2880 - 2.3010	2.2710 - 2.2770	mag	2

[a]In the case of CO, 'Red Pseudocontinuum' indicates the most redward pseudocontinuum band, which is still blueward of the feature itself. [b]**Sources.** (1) Riffel et al. (2007); (2) Mármol-Queraltó et al. (2008). .

In order to obtain an SSP-equivalent age or metallicity for a population, the strength of an age- or metallicity-sensitive index is measured, and this measurement is compared with the predictions of SPS models. The predicted strength of the 1.1 μm CN index is shown in Figure 4.7. The predictions of the different models are shown as various coloured lines for ages ranging from 1–12 Gyr: M11 is plotted in blue, BC03 in red, and FSPS in green. The

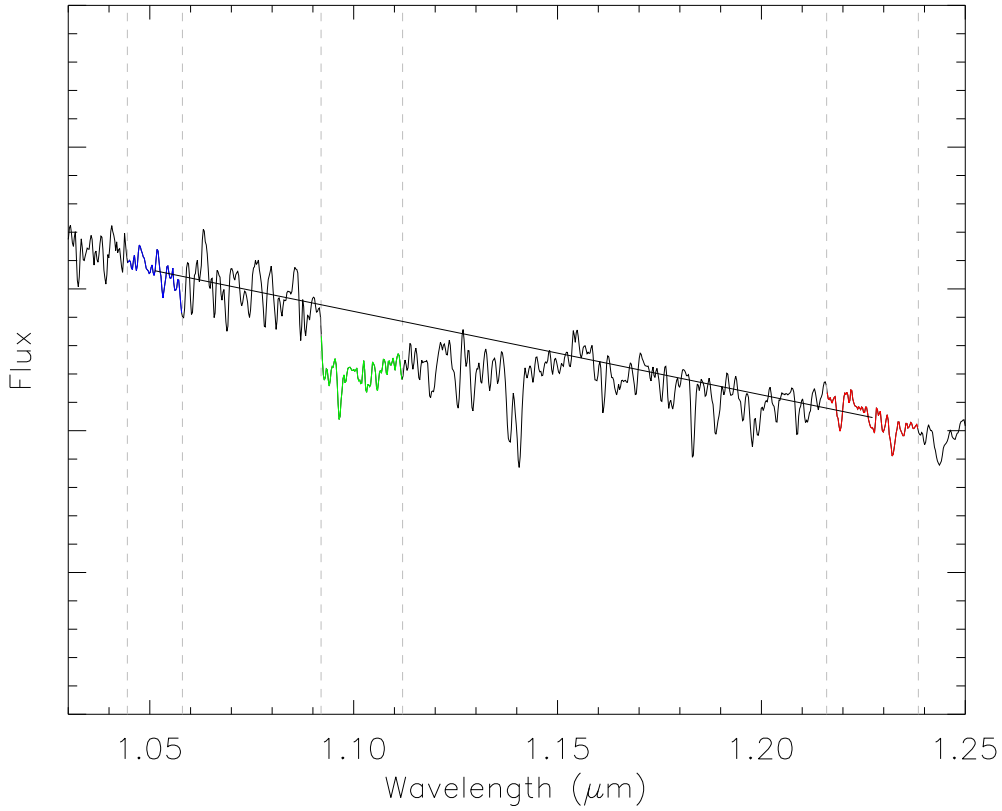

Figure 4.5: Example measurement of the CN index. The spectrum of NGC 3032 is shown, cropped around the feature of interest. The green shows the region of the spectrum falling within the central bandpass. The blue and red show the blue and red pseudocontinuum bandpasses respectively. The average flux in each of the blue and red bandpasses is calculated and joined with a straight line, giving the local pseudocontinuum around the feature. Grey dashed lines mark the edges of the bandpasses for clarity.

M11 models predict a peak in the strength of the CN index ($\sim$ 25Å) for populations of 1 Gyr, after which time the strength quickly decreases to $\sim$ 5Å, displaying no further variation for ages $\geq$ 3 Gyr. The BC03 models exhibit a gradual decline in strength for the CN index, however even at its peak strength CN is only very slightly stronger than the minimum of the M11 predictions. The FSPS models display very different behaviour for the CN index. The strength of the CN index in the FSPS models is predicted to decline from 1 Gyr, becoming negative between ages 2–4 Gyr, and then gradually increasing for ages $>$ 5 Gyr. This is due to the different shape of the FSPS models around the CN feature. A close inspection of the 1 Gyr SSP in Figure 4.1 reveals that the FSPS flux drops slightly before 1.1 μm, as well as at the CN feature itself. This affects the pseudocontinuum calculation, leading to the negative strengths obtained with these models.

Figure 4.8 shows the same thing for the CO index at 2.29 μm. In this case, the M11

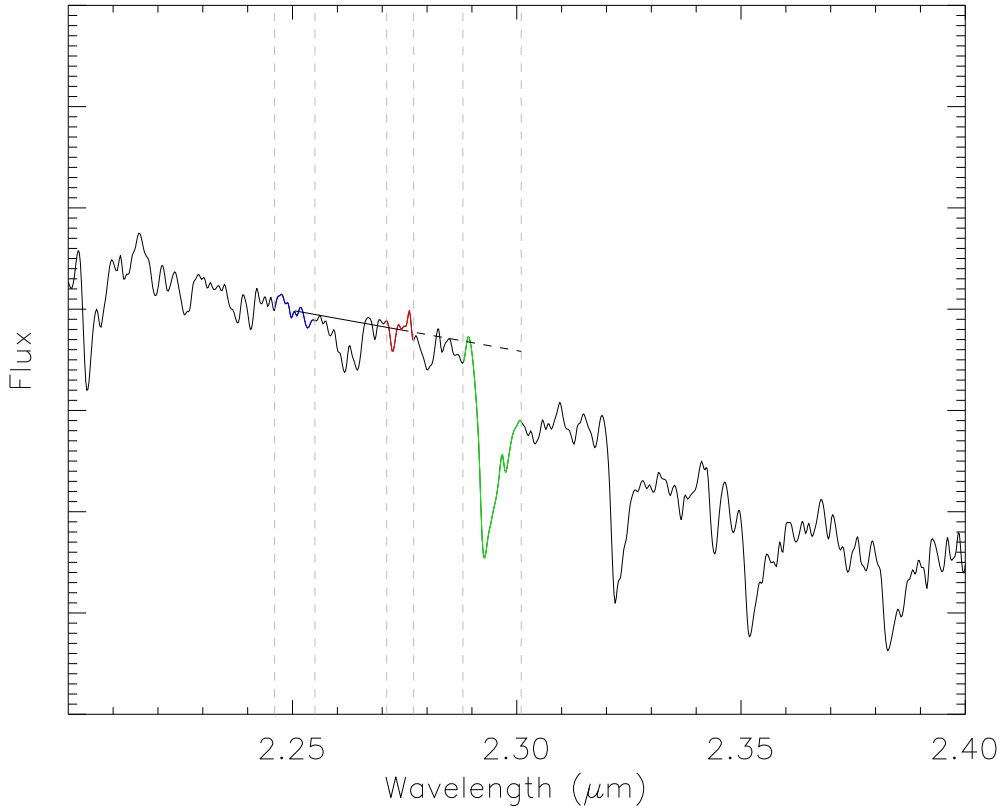

Figure 4.6: Example measurement of the CO index. The spectrum of NGC 3032 is shown, cropped around the feature of interest. The central bandpass is plotted in green and the pseudocontinuum bandpasses plotted in blue and red. The average flux in each of the blue and red bandpasses is calculated and joined with a straight line, which is extrapolated redward to give the local pseudocontinuum around the feature. Dashed lines mark the boundaries of these regions for clarity.

models predict a slightly higher strength for the youngest models, with no change in strength after 3 Gyr. BC03 predict an increase in strength up to 3 Gyr, followed by no change at a similar strength to the M11 models. FSPS predicts CO strength increases to 2 Gyr and then declines. The predicted strength at all ages is much higher than the M11 or BC03 predictions.

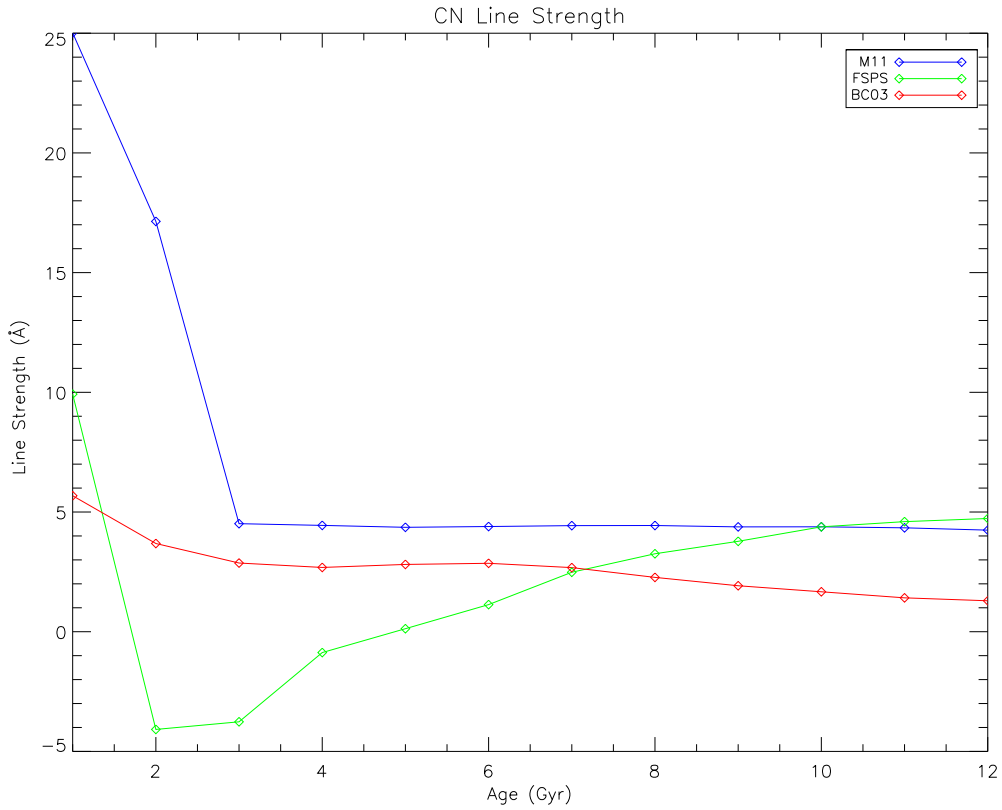

Figure 4.7: Strength of CN Index as predicted by the M11 models (blue), BC03 models (red) and FSPS models (green).

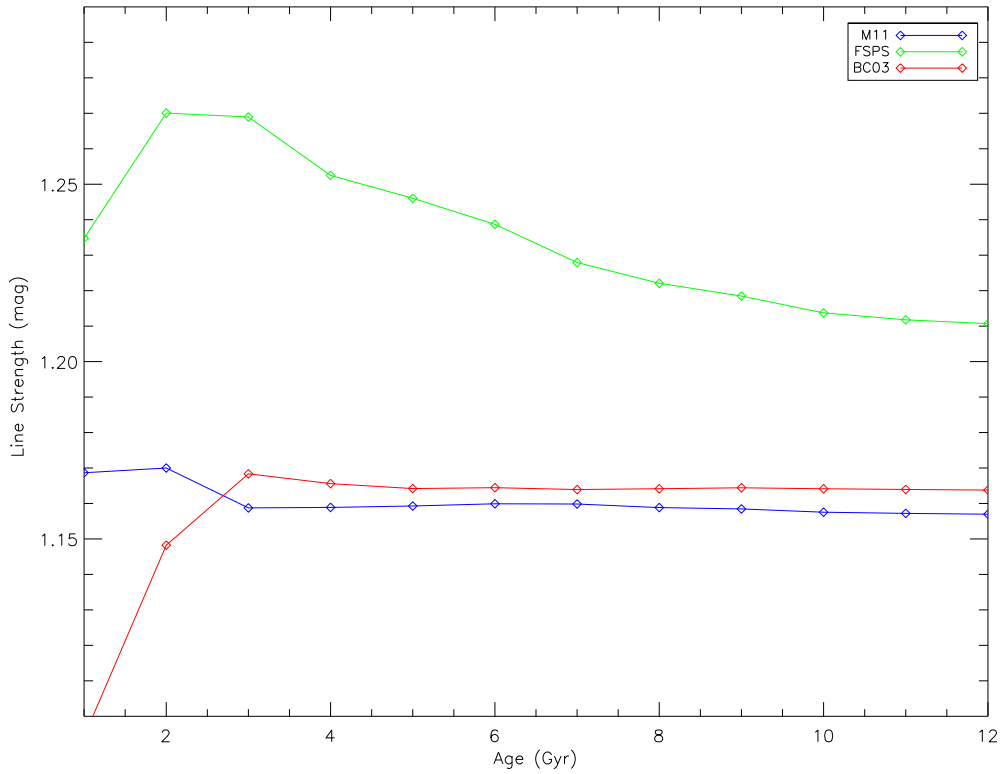

Figure 4.8: Same as Figure 4.7, but for the CO feature.

Chapter 5

Full Spectral Fitting

Spectral fitting is commonly used to derive estimates of the physical properties of unresolved stellar populations (Cid Fernandes et al. 2005; Ocvirk et al. 2006; Koleva et al. 2009; Conroy et al. 2014). With this technique, observations are compared with a grid of synthetic stellar populations spanning a range of ages and metallicities. By finding the template, or combination of templates, which best fit the data, (usually based on a χ^2 figure of merit) estimates can be derived for the age and metallicity of the observed galaxies. To study the stellar populations of our galaxies, we used the penalised pixel fitting code (pPXF)[1] by Cappellari and Emsellem (2004). For a given input spectrum, the code is able to fit individual templates, as well as calculate the best-fitting linear combination of a set of basis templates spanning a grid of age and metallicity. This allows the calculation both of SSP-equivalent ages and metallicities, as well as a star formation history.

5.1 pPXF

pPXF (Cappellari and Emsellem 2004) is a code written primarily to extract the stellar kinematics from absorption-line spectra of galaxies. It does this by fitting template spectra to an input spectrum in pixel space, using a maximum penalised likelihood approach. The fit is done in pixel space to allow the easy masking of gas emission lines or bad pixels from the fit. The first step in the fitting process is the creation of a model galaxy spectrum $G_{\rm mod}(x)$. A galaxy spectrum can be considered to be the sum of a number of stellar spectra redshifted according to their line-of-sight velocities. The model spectrum is thus the convolution of a template spectrum $T(x)$ with a parametrised line-of-sight velocity distribution (LOSVD), so

[1] http://www-astro.physics.ox.ac.uk/∼mxc/software/

that

$$G_{\rm mod}(x) = \sum_{k=1}^{K} w_k [B * T_k](x) + \sum_{l=0}^{L} b_l P_l(x) \qquad \text{for } w_k \geq 0 \tag{5.1.1}$$

where T_k is a library of k galaxy templates, $B(x)$ is the broadening function (represented by a parametrized function representing the LOSVD), and w_k are the positive weights applied to each template. $P_l(x)$ are Legendre polynomials of order l, added to account for differences in shape between the galaxy and the templates, and b are the positive weights attributed to the polynomials. Multiplicative polynomials can be included to serve the same purpose, which have the advantage that the relative strengths of the template absorption lines are not altered. We therefore use multiplicative polynomials in this analysis.

For each trial LOSVD, the best linear combination of templates is found by applying the bounded-variables linear least-squares algorithm of Lawson and Hanson (1995), which gives the set of non-negative template weights. The goodness of fit for this $G_{\rm mod}$ is then evaluated via the χ^2 value, defined as:

$$\chi^2 = \sum_{n=1}^{N} r_n^2 \tag{5.1.2}$$

where the residuals r_n are defined as:

$$r_n = \frac{G_{\rm mod}(x_n) - G(x_n)}{\Delta G(x_n)} \tag{5.1.3}$$

and $\Delta G(x_n)$ is the measurement error spectrum.

If a set of SSP model spectra of different ages are used as templates, these weights can be interpreted as a star formation history (SFH), giving the contribution of stars formed at a given epoch. pPXF can also be run on individual model spectra, and the resulting χ^2 values used to determine which single template best represents the observed spectrum.

5.2 Preparatory Steps

For each model, the first step was to read in the 12 SSP templates, prepared as detailed in Section 4.2: truncated to the relevant wavelength range and resampled onto pixels of constant linear wavelength, in order to mimic the GNIRS observations. The observations were also smoothed to the resolution of the models. The GNIRS spectrograph has a higher resolution (9 Å FWHM) than all three sets of models, requiring the resolution of the data to be degraded in order to compare measurements with model predictions. Both the M11 and BC03 models use the Pickles library, which has a resolution of 32 Å (FWHM). The Conroy models use the BaSeL library, which has a lower resolution of 53 Å (FWHM). To account

for differences in resolution between spectra, we convolve them using a Gaussian of FWHM given by:

$$\mathrm{FWHM_{Gaussian}} = \sqrt{(\mathrm{FWHM^2_{Max}} - \mathrm{FWHM^2_{Spec}})} \tag{5.2.1}$$

The observed galaxy spectrum and the models were then rebinned to a log scale so as to have a constant velocity step. This is necessary since:

$$\Delta v = \frac{c\Delta\lambda}{\lambda} \tag{5.2.2}$$

Integrating gives:

$$v = c\ln(\lambda) \tag{5.2.3}$$

so velocity is proportional to $\ln(\lambda)$, not linear λ.

Regions of poor atmospheric transmission (as defined in Section 2.4) between the J & H, and H & K bands were masked. These were removed to restrict the analysis to areas with high S/N – usually $\gtrsim 100$, although in two galaxies (IC 0719 and NGC 5475) the spectra include small regions where the S/N< 50.

pPXF is primarily designed to measure stellar kinematic parameters, such as mean velocity, velocity dispersion, and higher-order moments of the LOSVD. To get the correct LOSVD requires having the most accurate template possible, which often involves combining multiple templates in an optimal way. However, this thesis is concerned with comparing the galaxy spectra with the SSP templates in order to infer their stellar population properties. In particular, we wish to explore which models are the best representation of the galaxy spectra. For this reason, when applying pPXF, we first fit the spectrum using all templates simultaneously for a given family of models, and include a high order polynomial continuum term, thus obtaining the best numerical fit possible and securing the correct velocity and velocity dispersion values. These two parameters are then fixed in the subsequent fits. This reduces the freedom pPXF has to compensate the template choice with varying kinematic parameters.

For subsequent fits, we included a multiplicative polynomial of order 1 to account for low-order errors in flux calibration, without affecting the relative strength of absorption lines. This required the models to match the data by their own merits, without relying on the polynomial to match the observed shape.

5.2.1 Calibration of the Error Spectrum

The figure of merit used to calculate the best-fit spectrum depends on the measurement errors in the spectrum $\Delta G(x_n)$ as seen in Equations (5.1.2) and (5.1.3) A good estimate of

the error is therefore necessary to obtain a meaningful value of χ^2. Accurately propagating the error spectrum through all steps of the reduction, including accounting for the covariance between pixels, is not fully implemented in the IRAF software. We therefore opted to derive an empirical estimate of the error spectrum. This was done for each galaxy by performing a spectral fit using all available templates, plus a high order polynomial, to enable the fitting of all intrinsic galaxy features. The error was then taken to be the difference between this optimal template and the galaxy spectrum. For each galaxy, this same error vector was used to calculate a χ^2 for every spectral fit, allowing the quality of fit of the different models to be assessed using the absolute values of the resulting χ^2.

5.3 Results

5.3.1 Single Stellar Populations

We initially treated each galaxy as a single stellar population. For every galaxy we individually fit templates spanning the range 1–12 Gyr in 1 Gyr steps. The results of the fits are shown in Figures 5.1 to 5.12. Each plot shows the best-fit SSP for each of the three models, as determined by the reduced χ^2 value ($\chi^2_{\rm red}$). The best-fitting template ages and $\chi^2_{\rm red}$ values are given in Table 5.1.

Fit quality

Table 5.1 shows that all models yield poor $\chi^2_{\rm red}$ values from SSP fitting ($\chi^2_{\rm red} \gg 1$). However the BC03 models give consistently lower $\chi^2_{\rm red}$ values for every galaxy, with the notable exception of NGC 4710. The $\chi^2_{\rm red}$ value calculated using BC03 is on average, approximately a factor of 2 better than that calculated with M11 or FSPS. These two models obtain similar values, with FSPS being slightly the worst of the three (with an average $\chi^2_{\rm red} = 7.08$ as opposed to $\chi^2_{\rm avg} = 6.35$ for M11 and $\chi^2_{\rm avg} = 2.64$ for BC03).

The χ^2 results are mostly driven by overall spectral shape, as opposed to the strengths of specific features. The low order polynomial included in the fit makes apparent the flaws in the overall shapes of the templates, which are particularly noticeable in the FSPS models. These deficiencies in the models would be hidden by a high-order polynomial. With regards to spectral shape, FSPS templates are too rounded compared to the data, with prominent bulges present throughout the NIR range. This leads to a noticeable deviation from the galaxy data when fitting. As none of the FSPS models provide a particularly good fit, the $\chi^2_{\rm red}$ values do not strongly exclude any templates, as seen in the plot insets. Generally, the M11 models are better able to match the overall shape with their old templates. Young

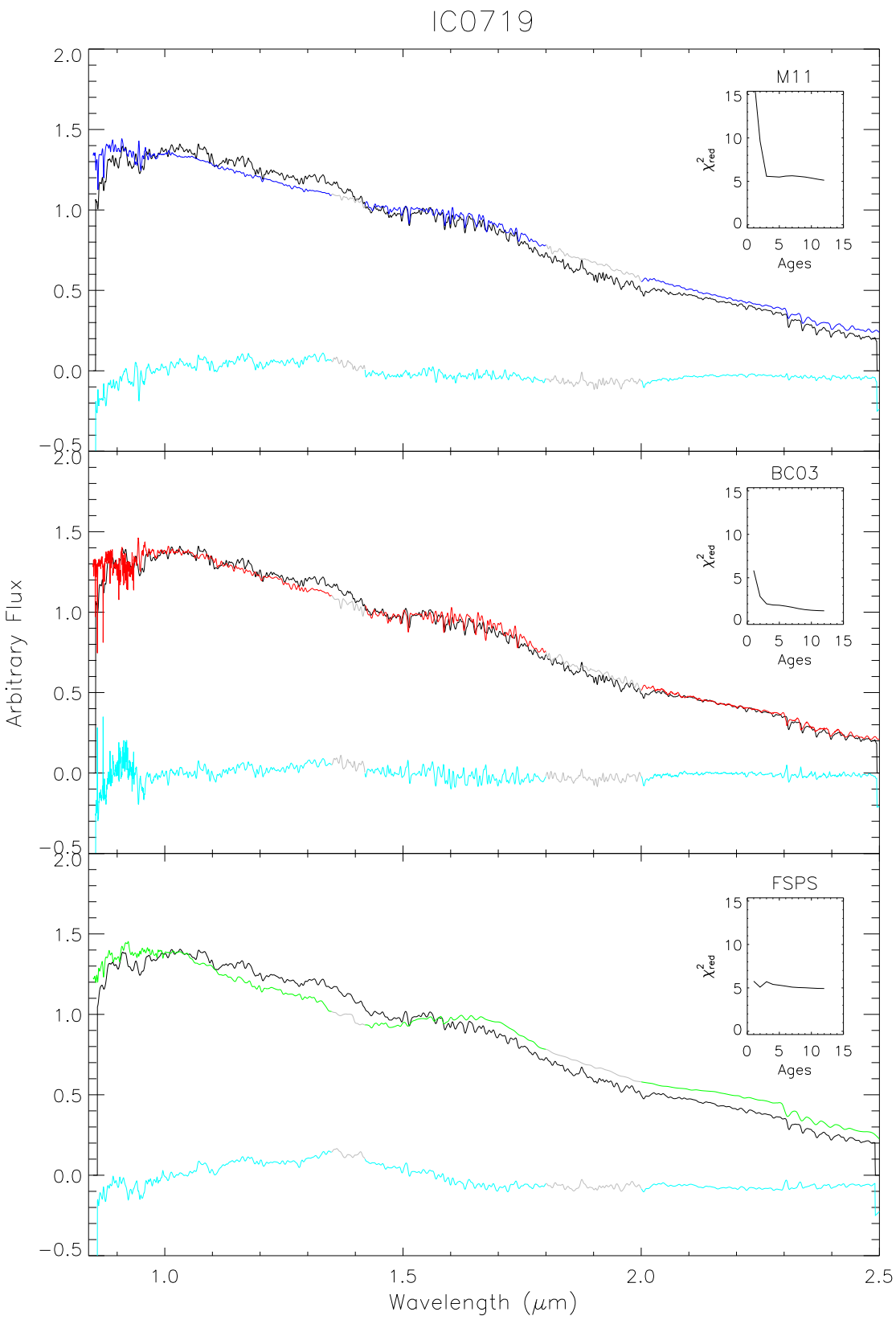

Figure 5.1: SSP fits for IC0719 for the three SPS models. The top panel shows the best-fit SSP obtained with the M11 models, the middle shows BC03, and the bottom panel FSPS. The observed spectrum is plotted in black, the best-fit in blue, red or green for M11, BC03 and FSPS respectively, and the residuals for each are shown in the bottom of each plot in cyan. The masked regions are plotted in grey. The inset shows the reduced χ^2 plotted against age for each galaxy. The age of the best-fit SSP is given in Table 5.1.

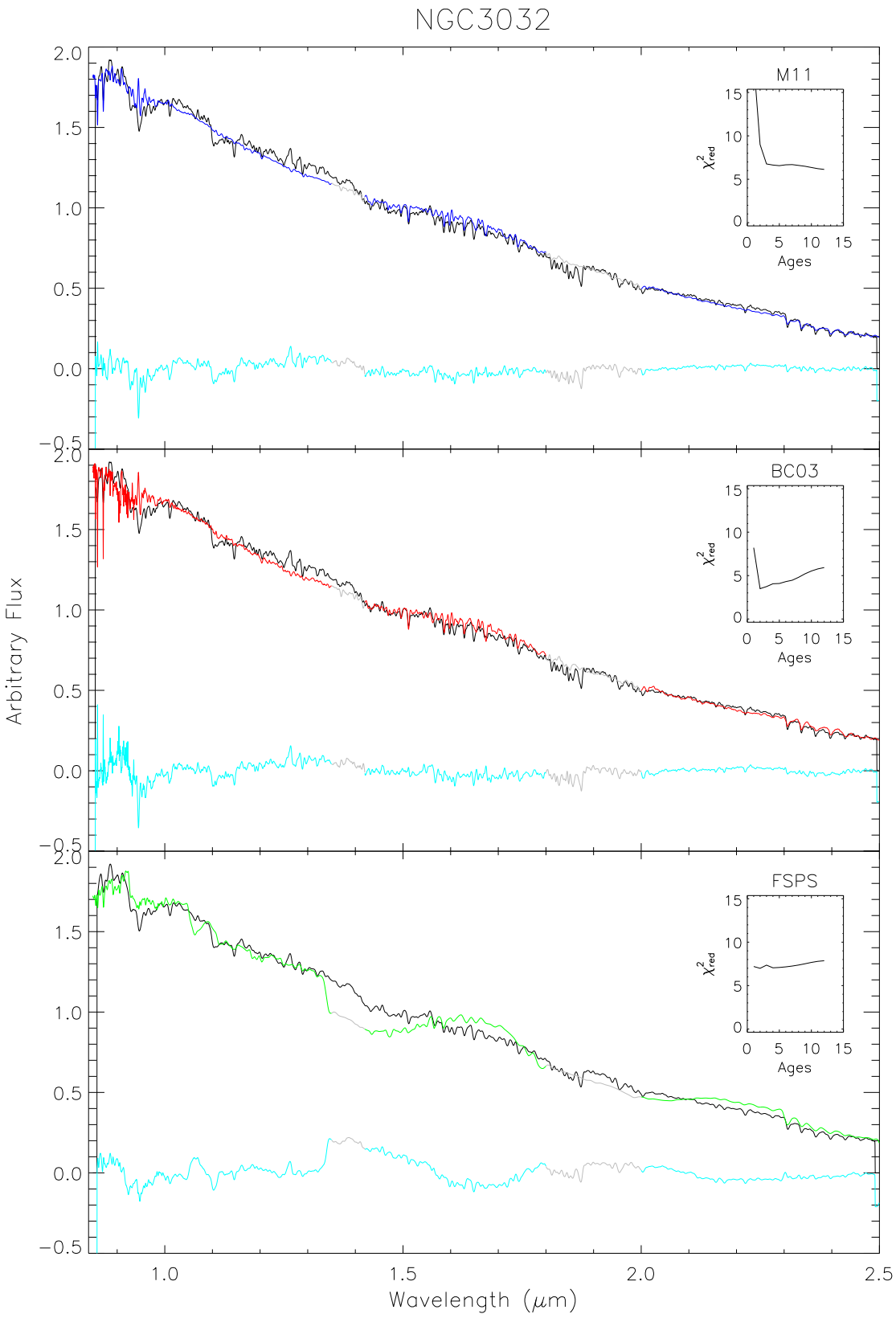

Figure 5.2: As in Figure 5.1 but for NGC3032

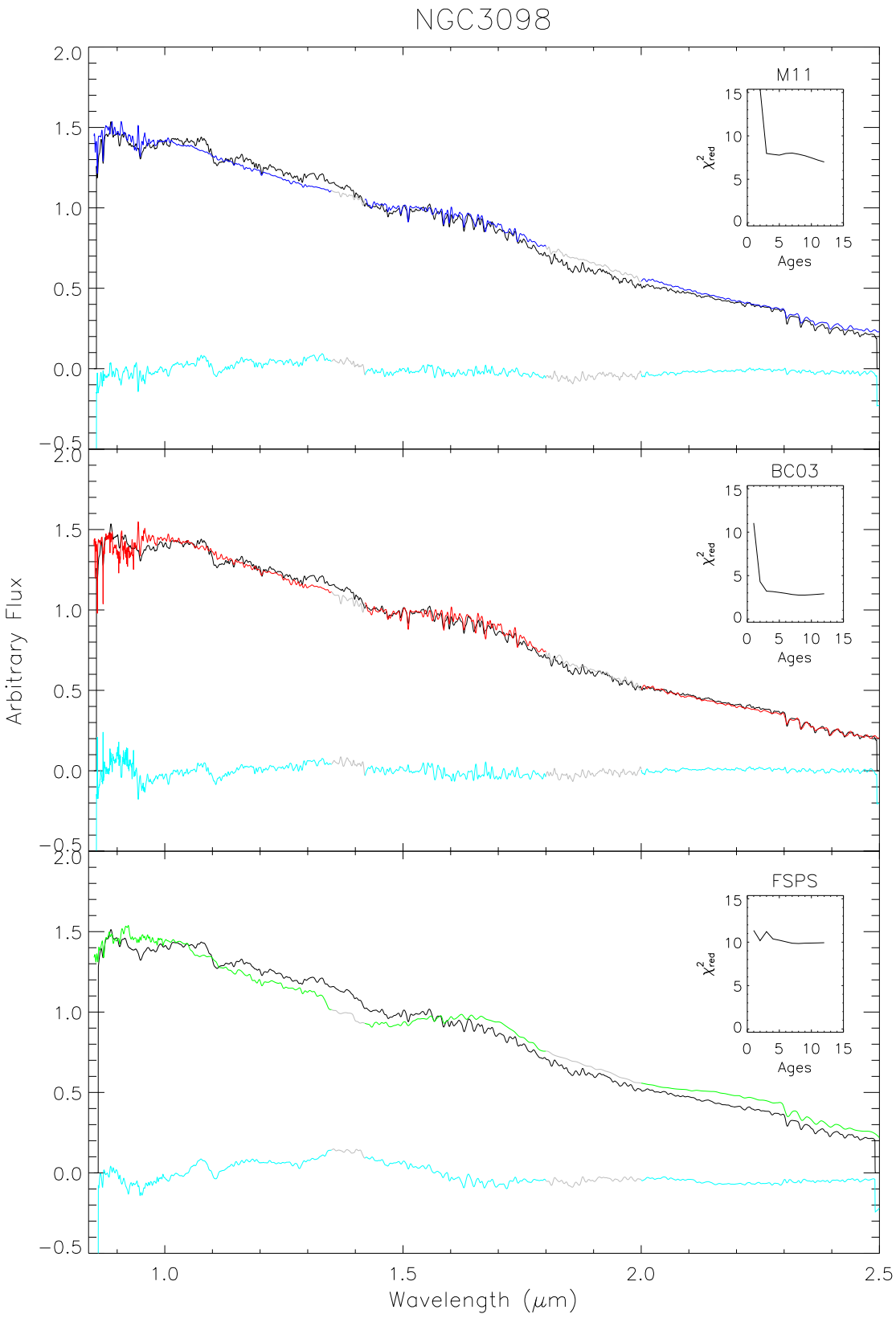

Figure 5.3: As in Figure 5.1 but for NGC3098

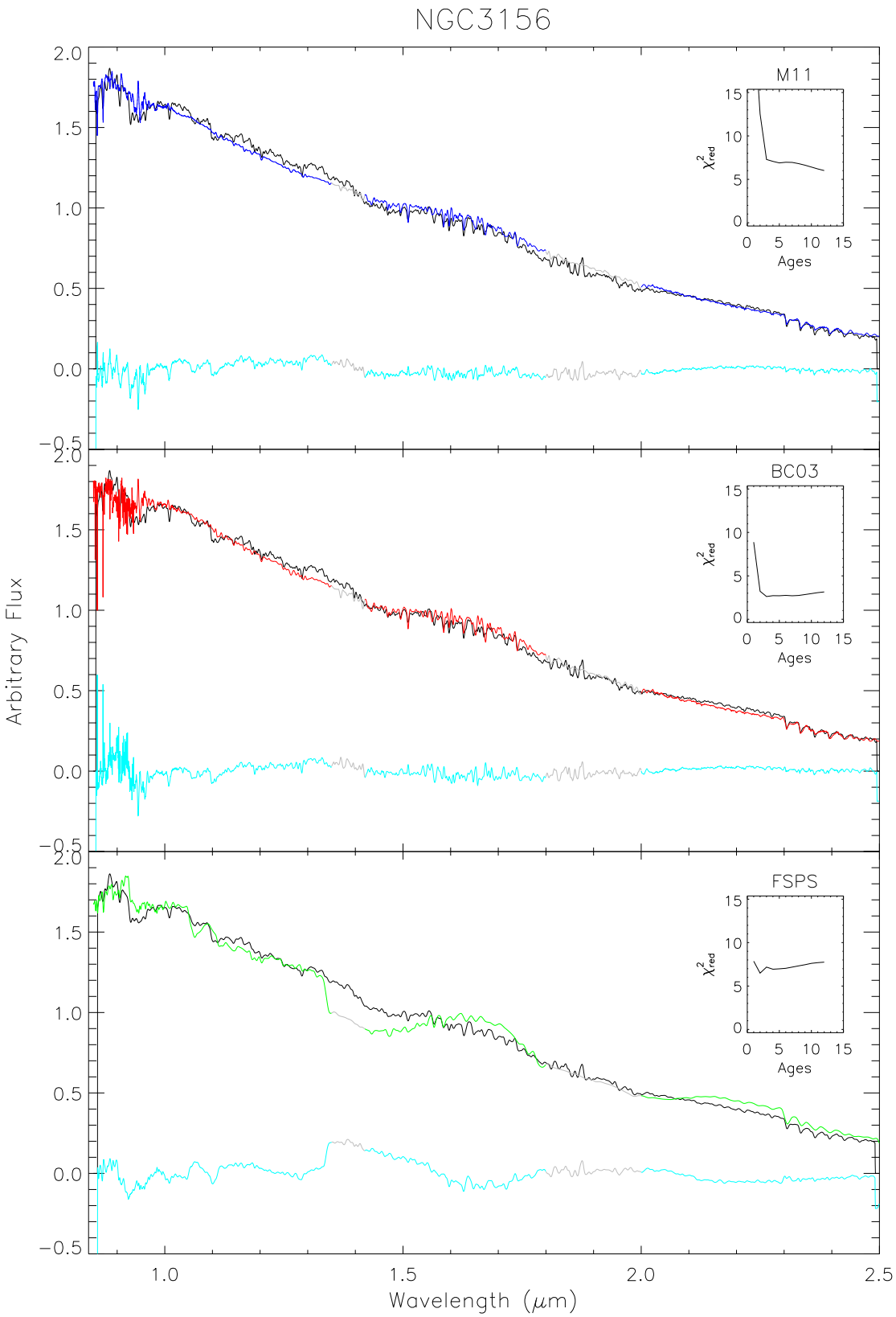

Figure 5.4: As in Figure 5.1 but for NGC3156

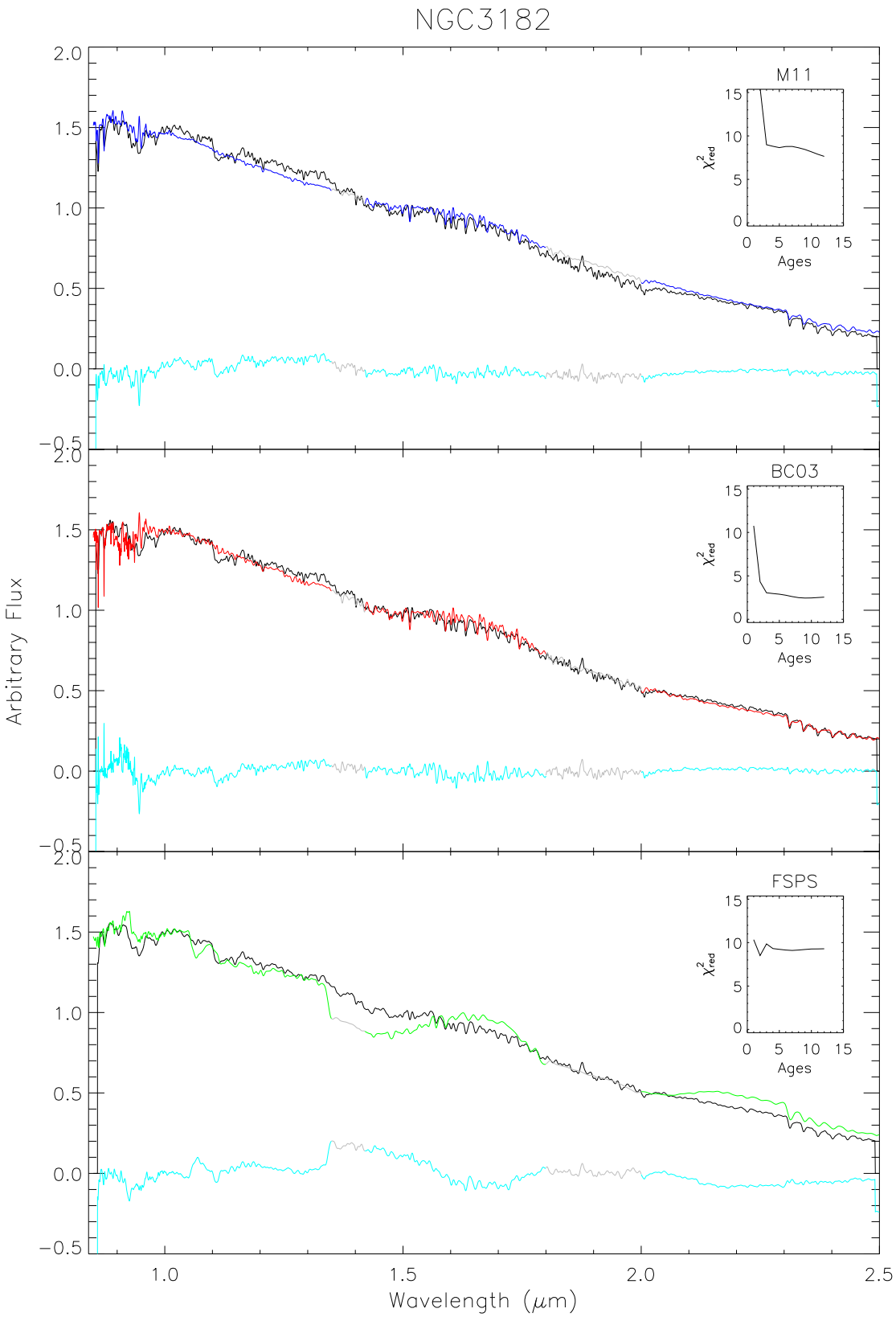

Figure 5.5: As in Figure 5.1 but for NGC3182

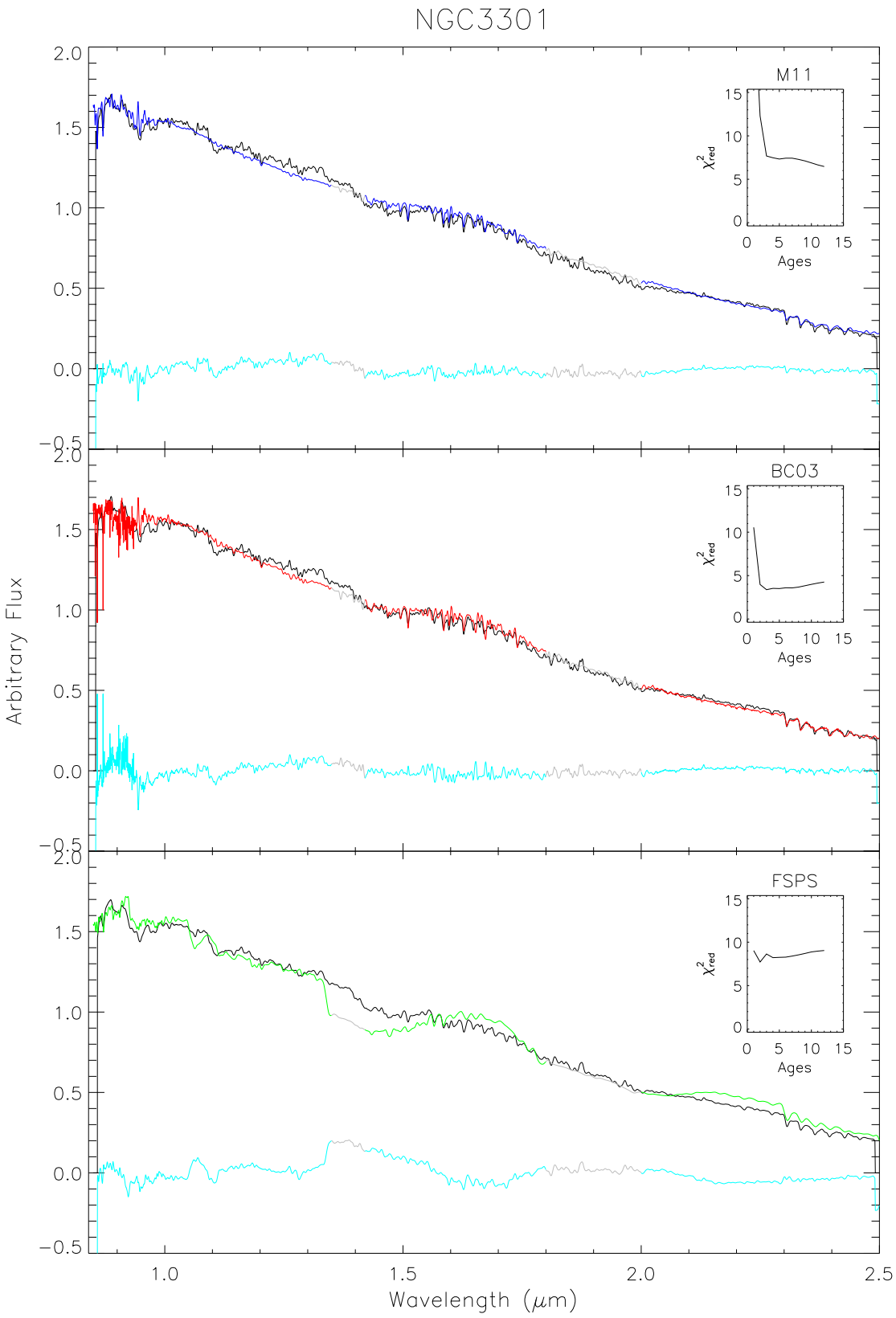

Figure 5.6: As in Figure 5.1 but for NGC3301

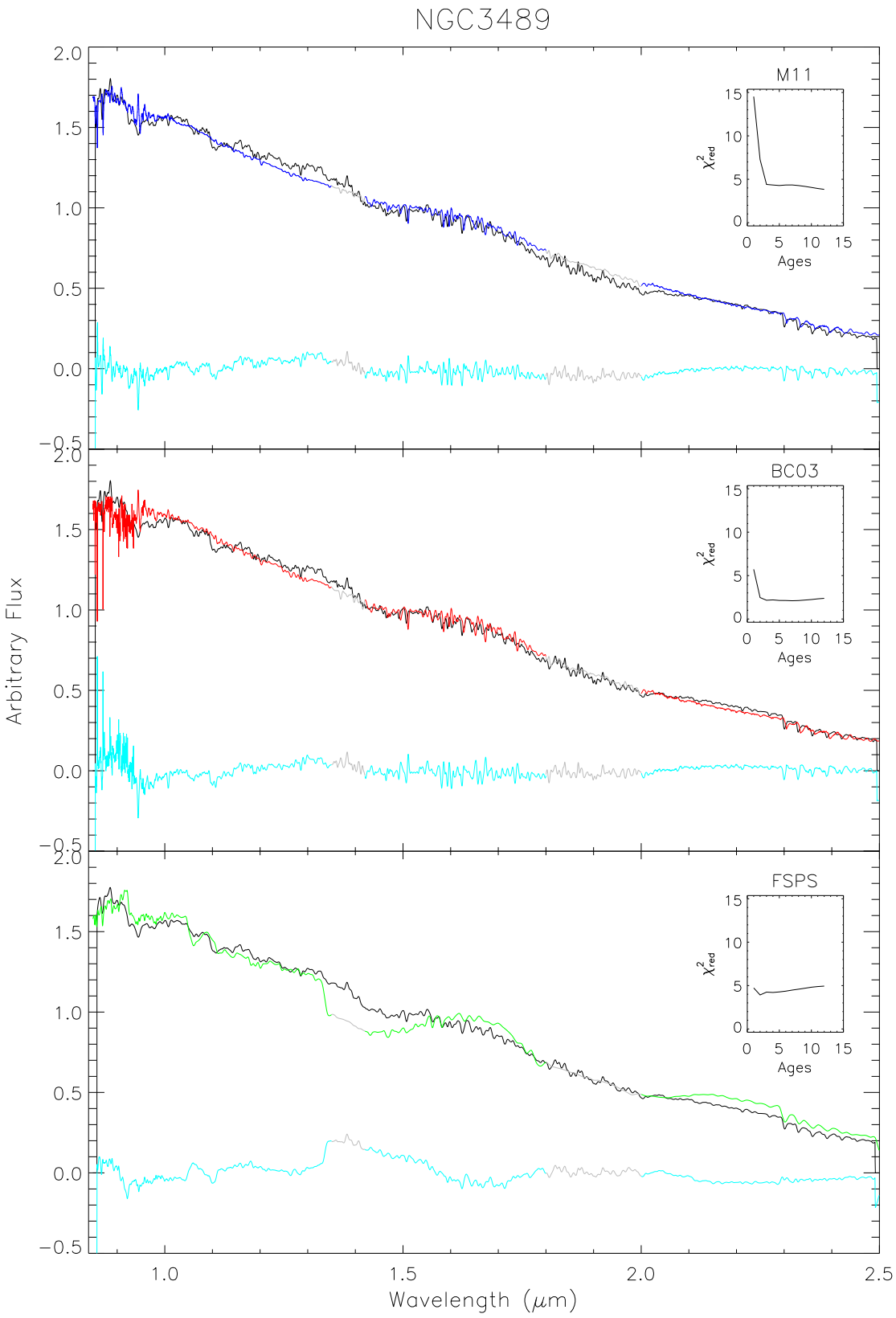

Figure 5.7: As in Figure 5.1 but for NGC3489

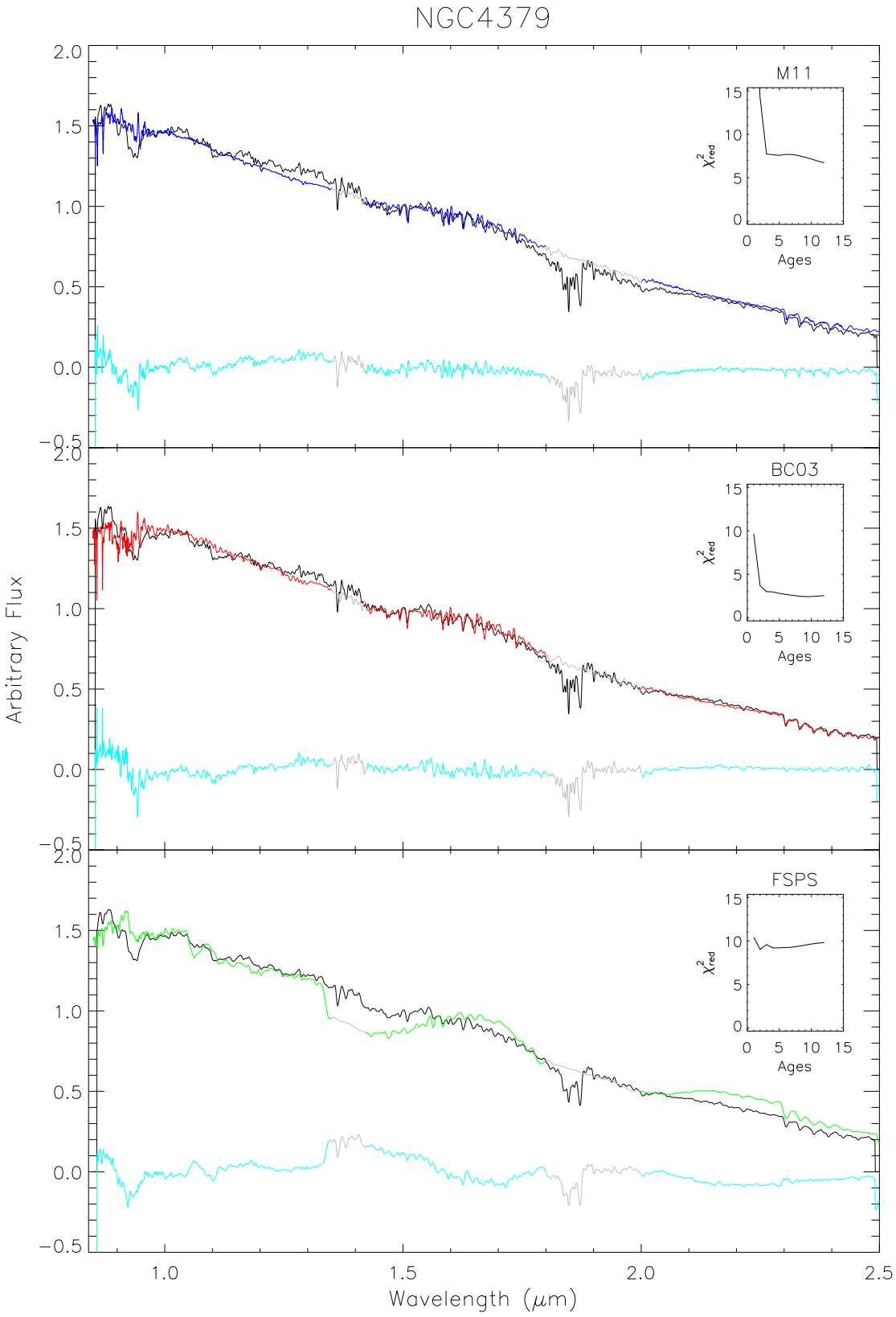

Figure 5.8: As in Figure 5.1 but for NGC4379

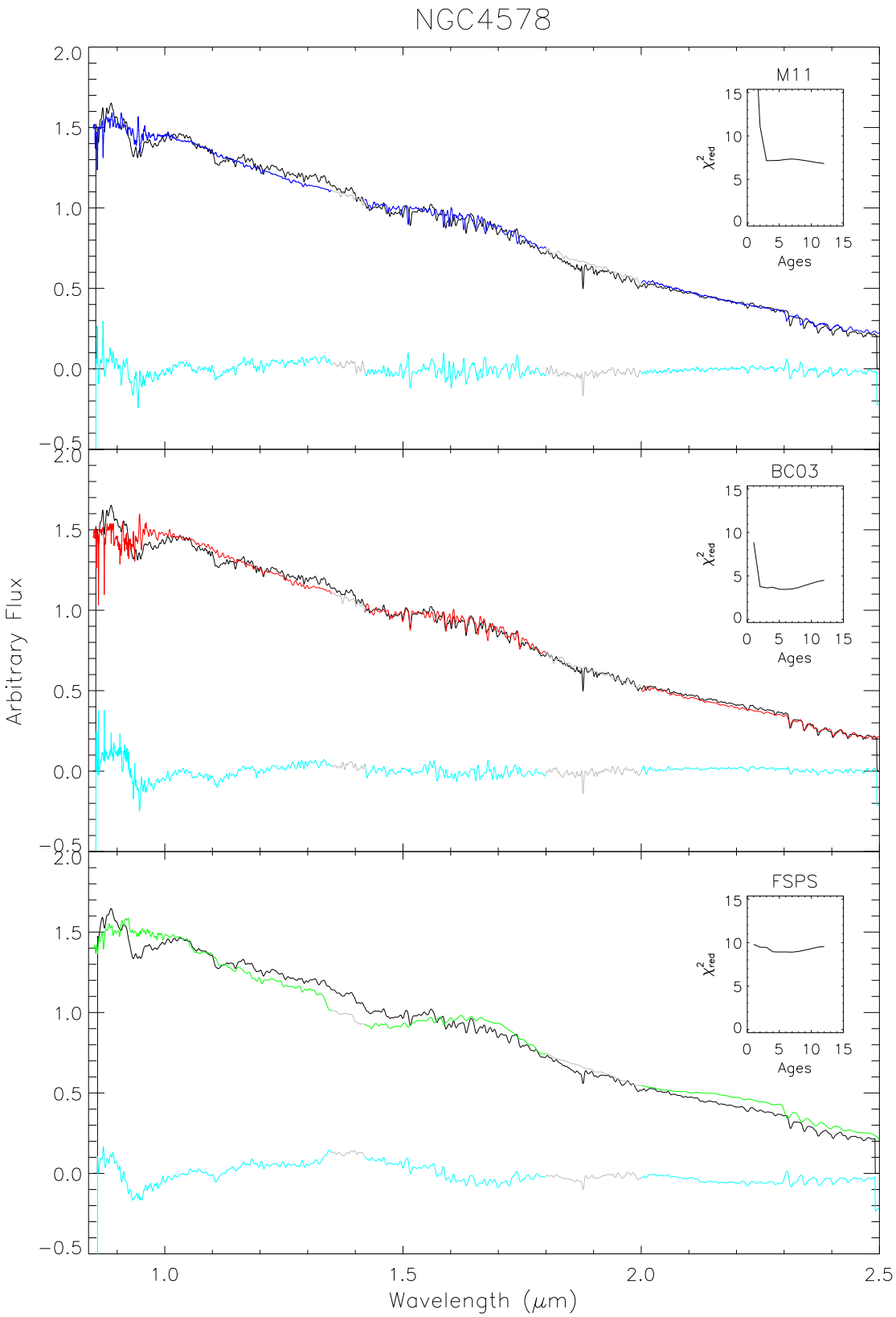

Figure 5.9: As in Figure 5.1 but for NGC4578

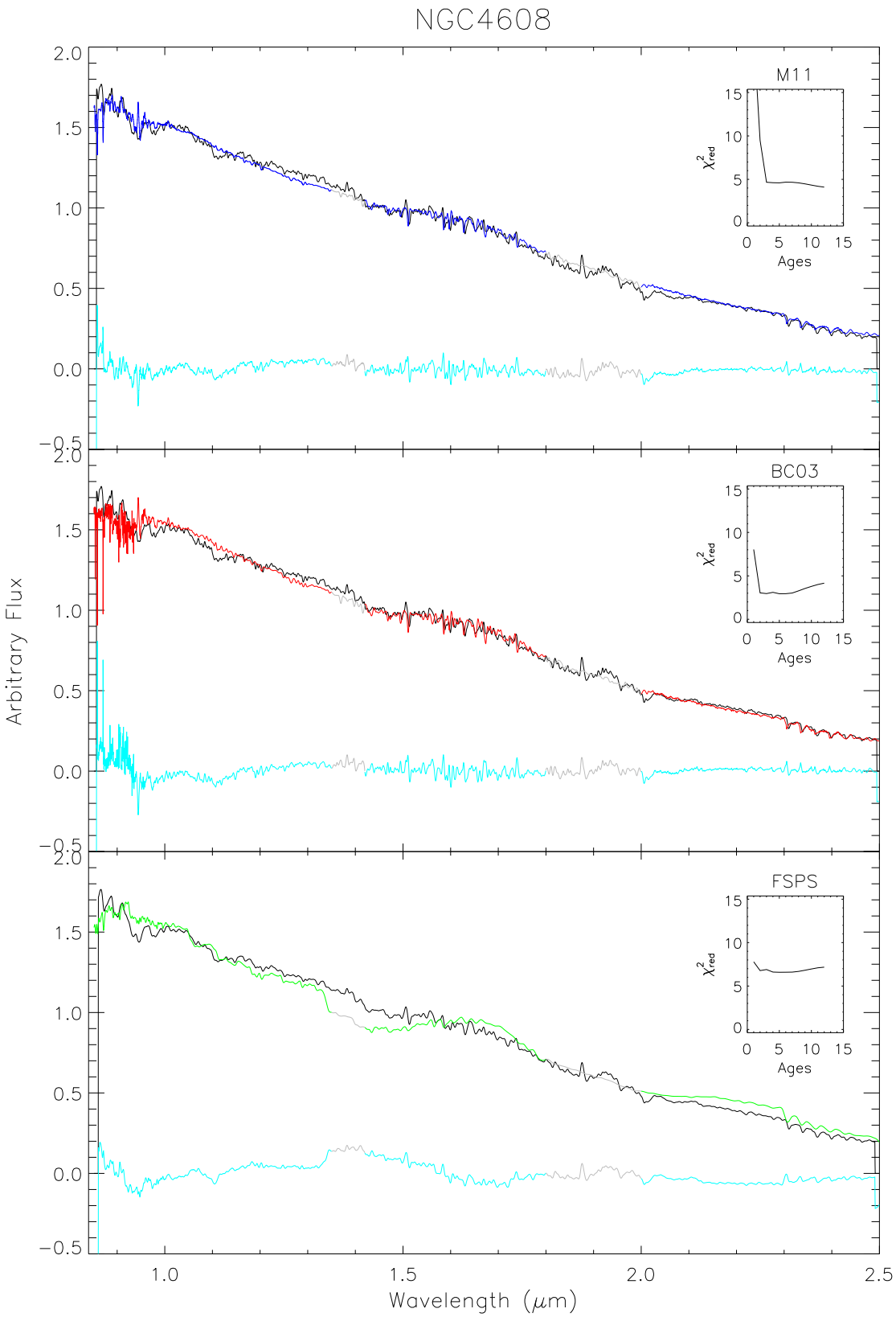

Figure 5.10: As in Figure 5.1 but for NGC4608

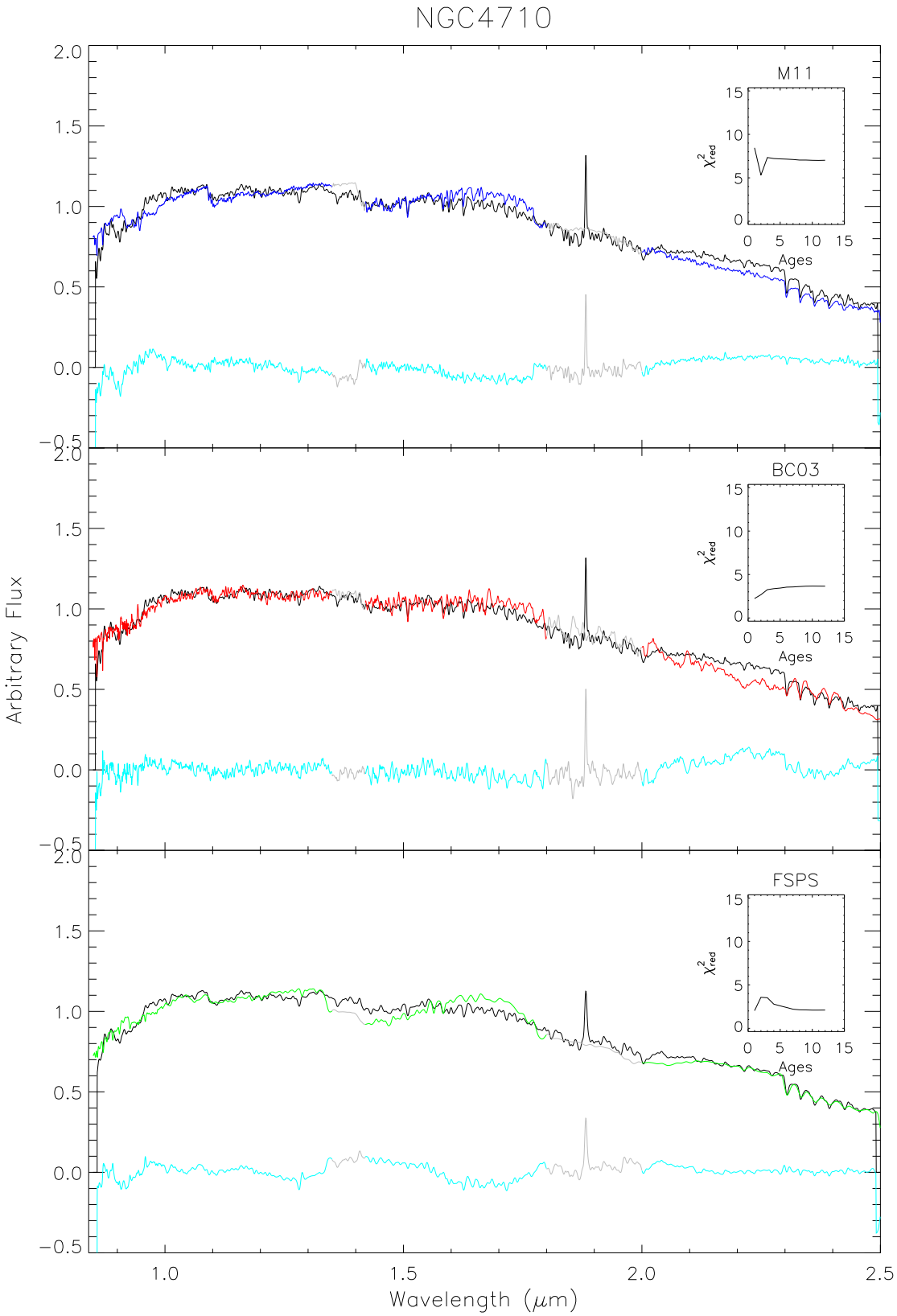

Figure 5.11: As in Figure 5.1 but for NGC4710

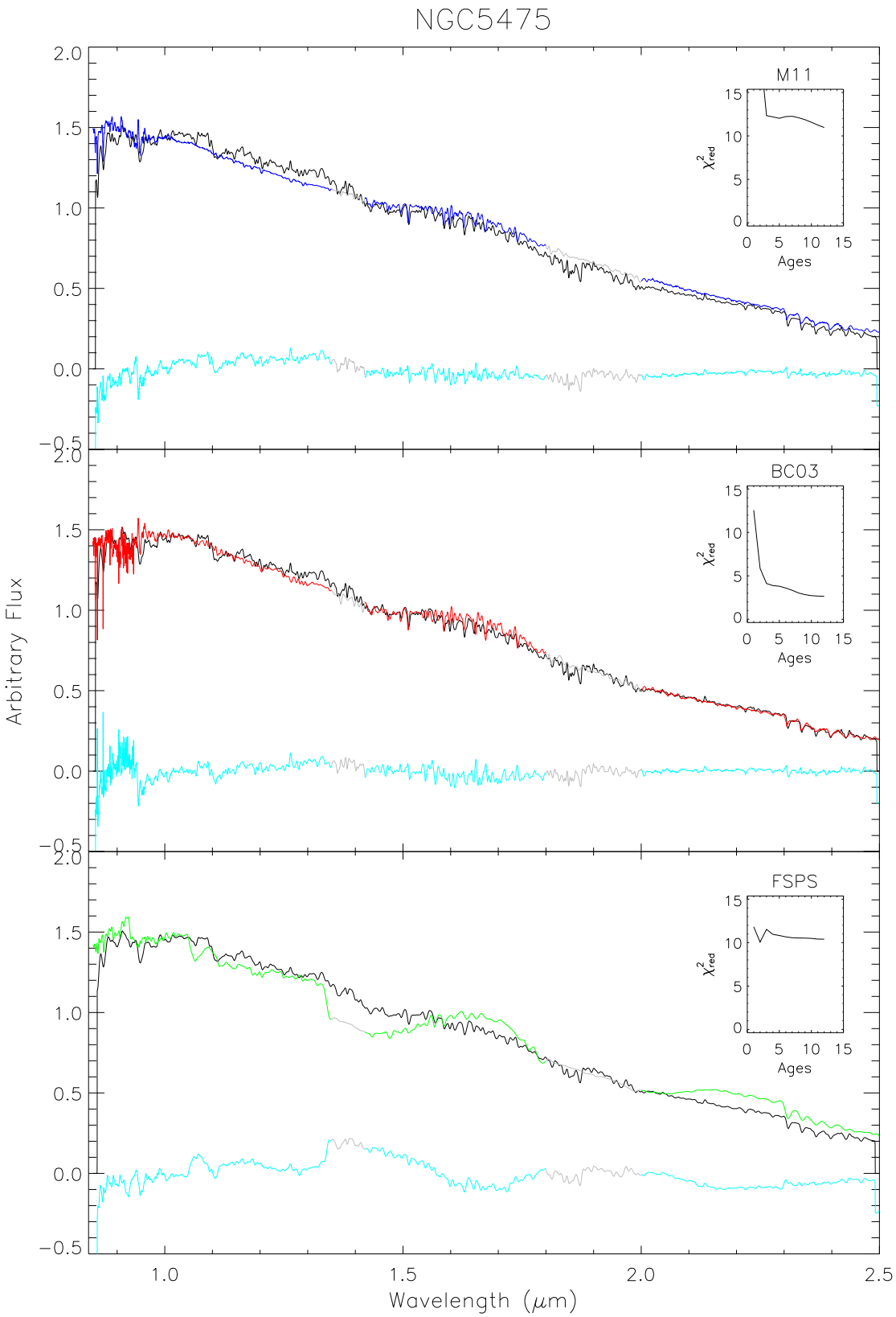

Figure 5.12: As in Figure 5.1 but for NGC5475

templates drastically overpredict the depth of the sharp TP-AGB features and the very flat continuum shape, leading to the exclusion of young templates based on the $\chi^2_{\rm red}$ value. Old models ($\gtrsim$ 3 Gyr) have been seen already to display little variation, and thus have little difference in the $\chi^2_{\rm red}$ value. The BC03 models display similar behaviour, typically excluding the youngest templates based on the $\chi^2_{\rm red}$ value. The one exception here is NGC 4710, for which the $\chi^2_{\rm red}$ does not strongly exclude any templates for any model.

Comparison with ATLAS$^{\rm 3D}$ Age Estimates

Here we compare the age estimates obtained by each model to the values calculated by ATLAS$^{\rm 3D}$. This is shown in Figure 5.13, where the models are plotted as different coloured symbols. The error in our ages derived from the infrared model fits is estimated as $\pm$2 Gyr, but this is purely for illustrative purposes. All the spectral fits have $\chi^2_{\rm red}$ well in excess of unity, implying an intrinsically poor fit of the models to the data, and making a meaningful statistical error estimate unfeasible. A single illustrative error bar is shown in the top right corner of the plot.

There is poor correspondence between age estimates derived from the three models, as well as with the age estimates derived from the optical by ATLAS$^{\rm 3D}$. Visual inspection suggests that the different models have some promising features at particular wavelengths, but none do a good job at reproducing the full spectral range. The poor match to the full spectral range drives the $\chi^2_{\rm red}$ of the fit, thus diluting the influence of specific features on the overall quality of fit.

5.3.2 Star Formation History

So far we have considered only SSPs, however this is an oversimplification for galaxies. We next consider the effect of a composite stellar population on the fits, as the SSP analysis demonstrated that particular features, such as CN, are significantly stronger than expected in models of specific ages. pPXF allows the derivation of a star formation history (SFH) by fitting multiple templates of different ages and metallicities simultaneously to observations. This could have been done using our near-infrared templates. However, the optical region is more robust against SPS uncertainties than the near-infrared (Conroy et al. 2010). For this reason, we utilised the SFH generated from the optical spectra by McDermid et al. (2014). The authors performed a regularised linear fit (Press et al. 1992) to the galaxies' optical spectra using SSP templates sampling a grid of age and metallicity. They obtained mass-weighted values of these parameters for every galaxy in the sample. The mass weights were binned to 1 Gyr time steps spanning the same range as the templates we are using in

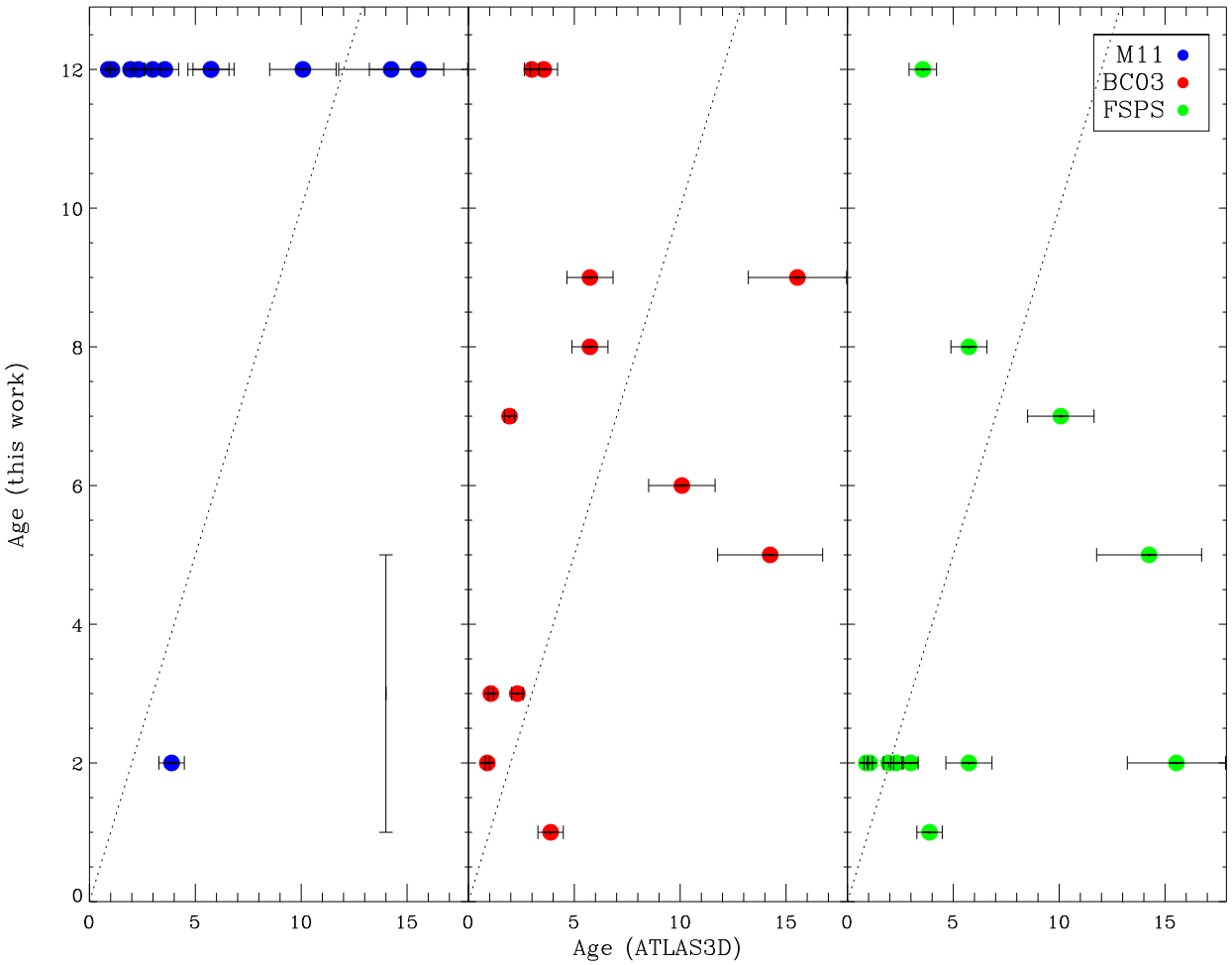

Figure 5.13: SSP-equivalent ages for each model compared with those calculated by ATLAS^{3D}. The M11 SSP-ages are plotted with blue circles, BC03 SSP-ages with red triangles and FSPS SSP-ages with green squares. The vertical error bar in the top left corner indicates an estimated error of ± 2 Gyr for the infrared age estimates. The 1:1 relation is shown as a dotted line.

the fits. As our sample was selected from the ATLAS^{3D} parent sample to be approximately solar, we marginalised over metallicity.

We thus created three SED templates for each galaxy (one for each model we set out to test) based on that galaxy's SFH. For each model, we multiplied every age template by its appropriate mass fraction, and added these templates together to create a single template for each model. This template was then fit to the galaxy in the same way as the SSP templates, and a $\chi^2_{\rm red}$ was calculated for each model. The mass fractions for each galaxy are shown in Figure 5.14. The results of the fits are shown in Figures 5.15 to 5.25 and given in Table 5.1.

Taking into account the effect of multiple populations demonstrates a few things: The inclusion of the SFH alleviates the problem of the M11 models predicting too strong a con-

Table 5.1: Spectral Fits.

		Single Stellar Populations						Star Formation History		
	ATLAS^{3D}	M11		BC03		FSPS		M11	BC03	FSPS
Galaxy	Age	Age	$\chi^2_{\rm red}$	Age	$\chi^2_{\rm red}$	Age	$\chi^2_{\rm red}$	$\chi^2_{\rm red}$	$\chi^2_{\rm red}$	$\chi^2_{\rm red}$
NGC3032	0.89	12	6.14	2	3.49	2	6.98	5.66	7.31	14.08
NGC3156	1.06	12	6.01	3	2.62	2	6.48	7.65	5.14	13.17
NGC3489	1.94	12	3.84	7	2.10	2	3.92	4.27	4.21	8.52
NGC3301	2.31	12	6.47	3	3.37	2	7.71	7.30	7.18	16.77
NGC5475	2.99	12	10.97	12	2.64	2	10.06	11.41	5.79	20.90
IC0719	3.56	12	5.12	12	1.20	12	4.93	5.58	2.68	9.98
NGC4710	3.88	2	5.31	1	2.24	1	2.03	7.12	7.11	4.43
NGC3098	5.74	12	6.99	8	2.75	8	9.84	7.45	5.57	19.77
NGC3182	5.74	12	7.65	9	2.44	2	8.51	8.20	4.97	18.32
NGC4578	10.08	12	6.83	6	3.45	7	8.90	5.27	8.53	18.83
NGC4608	14.25	12	4.10	5	2.94	5	6.59	3.53	8.31	14.35
NGC4379	15.54	12	6.73	9	2.42	2	9.04	6.23	5.06	19.62

Notes. ATLAS^{3D}Age gives the SSP-equivalent age calculated from optical line-strength indices. The single stellar populations columns give the age of the best-fit template based on the reduced χ^2, as well as the value of $\chi^2_{\rm red}$. Star formation history results are based on the fitting of a single composite template generated from the star formation history derived by ATLAS^{3D}, and thus give only the $\chi^2_{\rm red}$ for this template. All ages are given in Gyr.

tribution from the TP-AGB phase for intermediate age populations. These models can now match the CN break observed in NGC 3032 and NGC 3156, which are the galaxies with the largest mass-fraction of intermediate age populations. This indicates that the weaker than expected CN strength measured in the youngest galaxies is consistent with dilution by old populations present within the galaxy.

In most cases however, the physically-motivated SFH template was not a better fit to the data than the best-fitting SSP template, in spite of the fact that it should better represent the stellar populations present in the galaxies. In the case of the M11 models, a number of the $\chi^2_{\rm red}$ values did improve, although only marginally. Overall, the $\chi^2_{\rm red}$ value calculated for the SFH using the models of M11 stayed approximately the same. However, the $\chi^2_{\rm red}$ values obtained using BC03 and FSPS were, on average, double the values obtained from SSP fitting. This indicates that the SSP fits are driven by numerical and systematic effects rather than physical effects, since we know the SFH template should be a better representation of the composite stellar populations in our sample galaxies.

Overall, the $\chi^2_{\rm red}$ values obtained in both scenarios were $\gg 1$, demonstrating that fundamental inaccuracies are present in all models. No model was able to easily reproduce the

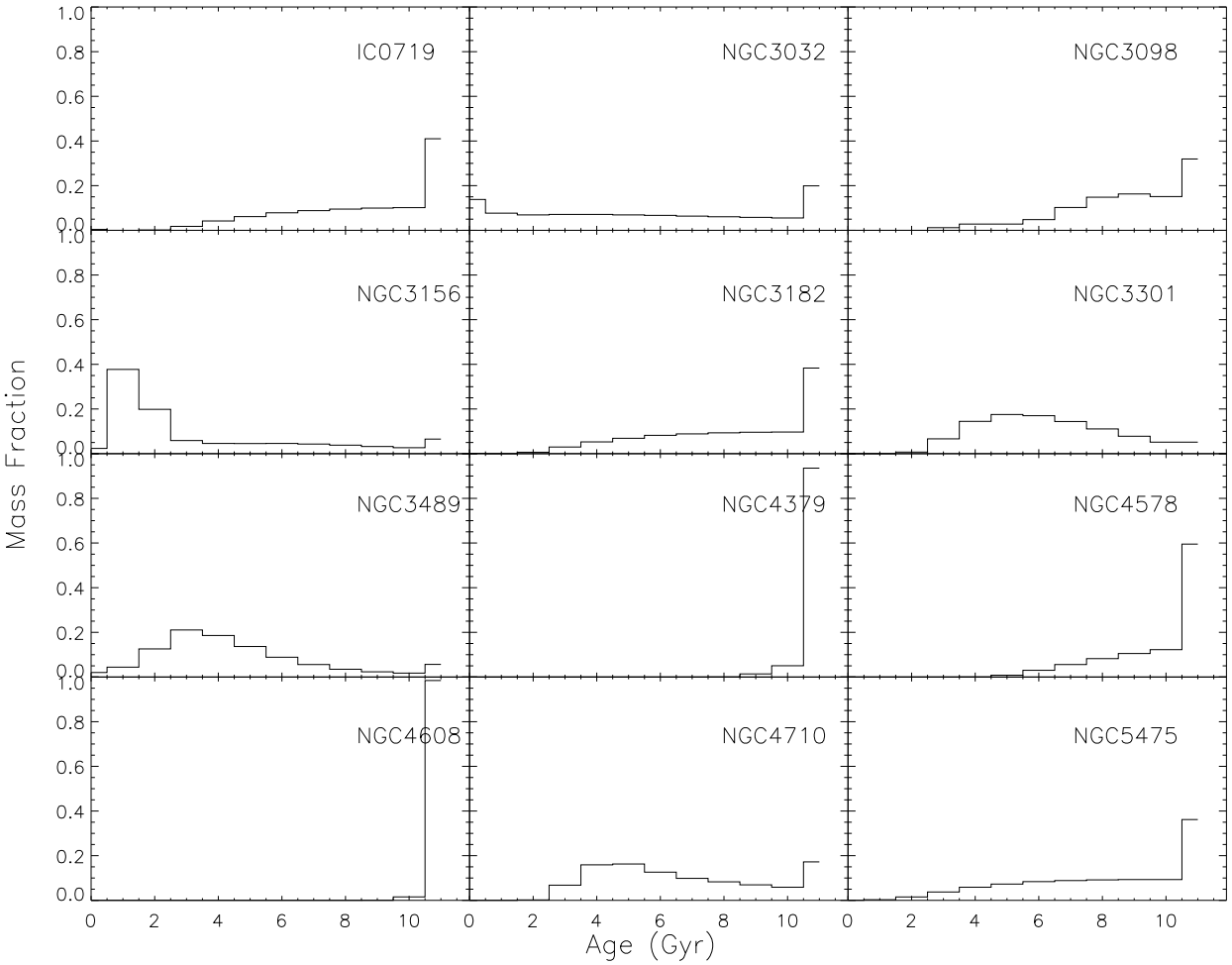

Figure 5.14: Mass fractions for each galaxy, calculated by ATLAS^{3D}.

observations over the entire near-infrared range.

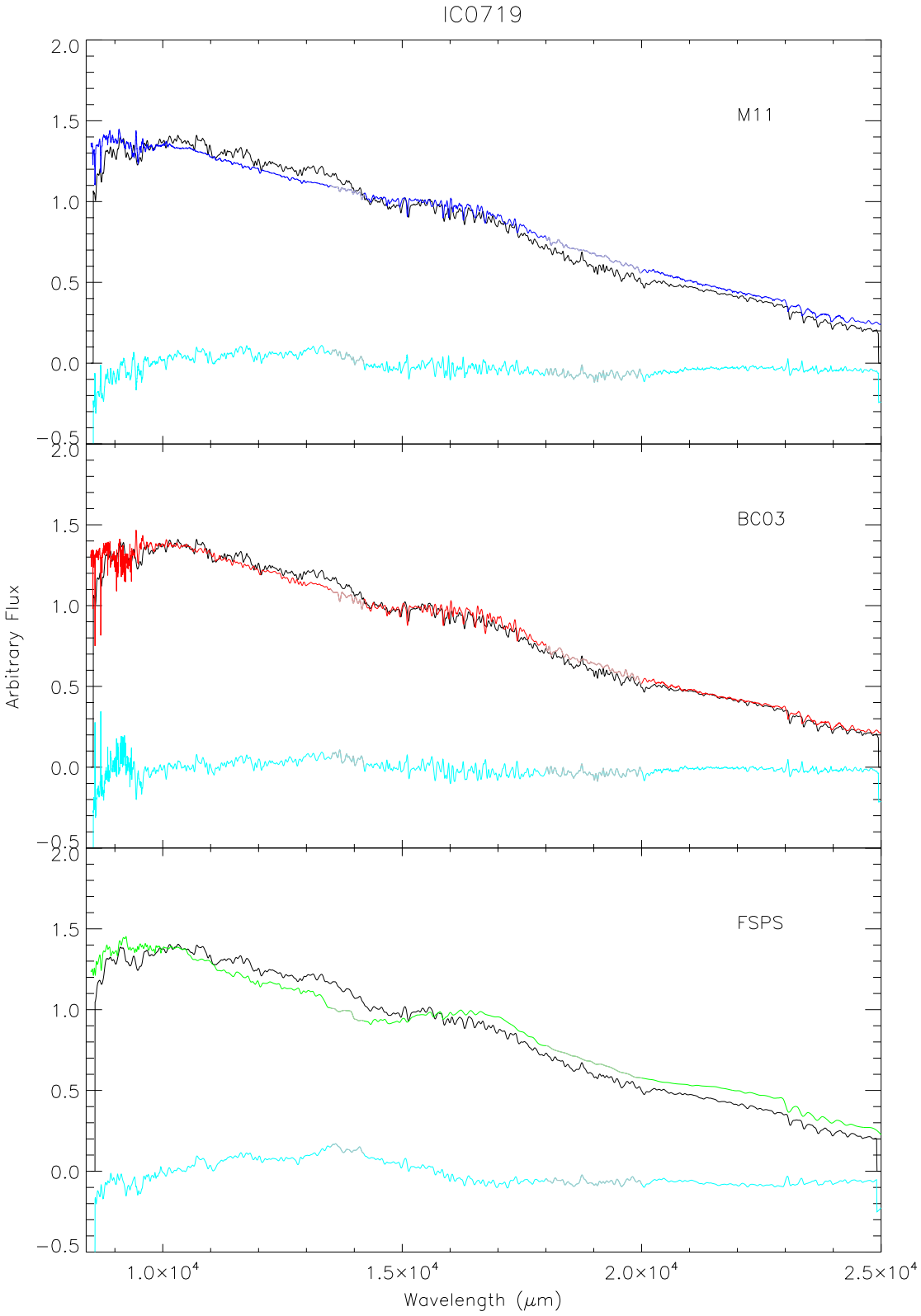

Figure 5.15: SFH fits for IC0719 for the three SPS models. The top panel shows the fit of the M11 SFH template to the galaxy, the middle shows BC03, and the bottom panel FSPS. The colours are as used previously.

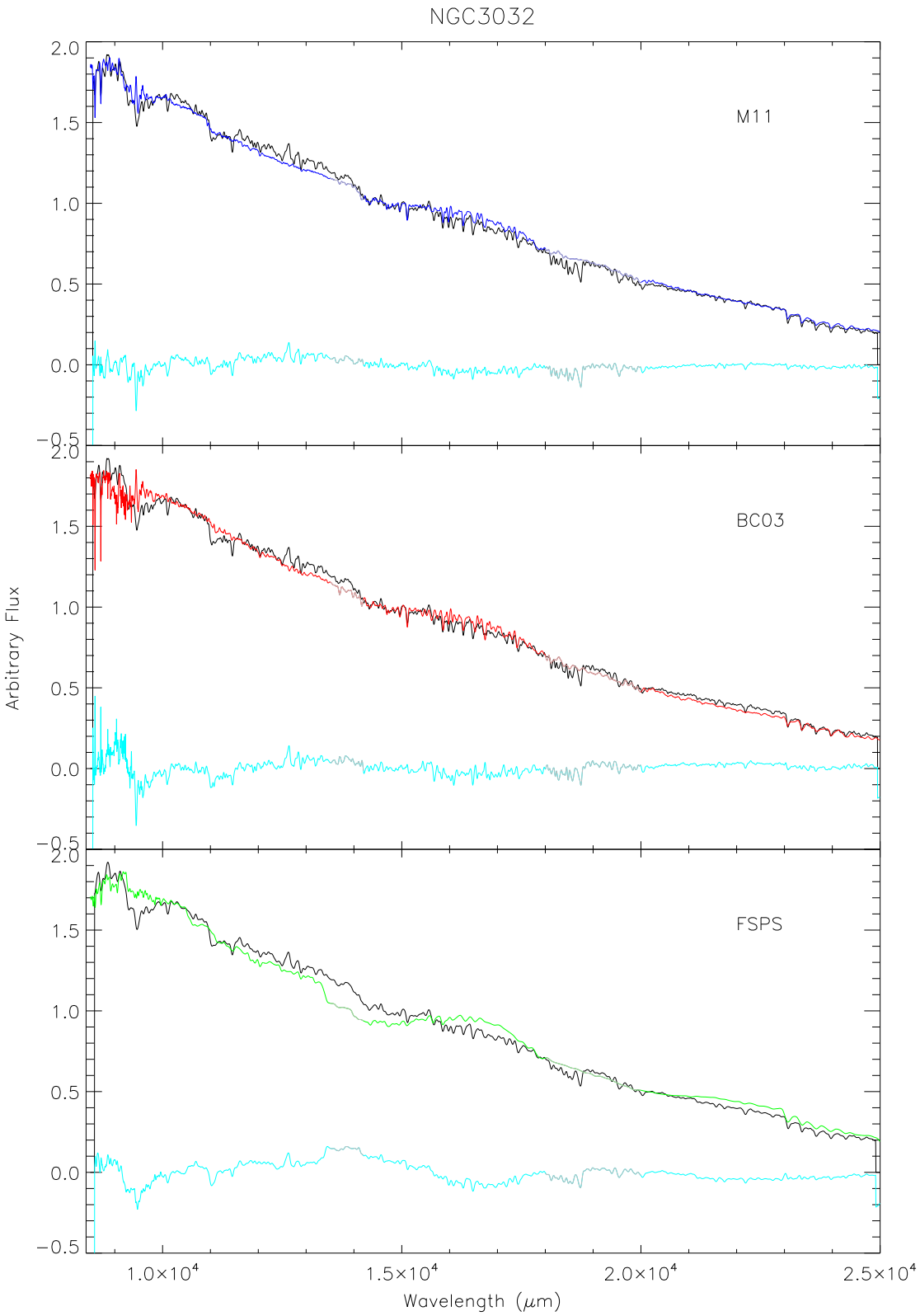

Figure 5.16: As in Figure 5.1 but for NGC3032

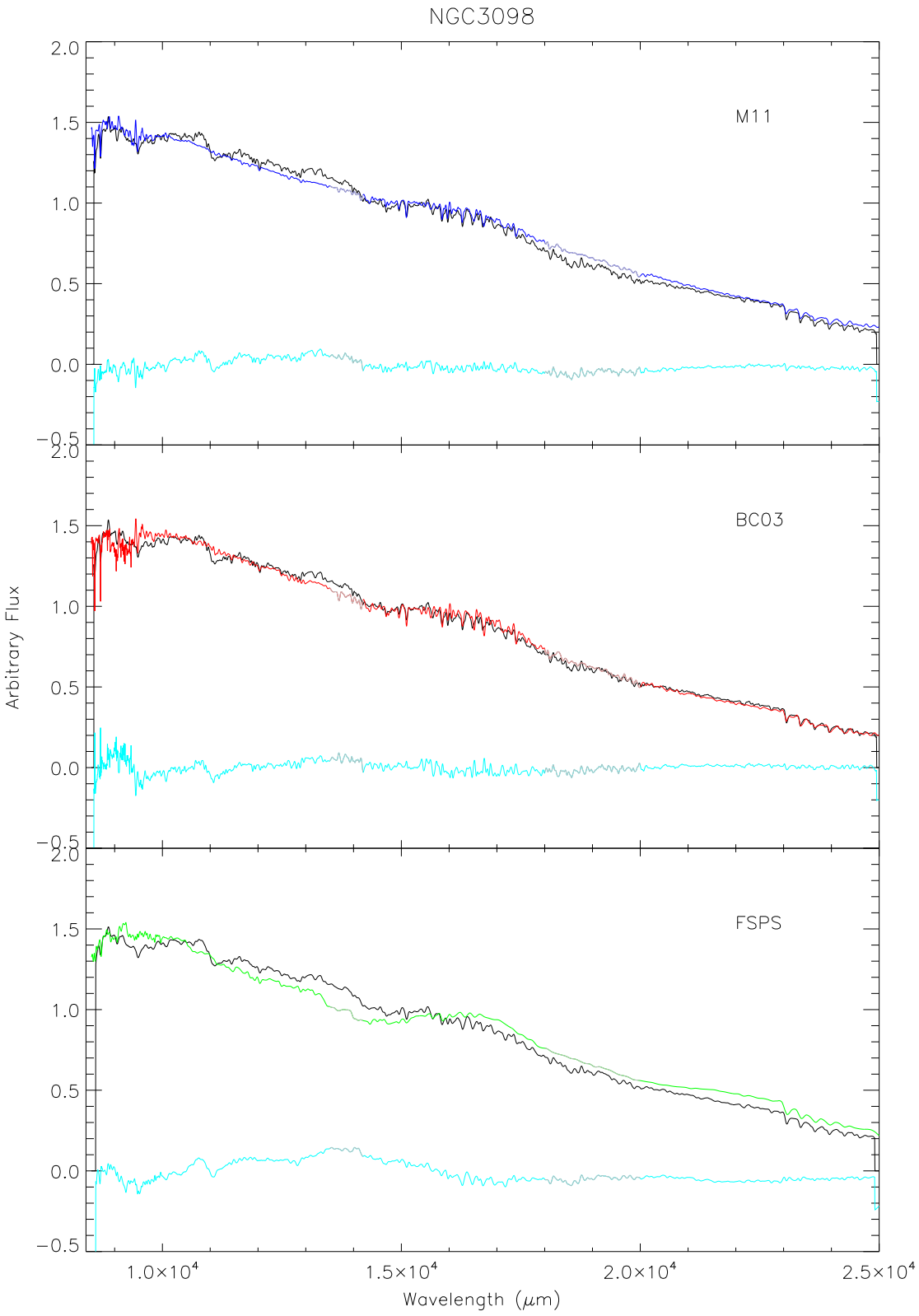

Figure 5.17: As in Figure 5.1 but for NGC3098

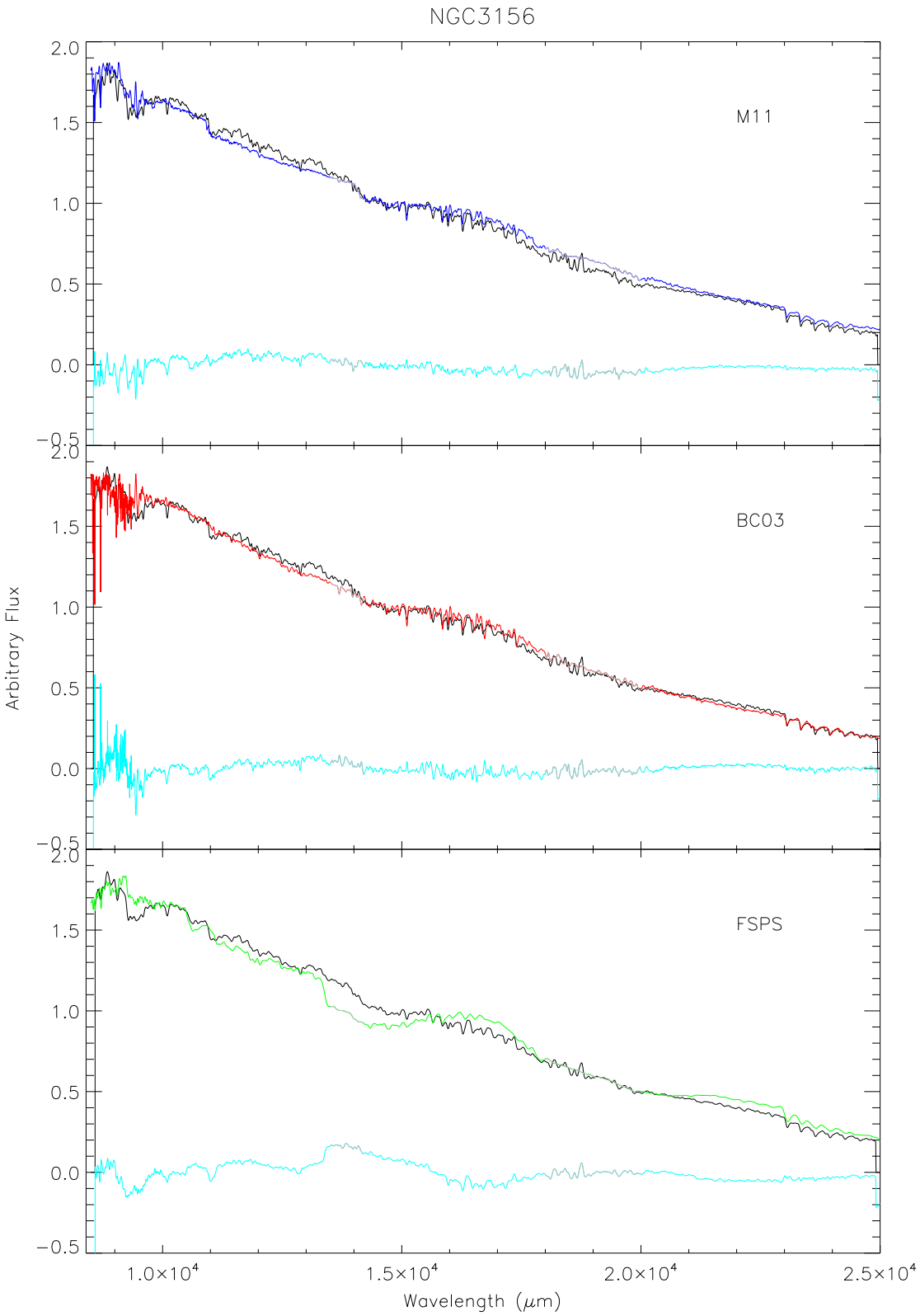

Figure 5.18: As in Figure 5.1 but for NGC3156

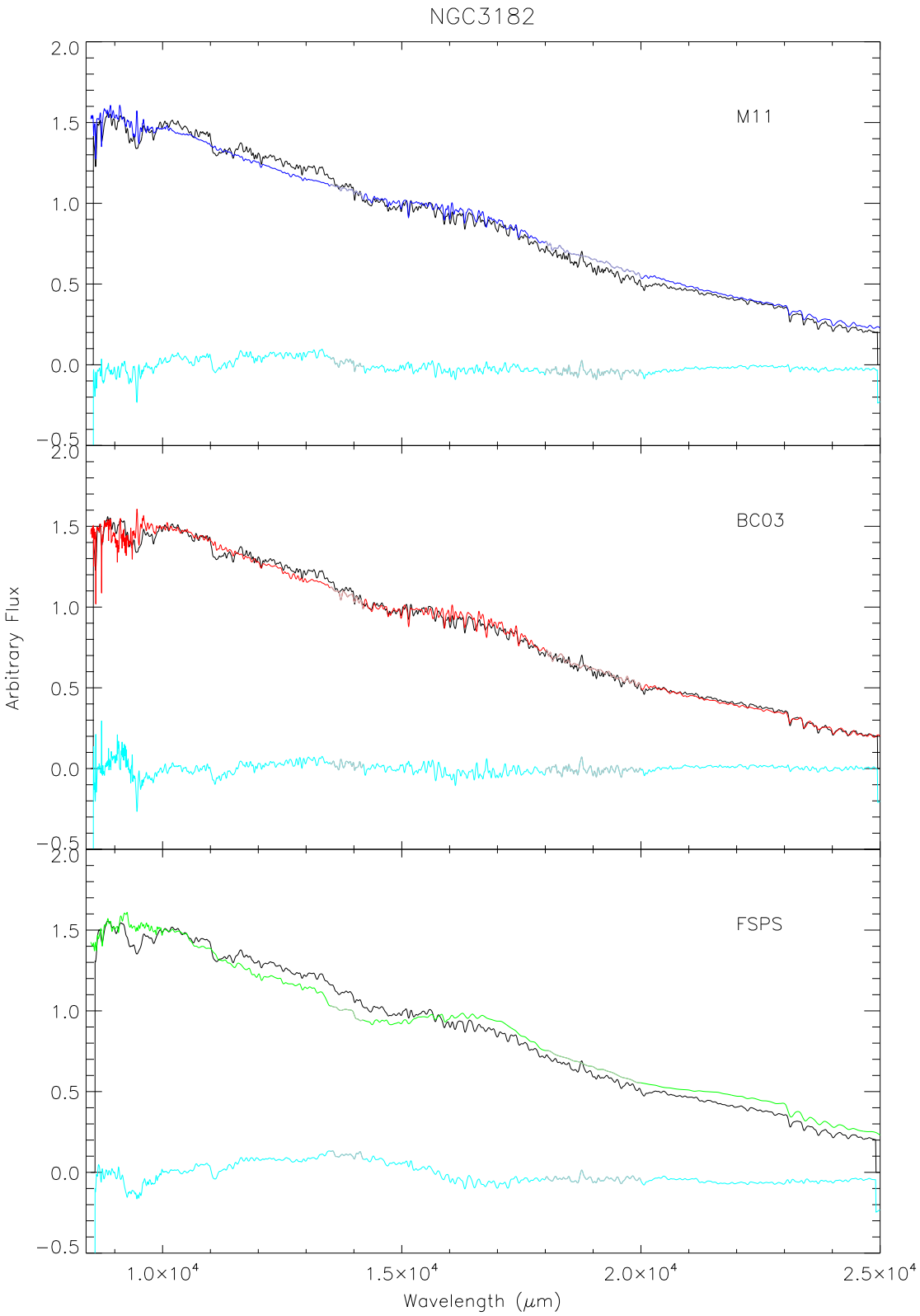

Figure 5.19: As in Figure 5.1 but for NGC3182

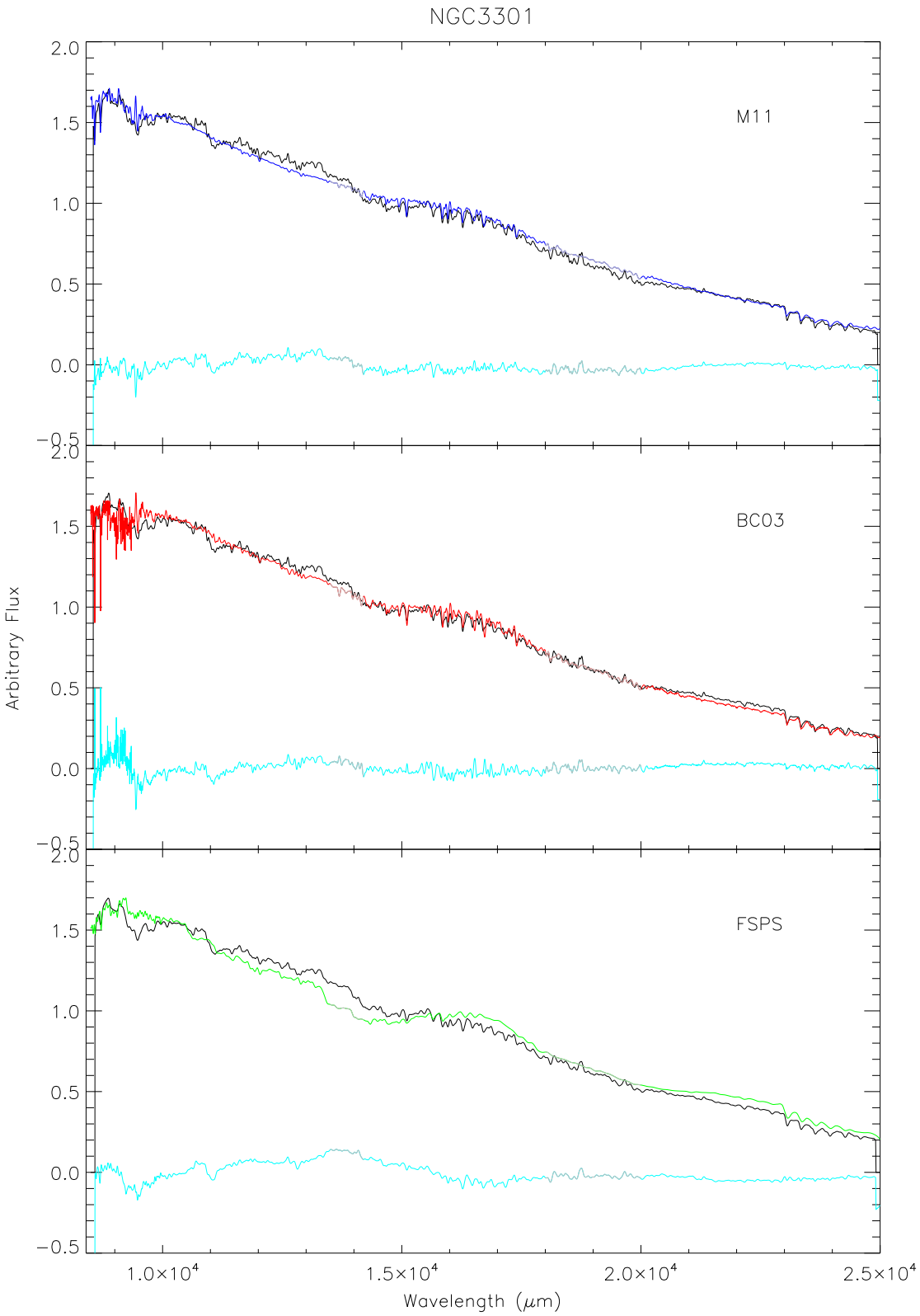

Figure 5.20: As in Figure 5.1 but for NGC3301

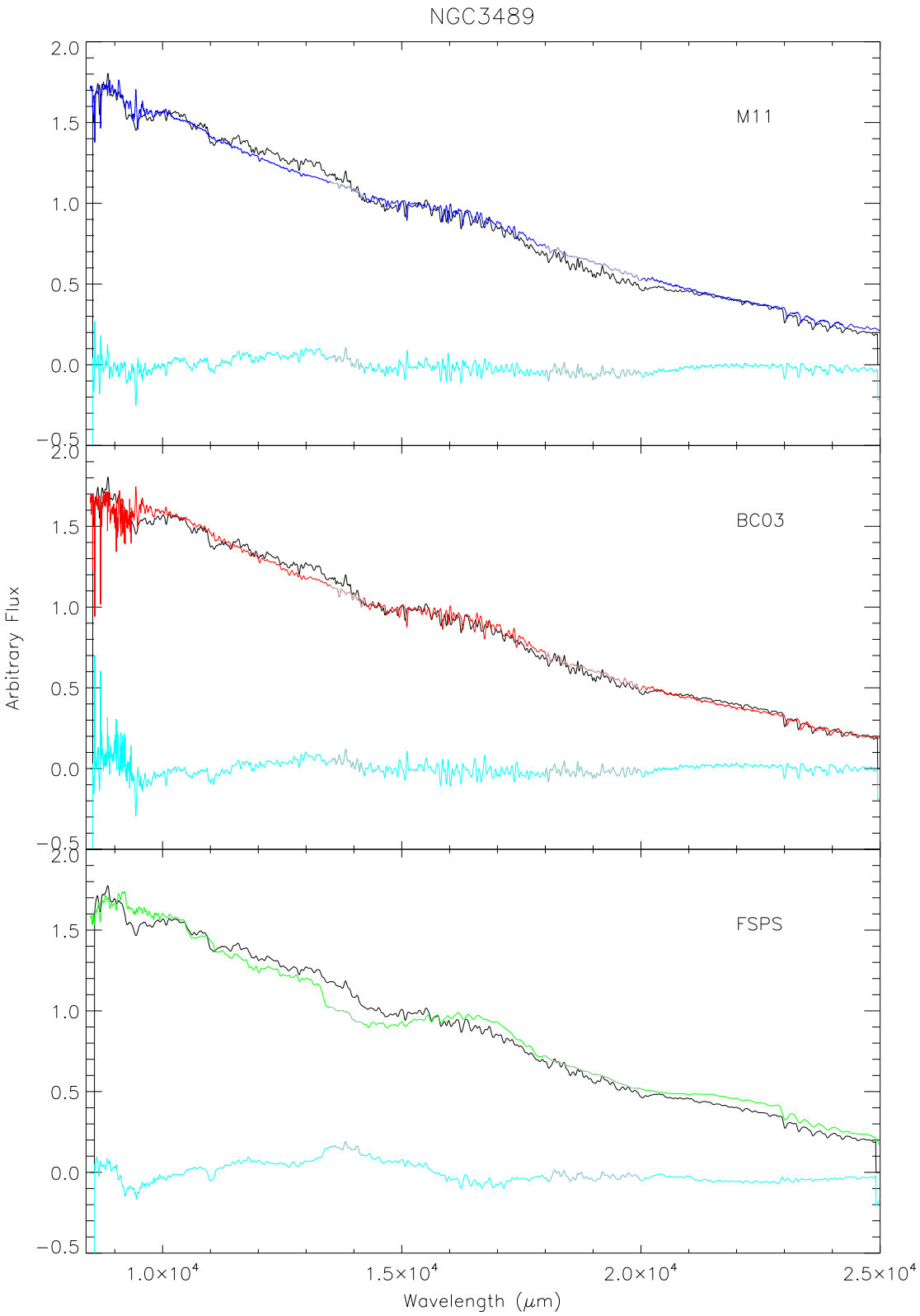

Figure 5.21: As in Figure 5.1 but for NGC3489

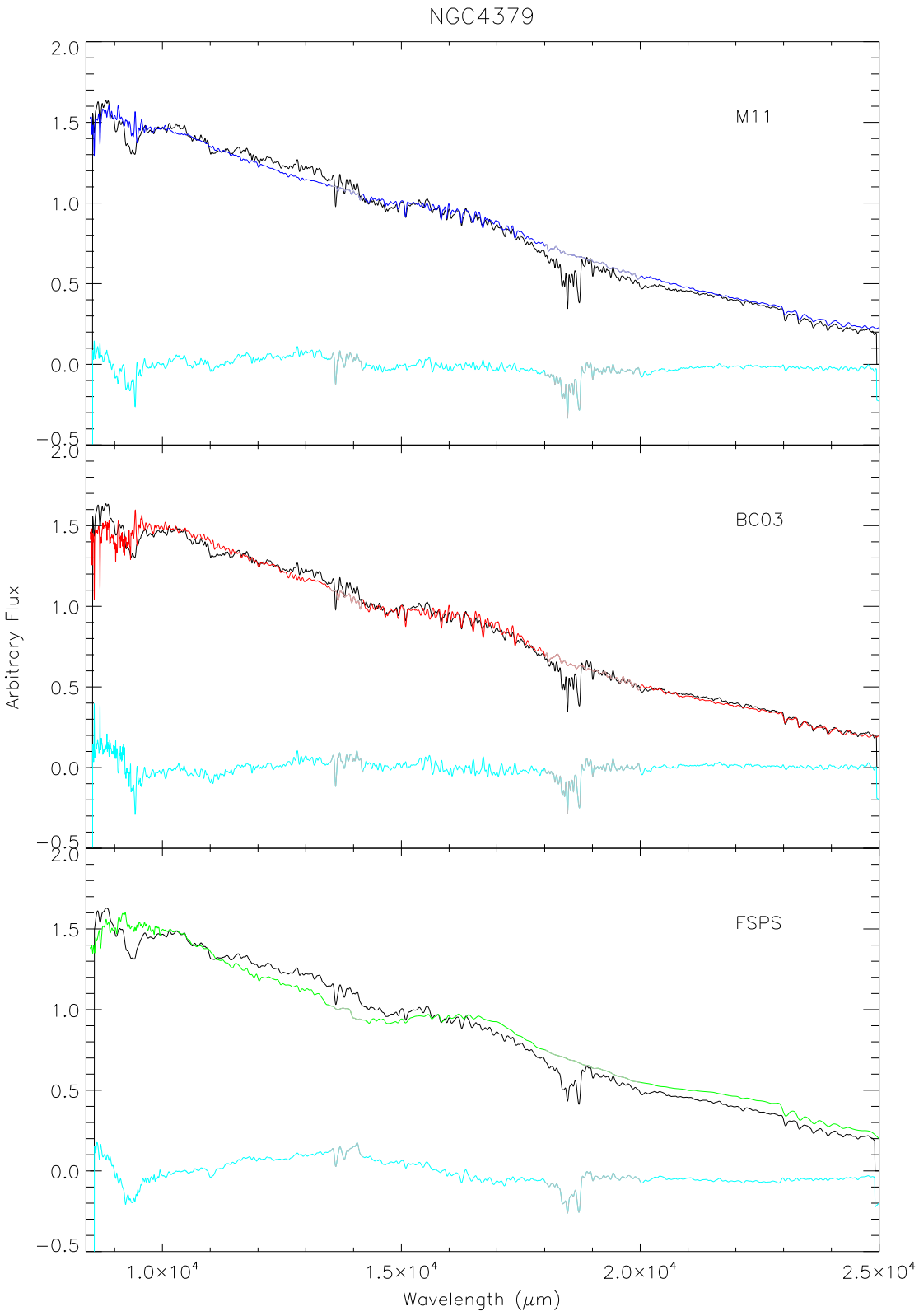

Figure 5.22: As in Figure 5.1 but for NGC4379

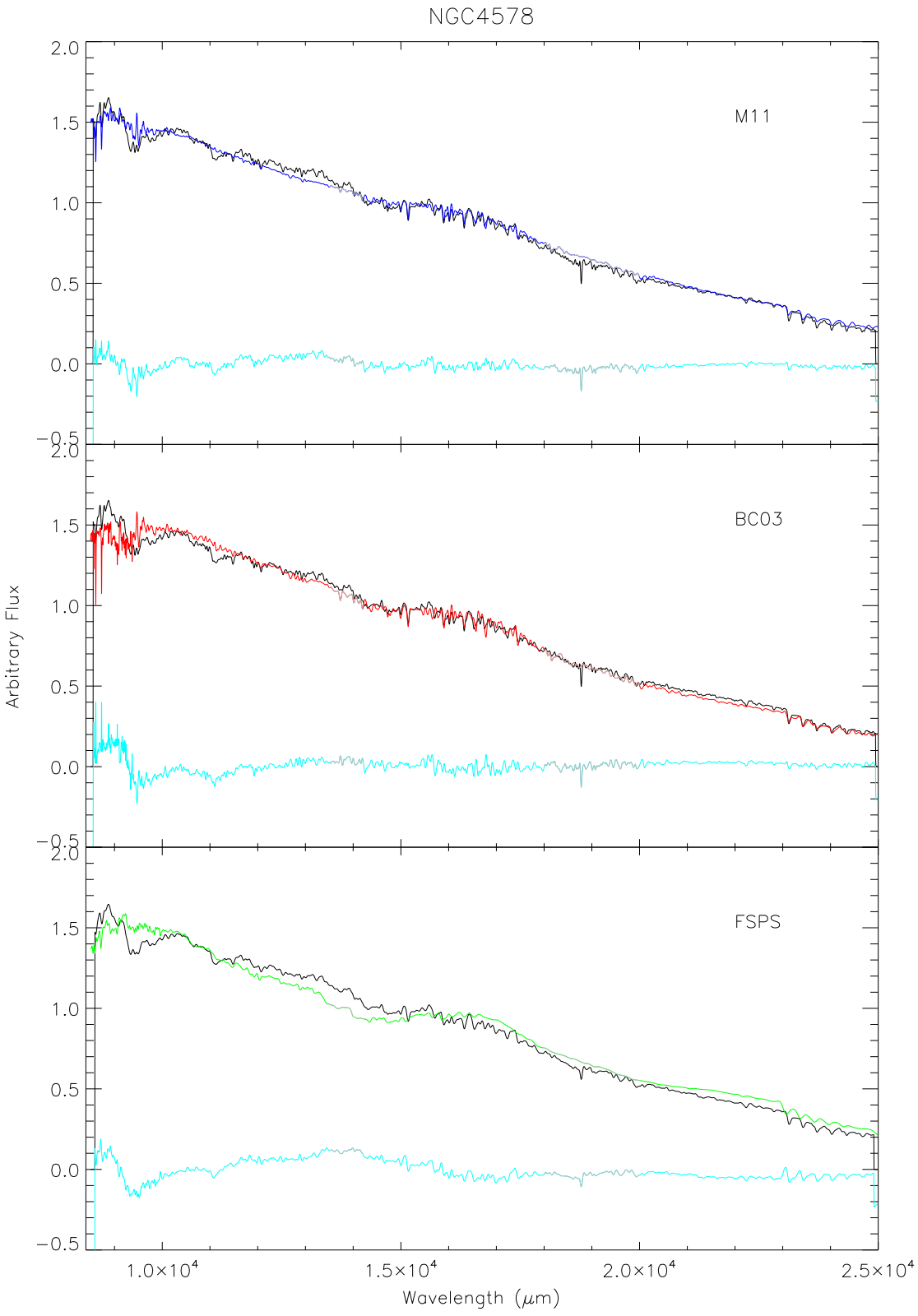

Figure 5.23: As in Figure 5.1 but for NGC4578

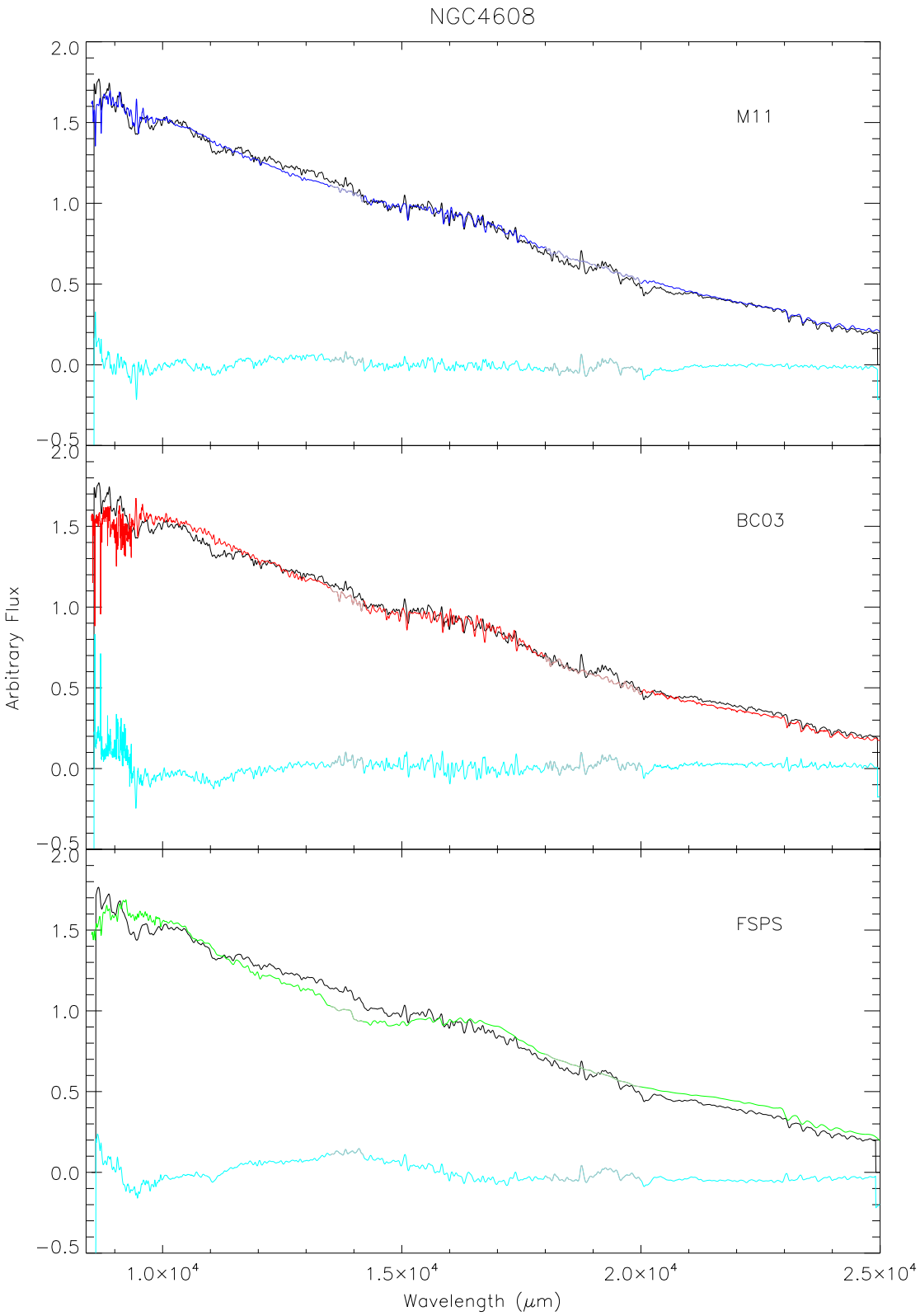

Figure 5.24: As in Figure 5.1 but for NGC4608

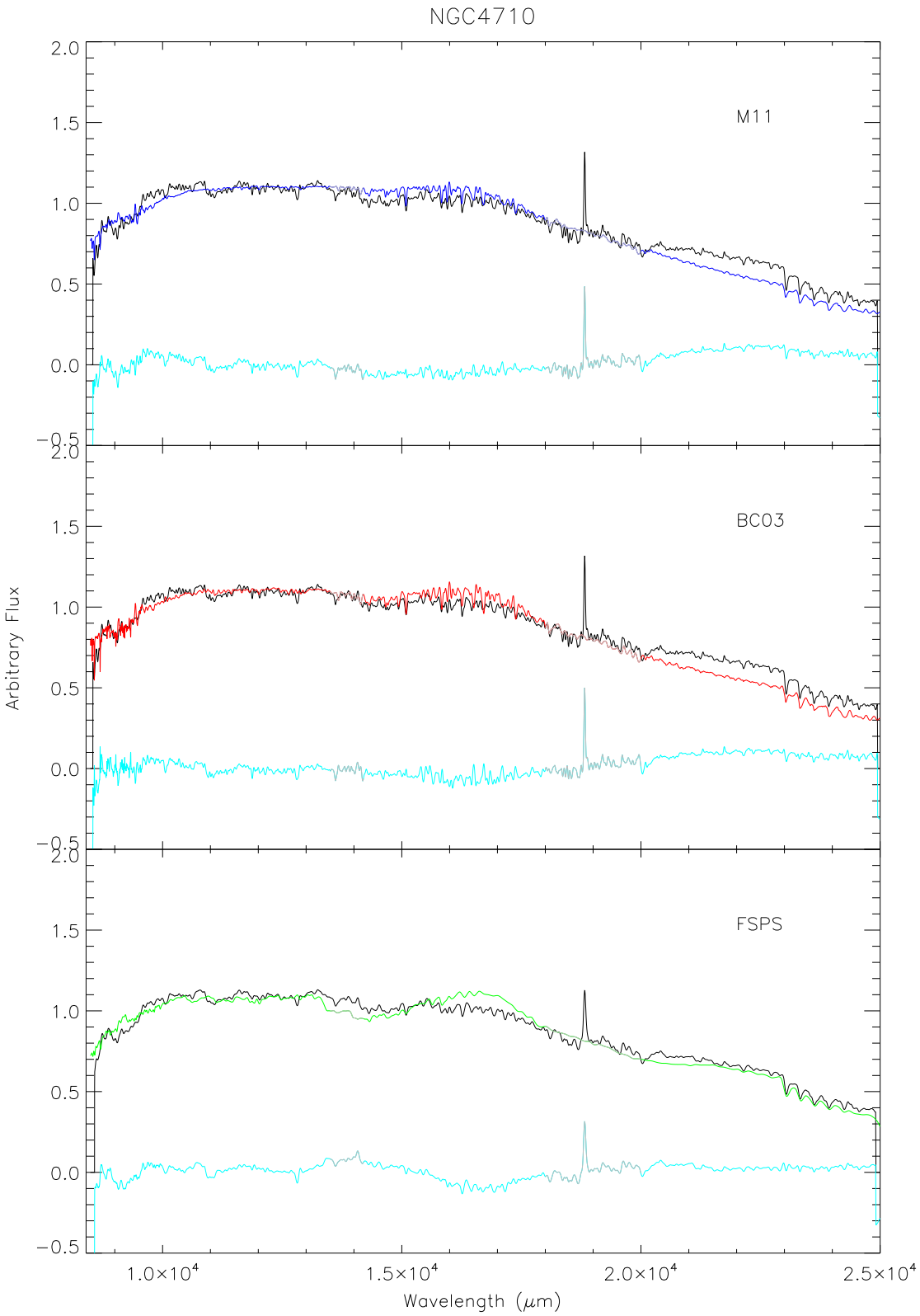

Figure 5.25: As in Figure 5.1 but for NGC4710

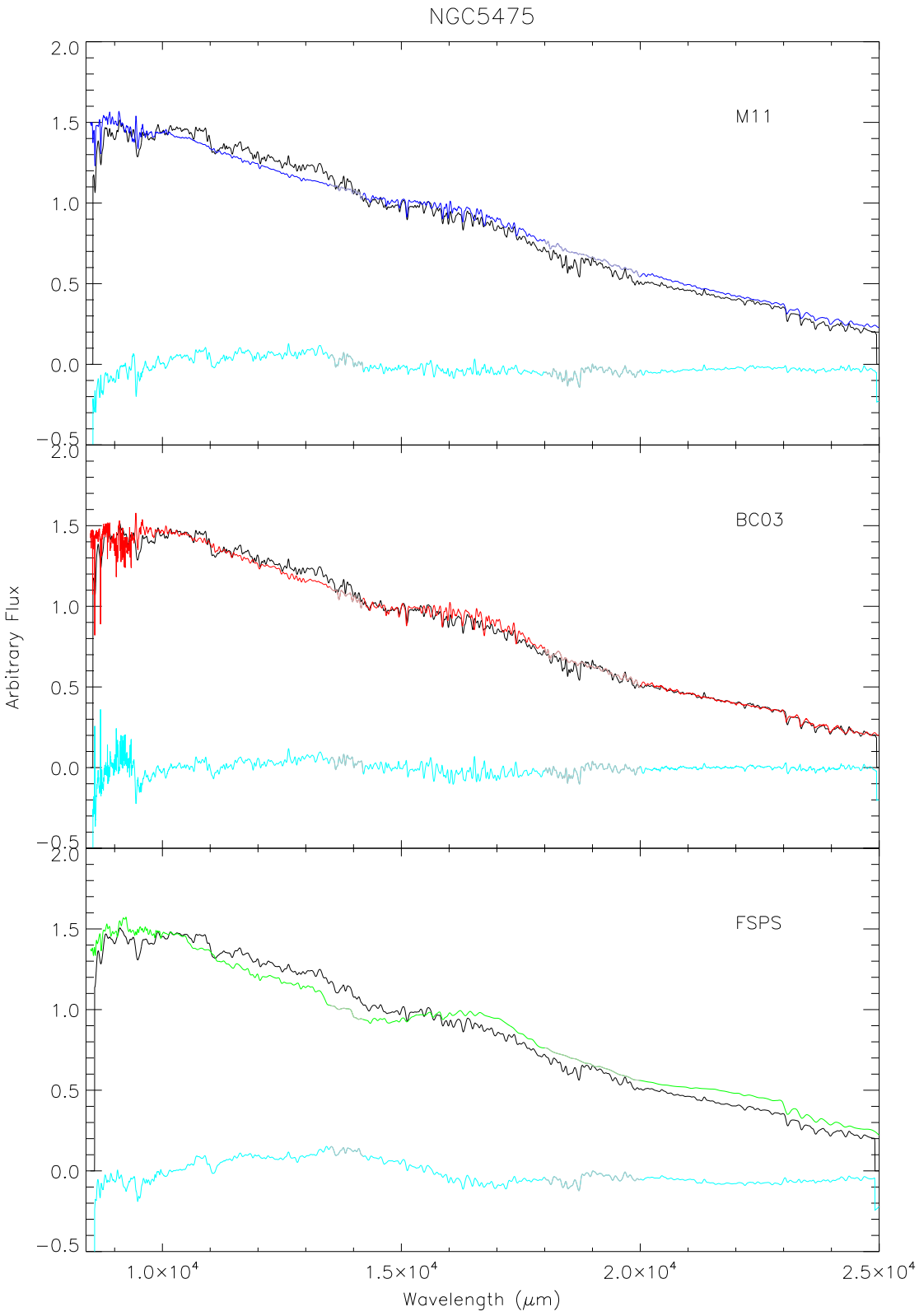

Figure 5.26: As in Figure 5.1 but for NGC5475

Chapter 6

Line Strength Analysis

The measurement of line strength indices, when compared with the predictions of single stellar populations, provides a single value of stellar population parameters such as age and metallicity. This technique has previously been used widely in studies of ETGs (e.g., Gorgas et al. 1990; Worthey et al. 1992; Davies 1996; Trager et al. 2000). The vast majority of line-strength studies have been around visible wavelengths, but with the development of sensitive infrared instruments, studies at longer wavelengths are becoming more common (e.g., Lyubenova et al. 2010, 2012, and references therein).

The measurement of individual line strengths offers the advantage that the procedure is not adversely affected by regions of uncertainty in the models. The specific features of interest are the only spectral regions in which models must be sufficiently accurate. The disadvantage of the line strength approach is that not all information present in the spectrum is utilised. The technique is also complicated by the fact that a single absorption line is typically due to a blend of nearby elements rather than the specific element we wish to trace.

6.1 Preparing the Spectra

The observed spectrum of a galaxy is a the sum of the spectra of all stars present convolved by their line-of-sight velocity distributions (LOSVD) and the instrumental broadening. These two effects weaken the intrinsic strength of the feature. To compare with SPS models, which have their own instrumental resolution and no velocity dispersion, requires some calibration.

The first step of the calibration process was to smooth all models and observations to the lowest common resolution, (i.e. the resolution of FSPS). This was done by convolving the spectra with a Gaussian of appropriate FWHM as detailed in Chapter 5. Secondly, we considered the effects of velocity dispersion. The models are at zero velocity dispersion, while the galaxies were selected to span a narrow range of velocity dispersion (83–118 km s^{-1}). In

principle, the models and galaxies should all be broadened to a common velocity dispersion, in a similar way as was done for the spectral resolution. We tested whether or not this correction was necessary by broadening the models in log space to 150 km s^{-1} (higher than the highest velocity dispersion of any galaxy). As the models are at zero velocity dispersion whereas the galaxies are fairly similar, this is the correction which would have the largest impact. The line strengths were measured on the models both with and without velocity dispersion broadening and the difference in calculated strengths was $< 1\%$ for all models at all ages. Therefore, to avoid further broadening and resampling of the data, which can introduce additional systematic uncertainties into the index measurements, we did not apply a velocity dispersion correction, as the difference was negligible for the models, and would have even less effect between individual galaxies.

Finally, before measuring the strength of the features each galaxy was corrected for its radial velocity. Every galaxy has a particular velocity with respect to the Earth, whereas the indices are defined for zero velocity. This can cause the feature of interest to be redshifted out of the central bandpass if this effect is not corrected for. As described in detail in the previous chapter, we used the penalised pixel-fitting code (pPXF) of Cappellari and Emsellem (2004) to perform spectral fitting of each galaxy. One of the outputs of the spectral fitting procedure is the observed velocity shift with respect to the (zero-velocity) templates. This was used to shift each galaxy back to its respective rest wavelength. After applying these calibrations, the strengths of chosen indices were measured in both the galaxy spectra and the model SEDs in the same way.

6.2 Error

The two main contributions to the uncertainties in measuring line indices come from the statistical Poisson noise in the index pass bands, and from errors in the assumed radial velocity. Errors in the input velocity can cause the part of the feature of interest to be shifted out of the index bandpass. Noise can affect the flux measured in the central bandpass itself or in the level calculated for the pseudocontinuum, both affecting the final measured strength of the feature. Errors on the strengths of features were estimated through Monte Carlo simulations using pPXF (pPXF is described in greater detail in Section 5.1). The errors on the kinematics (V, σ) for each galaxy were measured on many realisations of the input spectrum, after adding random noise at a level consistent with the observed error spectrum. The error spectrum was calculated based on the difference between the observed spectrum and the best-fit template created using all available model templates and up to order 10 additive polynomials to ensure an accurate fit to the galaxies' intrinsic features. The errors

on the strengths of the features themselves were then calculated by shifting the bandpasses randomly according to the velocity error and accounting for the presence of noise once again, following a Monte Carlo approach, using 500 realisations.

6.3 Results

The results of the CN measurement are plotted in Figure 6.1. The strength of the features measured in the observed galaxy spectra are plotted as black circles, against the SSP-equivalent ages calculated from their optical spectra by McDermid et al. (2014). For each of the three models, we have predictions for ages of 1-12 Gyr at solar metallicity. The model predictions are plotted in coloured lines – M11 in blue, BC03 in red and FSPS in green. A similar plot for the strength of CO is shown in Figure 6.2 and the measured values for both indices are listed in Tables 6.1 and 6.2.

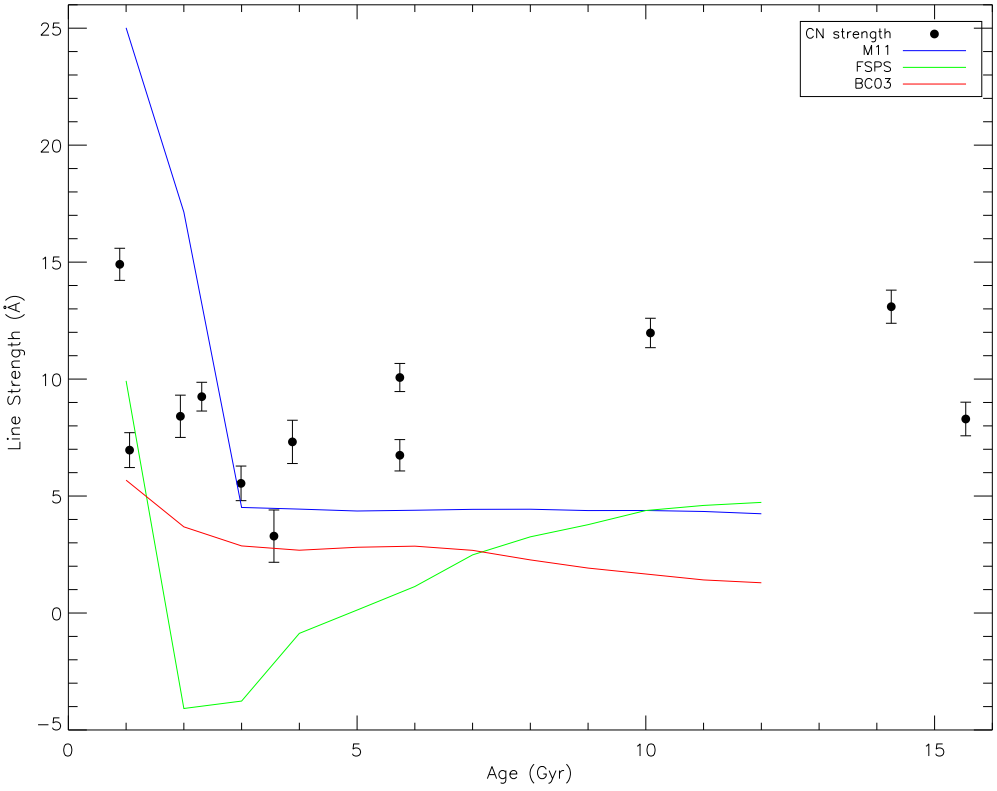

Figure 6.1: CN index measurements.

The CN index shows no clear relation with age, in contradiction to model predictions. To infer an age using the CN index (without knowledge of the optical ages), one would find the points on the model curves in Figure 6.1 which correspond to the measured values. These would point to young ages for almost all galaxies, complementing the visual inspection of the

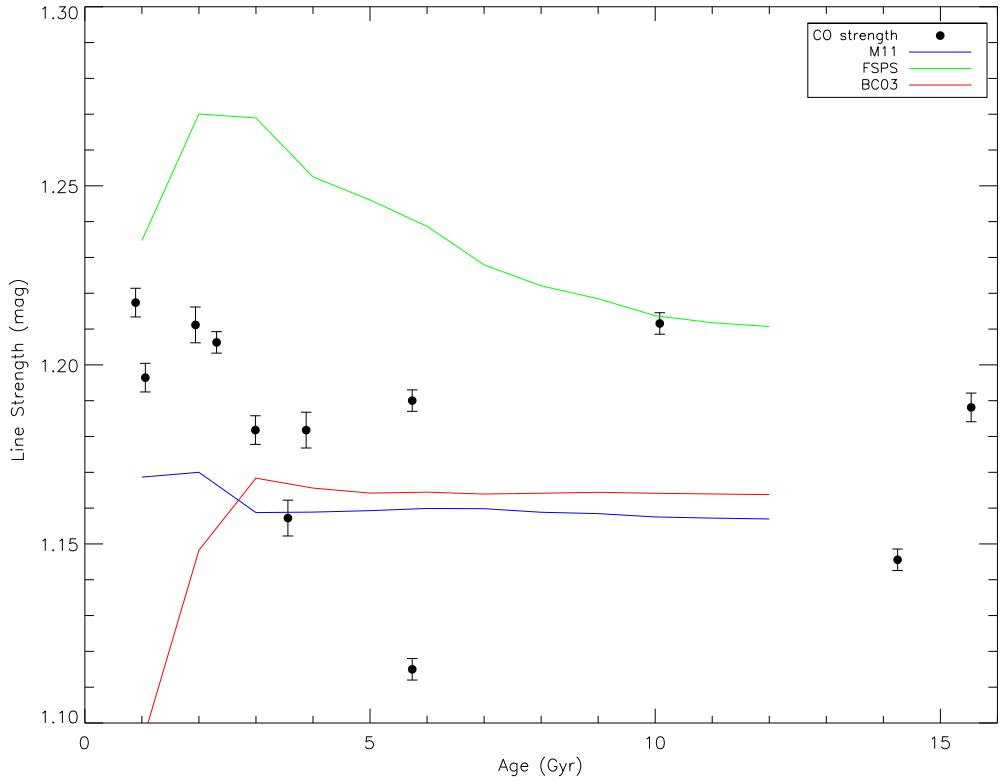

Figure 6.2: CO index measurements.

galaxies undertaken in Chapter 3, where CN was seen to be present and of similar strength in all galaxies, regardless of the optically-derived age. The youngest galaxy, NGC 3032, does however display the strongest CN break. No models manage to accurately predict the strength of the CN index. The M11 models overpredict CN strength in the youngest galaxies while underpredicting the old. BC03 underestimates CN strength at all ages. FSPS underpredict the strength, but may describe the general behaviour of the index with increasing age.

The CO index in Figure 6.2 shows a gradual decrease with age. On average, the youngest galaxies (≤ 3 Gyr) have CO strengths approximately 0.04 magnitudes higher than the older galaxies, which is a difference approximately 10 times greater than the average error. A decline in the strength of CO with age is predicted by both M11 and FSPS, although the absolute scale is incorrect for both.

6.4 Discussion

There is a clear disconnect between the predictions of all three models and the measured values for both the CN and CO indices. For example, when using the M11 models, measurements

Table 6.1: Predicted CN and CO strength.

Age	M11		BC03		FSPS	
(Gyr)	CN (Å)	CO (mag)	CN (Å)	CO (mag)	CN (Å)	CO (mag)
1	25.02	1.17	5.68	1.09	9.92	1.23
2	17.14	1.17	3.68	1.15	-4.08	1.27
3	4.51	1.16	2.87	1.17	-3.76	1.27
4	4.44	1.16	2.68	1.17	-0.87	1.25
5	4.36	1.16	2.81	1.16	0.13	1.25
6	4.39	1.16	2.86	1.16	1.13	1.24
7	4.43	1.16	2.68	1.16	2.48	1.23
8	4.44	1.16	2.27	1.16	3.26	1.22
9	4.38	1.16	1.92	1.16	3.78	1.22
10	4.38	1.16	1.67	1.16	4.38	1.21
11	4.34	1.16	1.41	1.16	4.60	1.21
12	4.24	1.16	1.29	1.16	4.73	1.21

based on near-infrared data alone would imply young ages for most galaxies. However, based on similar SSP-equivalent line measurements made in the optical, the galaxies are known to span a large range of ages. Due to the extensive optical spectral libraries, and decades of study, coupled with the high signal-to-noise of the optical data on these galaxies, we have higher confidence in the optically-derived ages than those derived using the near-infrared. The inability of the near-infrared models to accurately reproduce the optical age estimates is likely due to inaccuracies in the near-infrared models themselves rather than being an effect of different stellar populations being sampled by the optical and near-infrared spectra. GNIRS and SAURON both have similar aperture sizes, and cover approximately the same region of the galaxies. As we are studying early-type galaxies, many of which contain no traces of gas or dust, extinction cannot be the cause of the discrepancy. It is also not due to differential sensitivity of the optical and near-infrared wavelength regimes to particular stellar populations. We know this as the spectral fitting carried out using the entire star formation history, which accounted for all stellar populations present in the galaxies, did not produce better results in the near-infrared.

The lack of a clear trend for either the CN or CO indices with age is surprising, based on the clear predictions of all near-infrared models. All models predict the two indices to vary with age, although the variation itself depends strongly on the model. The differences in the model predictions are due mainly to differences in their treatments of the TP-AGB phase, but also depend somewhat on the stellar tracks and spectral libraries used.

The use of indices is, in principle, more robust against systematic errors in the models, e.g. with respect to flux calibration of the stellar libraries, broad-band opacities, etc. Here

Table 6.2: Measured Line Strengths.

Galaxy	CN Strength (Å)	CO Strength (mag)
IC 0719	14.91 ± 0.69	1.22 ± 0.004
NGC 3032	6.96 ± 0.74	1.20 ± 0.004
NGC 3098	8.41 ± 0.90	1.21 ± 0.005
NGC 3156	9.25 ± 0.61	1.21 ± 0.003
NGC 3182	5.54 ± 0.74	1.18 ± 0.004
NGC 3301	3.29 ± 1.12	1.16 ± 0.005
NGC 3489	7.32 ± 0.93	1.18 ± 0.005
NGC 4379	10.07± 0.60	1.19 ± 0.003
NGC 4578	6.74 ± 0.67	1.11 ± 0.003
NGC 4608	11.97 ± 0.63	1.21 ± 0.003
NGC 4710	13.09 ± 0.71	1.15 ± 0.003
NGC 5475	8.29 ± 0.72	1.19 ± 0.004

we have shown, however, that the models are still a poor predictor of the data. Moreover, this is not restricted to ages considered to be close to the peak of the TP-AGB contribution, suggesting additional sources of uncertainty beyond the luminosity contribution of the TP-AGB phase.

Chapter 7

Summary and Conclusions

This study carried out a series of tests on three popular SPS models, with the aim of constraining the contribution of the hotly-debated TP-AGB phase to the near-infrared spectral energy distributions of intermediate age galaxies. The tests were carried out on nuclear spectroscopy of a sample of twelve nearby early-type galaxies selected from the complete, volume-limited ATLAS^{3D} parent sample. The data are of high enough signal-to-noise to enable a detailed spectral analysis of their absorption features. The sample spans 14 Gyr in age but only a small range of metallicity, α-abundance and velocity dispersion. Its properties are well known from the parent study.

We measured the strengths of the CN index at 1.1 μm and the CO index at 2.29 μm. These indices were chosen as they are both strong, isolated features that were clearly visible in the spectra of all galaxies, and which were predicted by SPS models to vary with age. We compared the measured galaxy strengths with those predicted by the SPS models of Bruzual and Charlot (2003), Conroy et al. (2009); Conroy and Gunn (2010) and Maraston and Strömbäck (2011).

We carried out full spectral fitting of the observed spectra, fitting both individual SSPs and a composite SED predicted by the star formation history to each galaxy. We compared the quality of the fits obtained with each model as determined by the reduced χ^2. We also compared the SSP-ages estimated using each model with the ages obtained by spectral fitting of the galaxies' optical spectra carried out by ATLAS^{3D}.

Our main conclusions are as follows:

We find that contrary to model predictions, the CN index displays no clear variation with age. The CN feature is present at a similar strength in galaxies of all ages, including galaxies which are composed solely of old populations. CN is thus not an effective tracer of intermediate age populations, as has been claimed. The BC03 and FSPS models consistently underpredict CN strength, while M11 overpredicts the strength at young ages (as derived at

optical wavelengths) while underpredicting for old. The CO index displays a gradual decline with age, consistent with the predictions of M11 and FSPS, however the absolute scale is incorrect for both. Thus, none of the models accurately predict measured line strengths for these two features.

Secondly, we find that all models fall short when it comes to full fitting of the near-infrared regime. SSP ages obtained from near-infrared fitting do not correlate with ages obtained from the optical. Inclusion of multiple stellar populations as calculated by optical fitting typically give poorer fits to the data than do the best-fit SSPs, in spite of the physically motivated nature of the composite population templates. As we have high confidence in the correctness of the optical star formation history, this indicates that the SSP fits are driven by numerical and systematic effects rather than physical ones. Accounting for the star formation history does resolve the differences in CN strength between the young M11 templates and the galaxies, indicating that dilution of CN strength by old populations could be a factor. However the star formation history does nothing to resolve the discrepancy between the galaxies and the old M11 templates.

This work could be extended to explore the effect of higher order polynomials on the fits, allowing the models to focus on specific features of interest rather than being forced to fit the shape. Alternatively, the measurement of other line indices present in this spectral range avoids the need for the models to accurately match the overall spectral shape. A thorough exploration of the effects of the ΔL and ΔT parameters on the FSPS models may shed light on improvements that could be made to this model set. Alternatively, a similar approach to the one undertaken here could be used to investigate the effects of different IMFs.

Bibliography

Aaronson, M., Persson, S. E., and Frogel, J. A. (1978). Photometric studies of composite stellar systems. II - observations of h2o absorption and the coolest stellar component of e and s0 galaxies. *ApJ*, 220:442–448.

Alloin, D. and Bica, E. (1989). A comparative study of NA i and CA II infrared lines in stars, star clusters and galaxy nuclei - an alternative to the dwarf-enriched population. *A&A*, 217:57–65.

Alongi, M., Bertelli, G., Bressan, A., Chiosi, C., Fagotto, F., Greggio, L., and Nasi, E. (1993). Evolutionary sequences of stellar models with semiconvection and convective overshoot. i - z = 0.008. *A&AS*, 97:851–871.

Baugh, C. M. (2006). A primer on hierarchical galaxy formation: the semi-analytical approach. *Reports on Progress in Physics*, 69(12):3101.

Bressan, A., Bertelli, G., and Chiosi, C. (1993). Evolutionary tracks and color magnitude diagrams. volume 416, pages 352–361.

Bruzual, A. G. (2006). On TP-AGB stars and the mass of galaxies. *Proceedings of the International Astronomical Union*, 2(S241):125–132.

Bruzual, G. and Charlot, S. (2003). Stellar population synthesis at the resolution of 2003. *Monthly Notices of the Royal Astronomical Society*, 344:1000–1028.

Calzetti, D. (2001). The dust opacity of star-forming galaxies. *Publications of the Astronomical Society of the Pacific*, 113:1449–1485.

Cappellari, M. and Emsellem, E. (2004). Parametric recovery of line-of-sight velocity distributions from absorption-line spectra of galaxies via penalized likelihood. *Publications of the Astronomical Society of the Pacific*, 116(816):138–147.

Cappellari, M., Emsellem, E., Krajnović, D., McDermid, R. M., Scott, N., Verdoes Kleijn, G. A., Young, L. M., Alatalo, K., Bacon, R., Blitz, L., Bois, M., Bournaud, F., Bureau,

M., Davies, R. L., Davis, T. A., de Zeeuw, P. T., Duc, P.-A., Khochfar, S., Kuntschner, H., Lablanche, P.-Y., Morganti, R., Naab, T., Oosterloo, T., Sarzi, M., Serra, P., and Weijmans, A.-M. (2011). The ATLAS3d project - i. a volume-limited sample of 260 nearby early-type galaxies: science goals and selection criteria: The ATLAS3d project - i. the sample. *MNRAS*, 413(2):813–836.

Cappellari, M., McDermid, R. M., Alatalo, K., Blitz, L., Bois, M., Bournaud, F., Bureau, M., Crocker, A. F., Davies, R. L., Davis, T. A., de Zeeuw, P. T., Duc, P.-A., Emsellem, E., Khochfar, S., Krajnovic, D., Kuntschner, H., Lablanche, P.-Y., Morganti, R., Naab, T., Oosterloo, T., Sarzi, M., Scott, N., Serra, P., Weijmans, A.-M., and Young, L. M. (2012). Systematic variation of the stellar initial mass function in early-type galaxies. *Nature*, 484:485–488.

Carter, D., Visvanathan, N., and Pickles, A. J. (1986). The dwarf star content of elliptical and lenticular galaxies. *ApJ*, 311:637–650.

Cassisi, S., Castellani, M., and Castellani, V. (1997). Intermediate-age metal deficient stellar populations: the case of metallicity z=0.00001. *A&A*, 317:108–113.

Cenarro, A. J., Gorgas, J., Vazdekis, A., Cardiel, N., and Peletier, R. F. (2003). Near-infrared line-strengths in elliptical galaxies: evidence for initial mass function variations? *MNRAS*, 339:L12–L16.

Cenarro, A. J., Peletier, R. F., Sánchez-Blázquez, P., Selam, S. O., Toloba, E., Cardiel, N., Falcón-Barroso, J., Gorgas, J., Jiménez-Vicente, J., and Vazdekis, A. (2007). Medium-resolution isaac newton telescope library of empirical spectra - II. the stellar atmospheric parameters. *MNRAS*, 374:664–690.

Chabrier, G. (2001). The galactic disk mass budget. i. stellar mass function and density. *ApJ*, 554:1274–1281.

Cid Fernandes, R., Mateus, A., Sodré, L., Stasinska, G., and Gomes, J. M. (2005). Semi-empirical analysis of sloan digital sky survey galaxies - i. spectral synthesis method. *MNRAS*, 358:363–378.

Cirasuolo, M., McLure, R. J., Dunlop, J. S., Almaini, O., Foucaud, S., and Simpson, C. (2008). A new measurement of the evolving near-infrared galaxy luminosity function out to z˜4: a continuing challenge to theoretical models of galaxy formation. *arXiv:0804.3471 [astro-ph]*. arXiv: 0804.3471.

Cohen, J. G. (1978). Near-infrared luminosity-sensitive features in m dwarfs and giants, and in m31 and m32. *The Astrophysical Journal*, 221:788–796.

Combes, F., Young, L. M., and Bureau, M. (2007). Molecular gas and star formation in the SAURON early-type galaxies. *MNRAS*, 377:1795–1807.

Conroy, C., Graves, G. J., and van Dokkum, P. G. (2014). Early-type galaxy archeology: Ages, abundance ratios, and effective temperatures from full-spectrum fitting. *ApJ*, 780:33.

Conroy, C. and Gunn, J. E. (2010). The propagation of uncertainties in stellar population synthesis modeling. III. model calibration, comparison, and evaluation. *ApJ*, 712(2):833.

Conroy, C., Gunn, J. E., and White, M. (2009). THE PROPAGATION OF UNCERTAINTIES IN STELLAR POPULATION SYNTHESIS MODELING. i. THE RELEVANCE OF UNCERTAIN ASPECTS OF STELLAR EVOLUTION AND THE INITIAL MASS FUNCTION TO THE DERIVED PHYSICAL PROPERTIES OF GALAXIES. *ApJ*, 699(1):486–506.

Conroy, C. and van Dokkum, P. G. (2012). THE STELLAR INITIAL MASS FUNCTION IN EARLY-TYPE GALAXIES FROM ABSORPTION LINE SPECTROSCOPY. II. RESULTS. *ApJ*, 760(1):71.

Conroy, C., White, M., and Gunn, J. E. (2010). THE PROPAGATION OF UNCERTAINTIES IN STELLAR POPULATION SYNTHESIS MODELING. II. THE CHALLENGE OF COMPARING GALAXY EVOLUTION MODELS TO OBSERVATIONS. *ApJ*, 708(1):58–70.

Cooke, A. and Rodgers, B. (2005). IRAF package for GNIRS data reduction–a product of the gemini/NOAO collaboration. In *Astronomical Data Analysis Software and Systems XIV*, volume 347, page 514.

Davies, R. L. (1996). The star formation history of elliptical galaxies. volume 171, page 37.

Davis, M., Efstathiou, G., Frenk, C. S., and White, S. D. M. (1985). The evolution of large-scale structure in a universe dominated by cold dark matter. *ApJ*, 292:371–394.

Davis, T. A., Young, L. M., Crocker, A. F., Bureau, M., Blitz, L., Alatalo, K., Emsellem, E., Naab, T., Bayet, E., Bois, M., Bournaud, F., Cappellari, M., Davies, R. L., de Zeeuw, P. T., Duc, P.-A., Khochfar, S., Krajnovic, D., Kuntschner, H., McDermid, R. M., Morganti, R., Oosterloo, T., Sarzi, M., Scott, N., Serra, P., and Weijmans, A.-M. (2014). The ATLAS3d

project - XXVIII. dynamically-driven star formation suppression in early-type galaxies. *arXiv:1403.4850 [astro-ph]*. arXiv: 1403.4850.

Diaz, A. I., Terlevich, E., and Terlevich, R. (1989). Near-IR features in late type stars - their relation with stellar atmosphere parameters. *MNRAS*, 239:325–345.

Eggen, O. J., Lynden-Bell, D., and Sandage, A. R. (1962). Evidence from the motions of old stars that the galaxy collapsed. *ApJ*, 136:748.

Elias, J. H., Joyce, R. R., Liang, M., Muller, G. P., Hileman, E. A., and George, J. R. (2006a). Design of the gemini near-infrared spectrograph. In McLean, I. S. and Iye, M., editors, *Ground-based and Airborne Instrumentation for Astronomy*, pages 62694C–62694C–12. Proc. SPIE.

Elias, J. H., Rodgers, B., Joyce, R. R., Lazo, M., Doppmann, G., Winge, C., and Rodríguez-Ardila, A. (2006b). Performance of the gemini near-infrared spectrograph. In *Ground-based and Airborne Instrumentation for Astronomy*, volume 6269, page 14. Proc. SPIE.

Fagotto, F., Bressan, A., Bertelli, G., and Chiosi, C. (1994). Evolutionary sequences of stellar models with new radiative opacities. III. z=0.0004 and z=0.05. *A&AS*, 104:365–376.

Fioc, M. and Rocca-Volmerange, B. (1997). PEGASE: a UV to NIR spectral evolution model of galaxies-application to the calibration of bright galaxy counts. *Arxiv preprint astro-ph/9707017*.

Frogel, J. A., Persson, S. E., Matthews, K., and Aaronson, M. (1978). Photometric studies of composite stellar systems. i - CO and JHK observations of e and s0 galaxies. *ApJ*, 220:75–97.

Gorgas, J., Efstathiou, G., and Aragon Salamanca, A. (1990). Line strengths in early-type galaxies. *Monthly Notices of the Royal Astronomical Society*, 245:217–237.

Gustafsson, B., Edvardsson, B., Eriksson, K., Jørgensen, U. G., Nordlund, å., and Plez, B. (2008). A grid of MARCS model atmospheres for late-type stars. *Astronomy and Astrophysics*, 486(3):951–970.

Herwig, F., Blöcker, T., and Driebe, T. (2000). TP-AGB evolution with overshoot for low-mass stars as a function of metallicity. *Memorie della Societa Astronomica Italiana*, 71:745.

Horne, K. (1986). An optimal extraction algorithm for CCD spectroscopy. *Publications of the Astronomical Society of the Pacific*, 98:609–617.

Hubble, E. P. (1926). Extragalactic nebulae. *ApJ*, 64:321–369.

Ilbert, O., McCracken, H. J., Le Fèvre, O., Capak, P., Dunlop, J., Karim, A., Renzini, M. A., Caputi, K., Boissier, S., Arnouts, S., Aussel, H., Comparat, J., Guo, Q., Hudelot, P., Kartaltepe, J., Kneib, J. P., Krogager, J. K., Le Floc'h, E., Lilly, S., Mellier, Y., Milvang-Jensen, B., Moutard, T., Onodera, M., Richard, J., Salvato, M., Sanders, D. B., Scoville, N., Silverman, J. D., Taniguchi, Y., Tasca, L., Thomas, R., Toft, S., Tresse, L., Vergani, D., Wolk, M., and Zirm, A. (2013). Mass assembly in quiescent and star-forming galaxies since z ˜= 4 from UltraVISTA. *A&A*, 556:55.

Irwin, M. J., Lewis, J., Hodgkin, S., Bunclark, P., Evans, D., McMahon, R., Emerson, J. P., Stewart, M., and Beard, S. (2004). VISTA data flow system: pipeline processing for WFCAM and VISTA. In Quinn, P. J. and Bridger, A., editors, *Optimizing Scientific Return for Astronomy through Information Technologies*, volume 5493 of *Society of Photo-Optical Instrumentation Engineers (SPIE) Conference Series*, pages 411–422.

Jones, J. E., Alloin, D. M., and Jones, B. J. T. (1984). The infrared CA II triplet - a luminosity indicator for stellar population synthesis. *ApJ*, 283:457–465.

Kaviraj, S., Khochfar, S., Schawinski, K., Yi, S. K., Gawiser, E., Silk, J., Virani, S. N., Cardamone, C. N., van Dokkum, P. G., and Urry, C. M. (2008). The UV colours of high-redshift early-type galaxies: evidence for recent star formation and stellar mass assembly over the last 8 billion years. *MNRAS*, 388:67–79.

Koleva, M., Prugniel, P., Bouchard, A., and Wu, Y. (2009). ULySS: a full spectrum fitting package. *A&A*, 501:1269–1279.

Kriek, M., Labbé, I., Conroy, C., Whitaker, K. E., van Dokkum, P. G., Brammer, G. B., Franx, M., Illingworth, G. D., Marchesini, D., Muzzin, A., Quadri, R. F., and Rudnick, G. (2010). THE SPECTRAL ENERGY DISTRIBUTION OF POST-STARBURST GALAXIES IN THE NEWFIRM MEDIUM-BAND SURVEY: A LOW CONTRIBUTION FROM TP-AGB STARS. *ApJ*, 722(1):L64–L69.

Kroupa, P. (2001). On the variation of the initial mass function. *MNRAS*, 322:231–246.

Kuntschner, H., Emsellem, E., Bacon, R., Cappellari, M., Davies, R. L., De Zeeuw, P. T., Falcón-Barroso, J., Krajnović, D., McDermid, R. M., Peletier, R. F., Sarzi, M., Shapiro, K. L., Van Den Bosch, R. C. E., and Van De Ven, G. (2010). The SAURON project - XVII. stellar population analysis of the absorption line strength maps of 48 early-type galaxies: The SAURON project - XVII. *MNRAS*, 408(1):97–132.

Kurucz, R. (1993). ATLAS9 stellar atmosphere programs and 2 km/s grid. *ATLAS9 Stellar Atmosphere Programs and 2 km/s grid. Kurucz CD-ROM No. 13. Cambridge, Mass.: Smithsonian Astrophysical Observatory, 1993.*, 13.

Kurucz, R. L. (1992). Model atmospheres for population synthesis. volume 149, page 225.

Lacy, M., Ridgway, S. E., Gates, E. L., Nielsen, D. M., Petric, A. O., Sajina, A., Urrutia, T., Drews, S. C., Harrison, C., Seymour, N., and Storrie-Lombardi, L. J. (2013). The spitzer mid-infrared active galactic nucleus survey. i. optical and near-infrared spectroscopy of obscured candidates and normal active galactic nuclei selected in the mid-infrared. *ApJS*, 208(2):24.

Lançon, A. (1998). A critical look at the role of AGB stars in stellar population synthesis. *arXiv preprint astro-ph/9810474*.

Lançon, A., Hauschildt, P. H., Ladjal, D., and Mouhcine, M. (2007). Near-IR spectra of red supergiants and giants. i. models with solar and with mixing-induced surface abundance ratios. *A&A*, 468:205–220.

Lançon, A. and Mouhcine, M. (2002). The modelling of intermediate-age stellar populations. II. average spectra for upper AGB stars, and their use. *A&A*, 393:167–181.

Larson, R. B. and Tinsley, B. M. (1978). Star formation rates in normal and peculiar galaxies. *ApJ*, 219:46–59.

Le Borgne, J.-F., Bruzual, G., Pelló, R., Lançon, A., Rocca-Volmerange, B., Sanahuja, B., Schaerer, D., Soubiran, C., and Vílchez-Gómez, R. (2003). STELIB: A library of stellar spectra at r ˜ 2000. *A&A*, 402:433–442.

Lejeune, T., Cuisinier, F., and Buser, R. (1997). Standard stellar library for evolutionary synthesis. i. calibration of theoretical spectra. *A&AS*, 125:229–246.

Lejeune, T., Cuisinier, F., and Buser, R. (1998). A standard stellar library for evolutionary synthesis. II. the m dwarf extension. *A&AS*, 130:65–75.

Lejeune, T. and Schaerer, D. (2001). Database of geneva stellar evolution tracks and isochrones for (UBV)j(RI)c JHKLL'm, HST-WFPC2, geneva and washington photometric systems. *A&A*, 366:538–546.

Lemson, G. and Consortium, t. V. (2006). Halo and galaxy formation histories from the millennium simulation: Public release of a VO-oriented and SQL-queryable database for

studying the evolution of galaxies in the LambdaCDM cosmogony. *arXiv:astro-ph/0608019*. arXiv: astro-ph/0608019.

Lord, S. (1992). ATRAN.

Lyubenova, M., Kuntschner, H., Rejkuba, M., Silva, D. R., Kissler-Patig, M., and Tacconi-Garman, L. E. (2012). Integrated J - and H -band spectra of globular clusters in the LMC: implications for stellar population models and galaxy age dating. *A&A*, 543:A75.

Lyubenova, M., Kuntschner, H., Rejkuba, M., Silva, D. R., Kissler-Patig, M., Tacconi-Garman, L. E., and Larsen, S. S. (2010). Integrated K -band spectra of old and intermediate-age globular clusters in the large magellanic cloud. *A&A*, 510:A19.

MacArthur, L. A., McDonald, M., Courteau, S., and González, J. J. (2010). INTEGRATED STELLAR POPULATIONS: CONFRONTING PHOTOMETRY WITH SPECTROSCOPY. *ApJ*, 718(2):768–773.

Malkan, M. A., Hicks, E. K., Teplitz, H. I., McLean, I. M., Sugai, H., and Guichard, J. (2002). 1-1.4 micron spectral atlas of stars. *ApJS*, 142:79–94.

Maraston, C. (1998). Evolutionary synthesis of stellar populations: a modular tool. *MNRAS*, 300(3):872–892.

Maraston, C. (2005). Evolutionary population synthesis: models, analysis of the ingredients and application to high-z galaxies. *MNRAS*, 362:799–825.

Maraston, C. (2006). High-redshift galaxies and the TP-AGB phase. *Proceedings of the International Astronomical Union*, 2(S241).

Maraston, C., Daddi, E., Renzini, A., Cimatti, A., Dickinson, M., Papovich, C., Pasquali, A., and Pirzkal, N. (2006). Evidence for TP-AGB stars in high-redshift galaxies, and their effect on deriving stellar population parameters. *ApJ*, 652(1):85.

Maraston, C. and Strömbäck, G. (2011). Stellar population models at high spectral resolution: High-resolution stellar population models. *MNRAS*, 418(4):2785–2811.

Marchesini, D., van Dokkum, P. G., Förster Schreiber, N. M., Franx, M., Labbé, I., and Wuyts, S. (2009). THE EVOLUTION OF THE STELLAR MASS FUNCTION OF GALAXIES FROM $z = 4.0$ AND THE FIRST COMPREHENSIVE ANALYSIS OF ITS UNCERTAINTIES: EVIDENCE FOR MASS-DEPENDENT EVOLUTION. *ApJ*, 701(2):1765–1796.

Marigo, P. and Girardi, L. (2007). Evolution of asymptotic giant branch stars. i. updated synthetic TP-AGB models and their basic calibration. *A&A*, 469:239–263.

Marigo, P., Girardi, L., Bressan, A., Groenewegen, M. A. T., Silva, L., and Granato, G. L. (2008). Evolution of asymptotic giant branch stars. *A&A*, 482(3):883–905.

Mármol-Queraltó, E., Cardiel, N., Cenarro, A. J., Vazdekis, A., Gorgas, J., Pedraz, S., Peletier, R. F., and Sánchez-Blázquez, P. (2008). A new stellar library in the region of the CO index at 2.3 μm. *A&A*, 489(2):885–909.

Melbourne, J., Williams, B. F., Dalcanton, J. J., Rosenfield, P., Girardi, L., Marigo, P., Weisz, D., Dolphin, A., Boyer, M. L., Olsen, K., Skillman, E., and Seth, A. C. (2012). THE CONTRIBUTION OF TP-AGB AND RHeB STARS TO THE NEAR-IR LUMINOSITY OF LOCAL GALAXIES: IMPLICATIONS FOR STELLAR MASS MEASUREMENTS OF HIGH-REDSHIFT GALAXIES. *ApJ*, 748(1):47.

Navarro, J. F., Frenk, C. S., and White, S. D. M. (1995). The assembly of galaxies in a hierarchically clustering universe. *MNRAS*, 275:56–66.

Ocvirk, P., Pichon, C., Lançon, A., and Thiébaut, E. (2006). STECMAP: STEllar content from high-resolution galactic spectra via maximum a posteriori. *MNRAS*, 365:46–73.

Origlia, L. and Oliva, E. (2000). Is the [CO] index an age indicator for star forming galaxies? *arXiv preprint astro-ph/0003131*.

Pérez-González, P. G., Rieke, G. H., Villar, V., Barro, G., Blaylock, M., Egami, E., Gallego, J., Gil de Paz, A., Pascual, S., Zamorano, J., and Donley, J. L. (2008). The stellar mass assembly of galaxies from z = 0 to z = 4: Analysis of a sample selected in the rest-frame near-infrared with spitzer. *ApJ*, 675:234–261.

Perryman, M. A. C., Lindegren, L., Kovalevsky, J., Hoeg, E., Bastian, U., Bernacca, P. L., Crézé, M., Donati, F., Grenon, M., Grewing, M., van Leeuwen, F., van der Marel, H., Mignard, F., Murray, C. A., Le Poole, R. S., Schrijver, H., Turon, C., Arenou, F., Froeschlé, M., and Petersen, C. S. (1997). The HIPPARCOS catalogue. *A&A*, 323:L49–L52.

Persson, S. E., Cohen, J. G., Sellgren, K., Mould, J., and Frogel, J. A. (1980). Infrared photometry of the semistellar nucleus of m31. *The Astrophysical Journal*, 240:779–784.

Pickles, A. J. (1998). A stellar spectral flux library: 1150–25000 å. *Publications of the Astronomical Society of the Pacific*, 110(749):863–878.

Pietrinferni, A., Cassisi, S., Salaris, M., Percival, S., and Ferguson, J. W. (2009). A large stellar evolution database for population synthesis studies. v. stellar models and isochrones with CNONa abundance anticorrelations. *ApJ*, 697:275–282.

Press, W. H., Teukolsky, S. A., Vetterling, W. T., and Flannery, B. P. (1992). *Numerical recipes in FORTRAN. The art of scientific computing.*

Prugniel, P., Soubiran, C., Koleva, M., and Le Borgne, D. (2007). New release of the ELODIE library: Version 3.1. *ArXiv Astrophysics e-prints*, page 3658.

Rayner, J. T., Cushing, M. C., and Vacca, W. D. (2009). THE INFRARED TELESCOPE FACILITY (IRTF) SPECTRAL LIBRARY: COOL STARS. *ApJS*, 185(2):289–432.

Renzini, A. (1981). Energetics of stellar populations. *Ann. de Phys.*, 6:87–102.

Riffel, R., Pastoriza, M. G., Rodríguez-Ardila, A., and Maraston, C. (2007). The first detection of near-infrared CN bands in active galactic nuclei: Signature of star formation. *ApJ*, 659(2):L103.

Salpeter, E. E. (1955). The luminosity function and stellar evolution. *ApJ*, 121:161.

Sánchez-Blázquez, P., Peletier, R. F., Jiménez-Vicente, J., Cardiel, N., Cenarro, A. J., Falcón-Barroso, J., Gorgas, J., Selam, S., and Vazdekis, A. (2006). Medium-resolution isaac newton telescope library of empirical spectra. *MNRAS*, 371:703–718.

Schiavon, R. P. (2007). Population synthesis in the blue. IV. accurate model predictions for lick indices and UBV colors in single stellar populations. *ApJS*, 171:146–205.

Searle, L., Sargent, W. L. W., and Bagnuolo, W. G. (1973). The history of star formation and the colors of late-type galaxies. *ApJ*, 179:427–438.

Skrutskie, M. F., Cutri, R. M., Stiening, R., Weinberg, M. D., Schneider, S., Carpenter, J. M., Beichman, C., Capps, R., Chester, T., Elias, J., Huchra, J., Liebert, J., Lonsdale, C., Monet, D. G., Price, S., Seitzer, P., Jarrett, T., Kirkpatrick, J. D., Gizis, J. E., Howard, E., Evans, T., Fowler, J., Fullmer, L., Hurt, R., Light, R., Kopan, E. L., Marsh, K. A., McCallon, H. L., Tam, R., Van Dyk, S., and Wheelock, S. (2006). The two micron all sky survey (2mass). *The Astronomical Journal*, 131:1163–1183.

Thomas, D., Maraston, C., Bender, R., and Mendes de Oliveira, C. (2005). The Epochs of Early-Type Galaxy Formation as a Function of Environment. *ApJ*, 621:673–694.

Tinsley, B. M. (1968). Evolution of the stars and gas in galaxies. *ApJ*, 151:547.

Tomczak, A. R., Quadri, R. F., Tran, K.-V. H., Labbé, I., Straatman, C. M. S., Papovich, C., Glazebrook, K., Allen, R., Brammer, G. B., Kacprzak, G. G., Kawinwanichakij, L., Kelson, D. D., McCarthy, P. J., Mehrtens, N., Monson, A. J., Persson, S. E., Spitler, L. R., Tilvi, V., and van Dokkum, P. (2014). Galaxy stellar mass functions from ZFOURGE/CANDELS: An excess of low-mass galaxies since z = 2 and the rapid buildup of quiescent galaxies. *ApJ*, 783:85.

Tonini, C., Maraston, C., Devriendt, J., Thomas, D., and Silk, J. (2009). The impact of thermally pulsing asymptotic giant branch stars on hierarchical galaxy formation models. *MNRAS*, 396(1):L36–L40.

Tonini, C., Maraston, C., Thomas, D., Devriendt, J., and Silk, J. (2010). Hierarchical models of high-redshift galaxies with thermally pulsing asymptotic giant branch stars: comparison with observations. *MNRAS*, 403(4):1749–1758.

Trager, S. C., Faber, S. M., Worthey, G., and González, J. J. (2000). The stellar population histories of local early-type galaxies. i. population parameters. *The Astronomical Journal*, 119:1645–1676.

Vacca, W. D., Cushing, M. C., and Rayner, J. T. (2003). A method of correcting near-infrared spectra for telluric absorption1. *Publications of the Astronomical Society of the Pacific*, 115(805):389–409.

Vassiliadis, E. and Wood, P. R. (1993). Evolution of low- and intermediate-mass stars to the end of the asymptotic giant branch with mass loss. *ApJ*, 413:641–657.

Vassiliadis, E. and Wood, P. R. (1994). Post-asymptotic giant branch evolution of low- to intermediate-mass stars. *ApJS*, 92:125–144.

Vazdekis, A. (1999). Evolutionary stellar population synthesis at 2 å spectral resolution. *ApJ*, 513:224–241.

Vazdekis, A., Casuso, E., Peletier, R. F., and Beckman, J. E. (1996). A new chemo-evolutionary population synthesis model for early-type galaxies. i. theoretical basis. *ApJS*, 106:307.

Vazdekis, A., Ricciardelli, E., Cenarro, A. J., Rivero-González, J. G., Díaz-García, L. A., and Falcón-Barroso, J. (2012). MIUSCAT: extended MILES spectral coverage. i. stellar populations synthesis models. *arXiv:1205.5496 [astro-ph]*. arXiv: 1205.5496.

Vazdekis, A., Sánchez-Blázquez, P., Falcón-Barroso, J., Cenarro, A. J., Beasley, M. A., Cardiel, N., Gorgas, J., and Peletier, R. F. (2010). Evolutionary stellar population synthesis with MILES. part i: The base models and a new line index system. *MNRAS*. arXiv: 1004.4439.

Westera, P., Lejeune, T., Buser, R., Cuisinier, F., and Bruzual, G. (2002). A standard stellar library for evolutionary synthesis. III. metallicity calibration. *A&A*, 381:524–538.

White, S. D. M. and Frenk, C. S. (1991). Galaxy formation through hierarchical clustering. *ApJ*, 379:52–79.

Wiklind, T. and Rydbeck, G. (1986). Detection of CO (j = 1-0) in the dwarf elliptical galaxy NGC 185. *A&A*, 164:L22–L24.

Worthey, G. (1994). Comprehensive stellar population models and the disentanglement of age and metallicity effects. *ApJS*, 95:107–149.

Worthey, G., Faber, S. M., and Gonzalez, J. J. (1992). MG and fe absorption features in elliptical galaxies. *ApJ*, 398:69–73.

Yan, H., Dickinson, M., Eisenhardt, P. R. M., Ferguson, H. C., Grogin, N. A., Paolillo, M., Chary, R.-R., Casertano, S., Stern, D., Reach, W. T., Moustakas, L. A., and Fall, S. M. (2004). High-redshift extremely red objects in the hubble space telescope ultra deep field revealed by the GOODS infrared array camera observations. *ApJ*, 616:63–70.

Young, J. S. and Scoville, N. Z. (1991). Molecular gas in galaxies. *ARA&A*, 29:581–625.

Young, L. M., Bureau, M., Davis, T. A., Combes, F., McDermid, R. M., Alatalo, K., Blitz, L., Bois, M., Bournaud, F., Cappellari, M., Davies, R. L., de Zeeuw, P. T., Emsellem, E., Khochfar, S., Krajnovic, D., Kuntschner, H., Lablanche, P.-Y., Morganti, R., Naab, T., Oosterloo, T., Sarzi, M., Scott, N., Serra, P., and Weijmans, A.-M. (2011). The ATLAS3d project - IV. the molecular gas content of early-type galaxies. *MNRAS*, 414:940–967.

Young, L. M., Scott, N., Serra, P., Alatalo, K., Bayet, E., Blitz, L., Bois, M., Bournaud, F., Bureau, M., Crocker, A. F., Cappellari, M., Davies, R. L., Davis, T. A., de Zeeuw, P. T., Duc, P.-A., Emsellem, E., Khochfar, S., Krajnovic, D., Kuntschner, H., McDermid, R. M., Morganti, R., Naab, T., Oosterloo, T., Sarzi, M., and Weijmans, A.-M. (2013). The atlas3d project – XXVII. cold gas and the colours and ages of early-type galaxies. *ArXiv e-prints*, 1312:6318.

Zhang, F., Li, L., Han, Z., Zhuang, Y., and Kang, X. (2013). Yunnan-III models for evolutionary population synthesis. *MNRAS*, 428(4):3390–3408.

Zibetti, S., Gallazzi, A., Charlot, S., Pierini, D., and Pasquali, A. (2013). Near-infrared spectroscopy of post-starburst galaxies: a limited impact of TP-AGB stars on galaxy spectral energy distributions. *MNRAS*, 428(2):1479–1497.